Theoretical and Experimental Study of Fuel Injector Tip Wetting as a Source of Particulate Emissions in Gasoline Direct-Injection Engines

by

Fahad M. Alzahrani

A dissertation submitted in partial fulfillment
of the requirements for the degree of
Doctor of Philosophy
(Mechanical Engineering)
in the University of Michigan
2020

Doctoral Committee:

Professor Volker Sick, Chair
Professor Andre Boehman
Dr. Mohammad Fatouraie, Robert Bosch LLC
Professor Venkatramanan Raman

Fahad M. Alzahrani

fahadmz@umich.edu

ORCID iD: 0000-0001-5101-7118

Dedication

“To my beloved mother who provides me with limitless love and prayers”

Acknowledgements

First and foremost, I would like to thank my parents, wife, and siblings for their unconditional love and support. Uniquely, the tremendous moral support from my mother kept me going, fueled me and pushed me beyond my limits. My accomplishments could not have happened without her encouragement and prayers she sent, and still sending to me and I am very grateful for her.

I would like to specially thank my academic advisor, Professor Volker Sick, for his incredible support, guidance and mentorship. I am deeply grateful and appreciative for the faith and trust he placed in me to perform my research work at the R&D facility of Robert Bosch LLC. Before joining his research group, I mentioned to him that I had an interest to conduct applied research that has a direct impact on the industry. After joining his group, he presented me with the opportunity to work in the industry for my Ph.D. I am very thankful for him and for keeping my interest in his mind.

I also would like to thank my supervisors and mentors during my time at Bosch. First, I would like to thank my supervisor and committee member, Dr. Mohammad Fatouraie, for his remarkable guidance and mentorship. I learned a lot from him especially on how to critically analyze research directions. His managerial support to conduct my experiments was also invaluable to complete my dissertation work. I am also thankful for the deep and motivating discussions we had, as it pushed my limits and polished my research work. Without it, this work could not have been possible. Secondly, I would like to thank Dr. Kevin Peterson and Dr. Michael

Mosburger for their mentorship and guidance during my first year at Bosch. They were great mentors and I learned a lot from them, and I am grateful for their assistance and guidance.

I also would like to thank my other committee members, Professor Andre Boehman and Professor Venkatramanan Raman, for their time and effort to serve on my committee. Their invaluable feedback and recommendations made this dissertation work complete.

I also would like to thank all technicians and engineers at Bosch who provided me with technical support to successfully complete my experimental work. Special thanks to Test Engineer Robert Arden and Senior Technician Michael Vlasblom for their assistance. The experimental work could not have been completed without their unique support. I also would like to thank members of the Quality Lab at Bosch for allowing me to use the 3D digital microscope for my tip imaging experiments. I am very appreciative of their flexibility to share their time with me to conduct my experiments. At times, they had to postpone their work to allow me to finish the experiments I needed to finish and I am very thankful for that.

I am also very thankful to all other friends and colleagues in Bosch and the University of Michigan for their helpful technical and non-technical discussions. Specially, I would like to thank my good friends Mohammad Alzuabi, Mario Medina, Dr. Ripudaman Singh, Nandan Vora and Shraavan Ravindranath for their helpful discussions and input on my work. Their deep insights and critiques were very helpful at many times. Special thanks to Steve Wozniak for his great company during my time at the Quality Lab and for his generosity to share his snacks with me every single time. I am thankful for his friendship.

I also would like to thank my research sponsors, BOSCH Group and the Department of Mechanical Engineering in the University of Michigan, for providing financial and technical resources for this work.

I also would like to express my sincere gratitude to my scholarship sponsor, King Fahd University of Petroleum & Minerals, for providing me and my family the necessary financial resources to complete my Ph.D. studies at the University of Michigan.

Table of Contents

List of Tables

List of Figures

List of Appendices

List of Acronyms

aTDC	after top dead center
bTDC	before top dead center
BMEP	brake mean effective pressure
CAD	crank angle degree
EOI	end of injection
GDI	gasoline direct injection
HC	hydrocarbon
ICE	internal combustion engine
PAH	polycyclic aromatic hydrocarbon
PM	particulate mass
PN	particulate number
RPM	revolutions per minute
SOI	start of injection

List of Symbols

A_s	Surface area	[m^2]
A, B, C	Antoine parameters	[-]
c_p	Specific heat capacity	[J/kg-K]
D	Diffusion coefficient	[m^2/s]
k	Thermal conductivity	[W/m-K]
L	Axial distance from tip surface for film geometry	[m]
L_s	Film thickness	[m]
m	Mass	[kg]
m_i, m^*	Initial film mass	[kg]
$\bar{M}$	Molecular weight	[kg/mol]
p	Pressure	[Pa]
$p_{v,L}$	Liquid vapor pressure	[Pa]
$p_{v,G}$	Vapor pressure in gas	[Pa]
p_c	Critical pressure	[bar]
r	Radial distance from center of spherical drop	[m]
R	Universal gas constant	[J/mol-K]
t	Time	[s]
T	Temperature	[K]
T_c	Critical temperature	[K]

T_w	Tip temperature	[K]
T_L	Liquid film temperature	[K]
$T_{L,0}$	Initial film temperature	[K]
V	Volume of liquid film	[m^3]
V_v	Volume of vapor	[m^3]
v_c	Critical molar volume	[m^3]
z_c	Compressibility factor	[-]
ρ	Density	[kg/m^3]
$\rho_{v,L}$	Liquid vapor density	[kg/m^3]
$\rho_{v,G}$	Vapor density in gas	[kg/m^3]
σ	Characteristic Lennard-Jones length	[Å]
ε	Characteristic Lennard-Jones energy	[J]
Ω_D	Diffusion collision integral	[-]
τ_c	Evaporation time constant	[s]

Abstract

Gasoline fuel film deposited on the tip of a fuel injector, i.e. injector tip wetting, has been identified as a significant source of particulate emissions at some operating conditions of gasoline direct-injection (GDI) engines. Fuel films on the injector tip at the time of spark burn in a diffusion flame, producing particulates. The physical mechanisms of the fuel film formation remains largely unclear as they depend on many parameters including engine hardware and operating conditions. Understanding the effect of these physical parameters on the film formation process can lead to better mitigation of the liquid film, which can result in significant reductions in particulate emissions. The liquid film on the injector tip can be reduced by either mitigating the initial fuel film that deposits on the tip during injection or by evaporating all or most of the fuel film before ignition takes place. The former process requires a clear understanding of the dependence of the fuel film formation on injector design, operating conditions and fuel flow conditions through the injector nozzle, which impose difficulties in the understanding due to the complex and interrelated processes involved. The liquid film evaporation process, i.e. injector tip drying, however depends mainly on engine operating conditions, and less on hardware or fuel flow dynamics. Understanding of the physics of injector tip drying is therefore less ambiguous but remains a challenge. Clear understanding of the tip drying physics can lead to significant reductions in PN emissions due to tip wetting.

This work developed an analytical model for liquid film evaporation on injector tip during an engine cycle for the mitigation of injector tip wetting. The model explains theoretically how fuel films on injector tip evaporate with time from end of injection to spark. The model takes into

consideration engine operating conditions, such as engine speed, engine load, tip and fuel temperatures, gas temperature and pressure, and fuel properties. The model was able to explain for the first time the observed trends in particulate number (PN) emissions due to injector tip wetting at different operating conditions. Engine experiments were used to validate the theoretical model by correlating the film mass predicted at the time of spark to PN and tip deposit volume measurements at different conditions. A new experimental technique was developed to measure the volume of tip deposit for this purpose since tip deposits are good indicators of tip wetting. In addition, an evaporation time constant was defined and was also found to correlate well with measured PN for all conditions tested. Injector manufacturers can use this time constant to maximize liquid film evaporation by correlating the variables in the time constant equation to changes in hardware and calibration.

The results indicate that the liquid film evaporation on the injector tip follows a first order, asymptotic behavior. Additionally, the initial film mass after end of injection was confirmed to increase linearly with injected fuel mass, i.e. engine load. Furthermore, the observed increasing exponential trend in PN emissions with engine load was due to the exponential nature of injector tip drying. As the initial film mass after injection increased linearly with engine load, the film mass at the time of spark increased in an exponential manner. A parametric study was also performed to understand the influence of the different initial and boundary conditions on fuel film evaporation. The liquid film evaporation on the injector tip was found to be highly sensitive to most of the injector initial and boundary conditions including the initial film mass after end of injection, the wetted surface area, the available time for tip drying and the injector tip temperature. The initial film temperature had the least effect on film mass evaporation.

Chapter 1 Introduction

To reduce further the contribution of internal combustion engines (ICEs) to environmental pollution, the emission limits for ICEs are continuously reduced. This requires the automotive industry to use advanced combustion strategies, modify existing hardware and/or exert larger efforts in engine calibration in order to meet these limits. In the context of direct-injection ICEs, such as diesel engines and gasoline direct-injection (GDI) engines, one of the main pollutants of interest is the particulate matter, primarily consisting of soot particles. There has been extensive work investigating soot formation in diesel engines [1–5]. Therefore, there is a well-established conceptual model for soot formation in this kind of engine [2]. With strongly reduced particles on diesel side using the diesel particulate filter (DPF), the discussion about further reducing particles for GDI and turbocharged GDI engines has also recently gained speed [6].

Particulate emissions regulations for GDI engines, which include particulate mass (PM) limits, are trending towards particulate number (PN) criteria. For example, in 2014 PN standards were introduced in Europe for GDI engines with a limit of 6×10^{12} particles/km, which was reduced by an order of magnitude in 2017 to the current limit of 6×10^{11} particles/km [7], and the same limit must be met in China by 2020 [8]. While the total PM limits for GDI engines has been investigated fairly well in the past decade and most likely the future limits can be met [9,10], the limits for PN were recently introduced and are more challenging to meet. Identifying and mitigating the sources of PN emissions for GDI engines is therefore critical to meet future emissions targets.

In GDI engines, the formation mechanisms of majority of engine-out PN are related, directly or indirectly, to the fuel injection process. Direct fuel injection into the combustion chamber may lead to the wetting of combustion chamber walls including piston crown, cylinder liner, intake and exhaust valves, spark plug, cylinder head and/or fuel injector tip. The fuel films formed on these surfaces, if not managed and/or mitigated, can lead to diffusion flames that result in significant amounts of PN emissions. Nowadays, most of surface wetting can be avoided using different design criteria and operating strategies. On the other hand, wetting of the fuel injector tip has been difficult to avoid completely despite the substantial reduction that has been achieved in the past.

PN due to tip wetting is a function of how much fuel wets the tip at the end of the injection process and how much fuel evaporates from the tip before the time of spark, i.e. tip drying. Furthermore, when the fuel film that is formed on the external surface of the injector tip does not fully vaporize before ignition, high temperature pyrolysis during combustion and exhaust strokes leads to carbon deposit formation on the injector tip. These deposits alter further tip wetting, amplifying its effect and increasing engine-out soot, a phenomenon known as PN drift. Since the measurement of the fuel film mass and/or thickness on the injector tip involves a lot of experimental uncertainty [11], most of the studies conducted on the tip wetting problem often relate the fuel film and the resulting diffusion flame to the deposit forming on the injector tip. It should be noted that for these studies the operating conditions were selected carefully to isolate the injector wetting as the main source for soot formation. However, most relations observed between PN emissions and injector deposit are qualitative, and no quantitative correlations were observed. In addition, current models used to predict tip wetting are computationally expensive CFD simulations that involve the solution of mass, momentum and energy equations along with complex spray and evaporation models.

1.1 Dissertation Objectives

The general objective of this dissertation is to understand the links between injector tip wetting, the resulting PN emissions, and the corresponding deposit growth on the tip. Specifically,

- It is desired to understand how the fuel film on the injector tip evaporates and affects the engine-out PN emissions. Understanding of the physics of fuel film evaporation from the injector tip is essential to enable reduction or elimination of PN formation and emission due to injector tip wetting. A hypothesis that explains the physics is proposed and formulated using a theoretical model, which is validated with experiments.
- Once the physics of fuel film evaporation is understood based on the theoretical model, the effect of injector initial and boundary conditions on liquid film evaporation on fuel injector tip is investigated and the most influential parameters in mitigating injector tip wetting are highlighted.
- It is desired to quantify and measure the amounts of injector deposit formed as a result of injector tip wetting and then explore the quantitative relationship between PN emissions and injector deposit at different operating conditions. A new method is proposed and used to quantify the amount of injector deposit based on three-dimensional digital microscopy.

The remainder of this dissertation is organized as follows. In Chapter 2, a literature review on soot particles and surface deposit formation chemistries is given first, followed by reviewing the current knowledge of the mechanisms of tip wetting, tip drying and injector deposit formation in GDI engines. The chapter concludes with the proposed hypothesis for liquid film evaporation on the fuel injector tip. Chapter 3 presents the development of the theoretical model and the solution algorithm used in the calculations. The experimental methodologies used to quantify PN emissions and deposit formation on the injector tip are illustrated in Chapter 4. The test matrix and test procedure used to validate the theoretical model is presented at the end of Chapter 4. Chapter

5 shows the results of model validation, the parametric study as well as the quantitative nature of increased PN emissions due to injector deposit formation. The conclusions and recommendations for future work are given in Chapter 6.

Chapter 2 Background and Hypothesis

In this chapter, a brief background on soot particles and surface deposit formation chemistries is given first, followed by generally reviewing the known sources of soot in GDI engines. More focus is given to injector tip wetting as a source of soot particles formation and emission, with analysis of the research gaps in the understanding of soot formation mechanisms in relation to injector tip wetting, tip drying and the corresponding deposit growth on the injector tip. The chapter concludes with the proposed hypothesis for fuel film evaporation on the injector tip during an engine cycle.

2.1 Chemistry of Soot Particles Formation

Soot is a solid material that contains very high content of carbon with typical H/C ratio of about 0.1 compared to 1.84 for gasoline [12]. In general, soot is formed as a result of incomplete fuel-rich combustion of hydrocarbons (HCs). The incomplete fuel-rich combustion zones can form during for example fuel-air mixing, crevice volumes, and liquid fuel films. Lighty et al. [13] summarized the soot formation process in time during an incomplete combustion process in the diagram shown in Figure 2.1, which the authors adapted based on the work of Bockhorn [14]. The most accepted starting chemical pathway for soot formation begins with ethylene (C_2H_4), which is an intermediate usually formed in large amounts during the combustion process of hydrocarbon fuels [15,16].

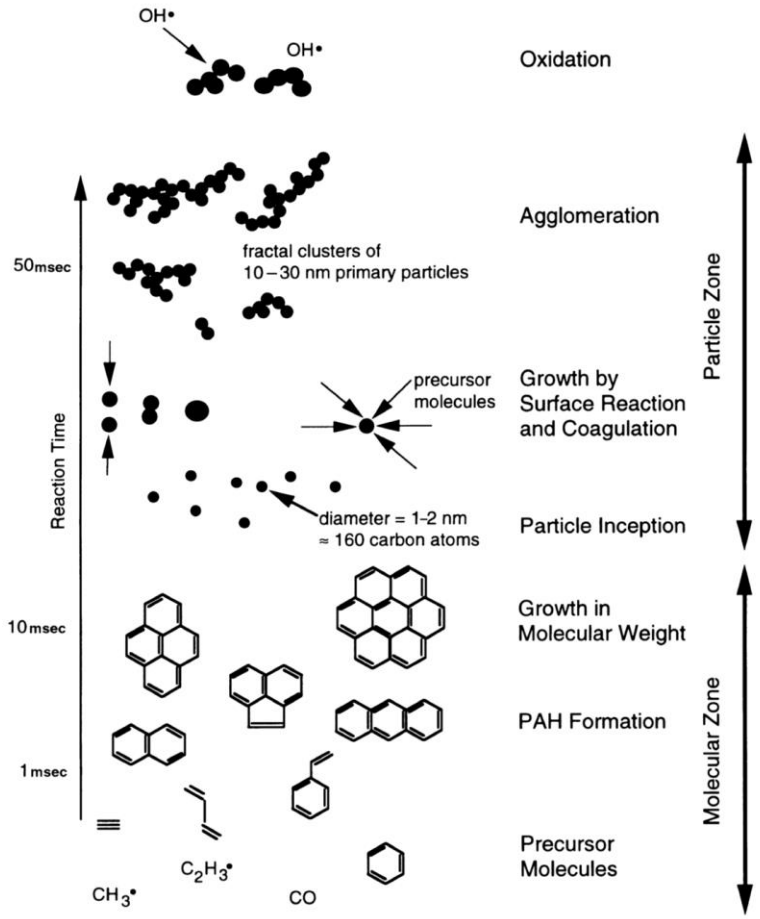

Figure 2.1: Timescale of soot formation chemistry [13]

During combustion, if oxygen (O), hydroxide (OH) or hydrogen (H) are available, ethylene will oxidize to form carbon monoxide (CO). However, if oxygen is unavailable and the temperature is high, decomposition of ethylene will most likely proceed by dehydrogenation.

$$H_2C = CH_2 \longrightarrow H_2C = \dot{C}H + \dot{H}$$

A second dehydrogenation proceeds to form acetylene (C_2H_2), which is a precursor in soot formation.

$$H_2C = \dot{C}H \longrightarrow HC \equiv CH + \dot{H}$$

Ethynyl radical formation proceeds after that by another dehydrogenation.

$$HC \equiv CH \longrightarrow \dot{C} + \dot{H}$$

With acetylene and ethynyl radicals as precursor molecules, polycyclic aromatic hydrocarbons (PAHs) and other cyclic compounds can form, and the process of soot formation continues, as shown in Figure 2.1. In general, the process from PAH to soot formation is a multi-step process [17] that starts with nucleation or inception of nuclei particles (average diameter of 1.5 nm) from heavy PAHs. The small particles then grow into large or primary soot particles by surface growth through gas-phase species condensation such as acetylene and PAH molecules and/or by coalescence or coagulation, which is the formation of primary particles from two or more small particles.

Soot generated from combustion often consists of clusters, also called agglomerates, of the large or primary particles, attaching together and forming groups (Figure 2.2) [18]. The size of primary particles ranges from around 10 to 40 nm, and the size range for the agglomerates is from 100 to 1000 nm. Most of the soot particles from combustion engines are of size less than 100 nm, which poses concerns regarding the negative impact they could have on human health [19].

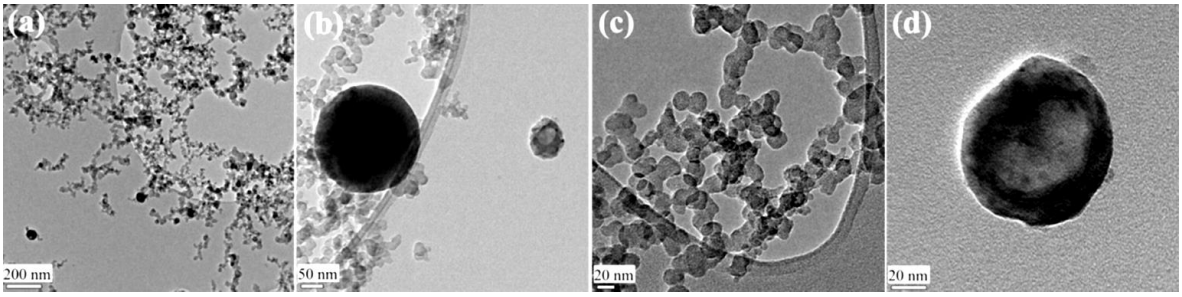

Figure 2.2: Vehicle exhaust particles collected and imaged using TEM [18]

2.2 Chemistry of Surface Deposit Formation

A liquid fuel film setting on a hot surface goes through certain chemical reactions that eventually convert it into a carbon deposit. Altin et al. [20] concluded that liquid oxidation reactions of alkyl radicals, which normally generate hydro-peroxides besides other oxidized products, are the ones responsible for the formation of deposits. Specifically, above 350 °C

formation of carbon deposits take place via two distinct chemical pathways: (1) elemental carbon and hydrogen formation by decomposition of HCs. This chemical route is often followed by metal catalysis of carbon deposition. (2) The second pathway is the large PAHs generation by polymerization and condensation of HCs species. The PAHs then nucleate and grow into carbon deposits. Usually, non-catalytic carbon deposition takes place through the polymerization route. Furthermore, the catalytic property of the surface at which deposits form on i.e. catalytic surface vs. non-catalytic surface, can influence the process of carbon deposition [20]. A catalytic surface can accelerate or decelerate the deposition process by the interaction with reactive species in the liquid. A non-catalytic surface on the other hand can act as a heat sink affecting the combustion system's heat and mass transfer, collecting more carbon deposits. One example for this is thermophoresis, where particles transfer from the hot fluid to the cold surface due to high temperature gradients. It is worth mentioning that the influence of a catalytic surface on the deposition process could reduce as particles build up on the surface since the layer of deposit act as an insulator, eliminating the contact between the surface and the liquid fuel. This infers that carbon deposition by non-catalytic reaction pathway is important for both catalytic and non-catalytic surfaces.

In the context of injector deposit formation, Xu et al. [21] indicated that precursors of injector deposits are formed through oxidation, condensation and precipitation of unstable HCs e.g. aromatics and olefins. These precursors form deposits through two different chemical reaction pathways: (1) auto-oxidation at low temperatures, and (2) coking or carbon deposition by high temperature pyrolysis. However, it is not clear what temperatures indicate the transition from one pathway to the other i.e. low to high temperature since both reaction pathways can take place at the same time at a specific range of temperature.

2.3 Sources of Soot in GDI Engines

Vehicles equipped with GDI engines can generate particulates by a number of mechanisms, which often take place simultaneously during engine and/or vehicle operation. There are mechanisms that are independent of the fuel injection process, like for example oil-related mechanisms such as oil leakage from the turbocharger or introduction of oil to the crankcase ventilation system i.e. PCV. Such mechanisms generally indicate bad engine design or engine malfunction [22] and they are not the focus here. On the other hand, the sources of particulates that are related to the engine fueling are attributed to the combustion of fuel-rich regions inside the combustion chamber. Typically, these regions are formed in either the gas phase because of the poor mixing process of fuel and air or due to fuel impingement on chamber walls during spray leading to liquid films forming on these surfaces [22–25].

2.3.1 Gas Phase

It is generally desired to form a perfect, homogenous mixture of fuel and air, which ideally should not generate particulates. However, the direct fuel injection process in GDI engines requires all of the injected fuel to vaporize and completely mix with the intake air in a very short period. Local zones with over-abundance of fuel can fail to complete that process in a timely manner before ignition, resulting in soot formation. Perfect mixing of fuel and air is generally driven by fuel injection characteristics, such as drop size, air entrainment during injection and spray penetration, as well as the mixing characteristics including the mixing time and turbulence [22]. An example of soot luminosity in the gas phase can be seen in Figure 2.3 [22]. The figure shows three endoscopic images (taken at ~90^{o} aTDC) of the combustion event inside a GDI engine, which is at room temperature. The different images represent various injection timings, where the timing is retarded (from left to right) so that there is less time for mixing and drops evaporation. As

observed in the figure, higher soot luminosity is observed as the time for mixing and evaporation is reduced.

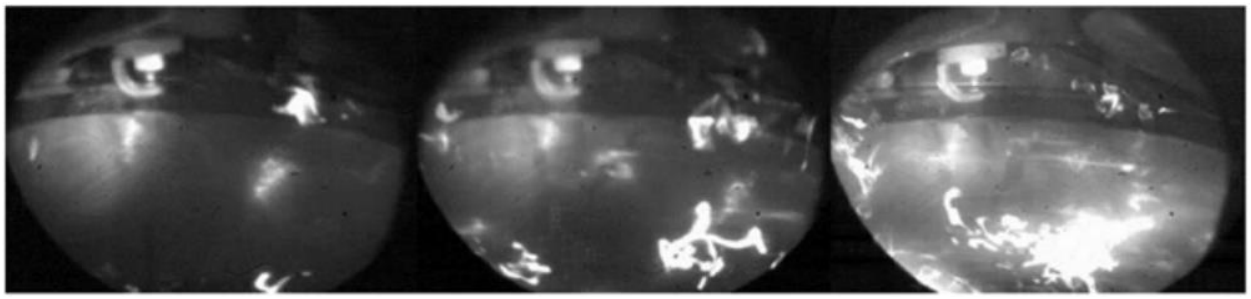

Figure 2.3: In situ high-speed imaging via endoscope showing soot luminosity in a GDI engine combustion chamber. Injection timing is retarded from left to right image. Piston timing is 90º aTDC [22]

2.3.2 Liquid Films

Because the fuel is directly injected into the combustion chamber of a GDI engine, the chamber's surfaces become susceptible to fuel wetting. Pool fires are created when liquid-phase fuel impinges on surfaces, including the piston crown, intake and exhaust valves, and cylinder walls [19,20]. If the operating temperature, pressure and gas flow conditions during intake and compression strokes are not sufficient to evaporate all of the fuel on these surfaces, diffusion flames occur leading to soot formation (Figure 2.4). If the fuel film is not fully vaporized and burned and there is fuel film remaining on the surface, high temperature pyrolysis leads to carbon deposits on the surface. These deposits can amplify the amount of surface wetting, leading to increased soot formation [28]. Fuel films impinging on combustion chamber surfaces in GDI engines are the major source for soot formation and emission, and in return managing the liquid film is crucial to controlling soot formation in GDI engines.

Figure 2.4: An endoscopic image showing a diffusion flame taking place as a result of fuel impingement on the piston's surface during the fuel injection process [29]

2.4 Injector Tip Wetting as a Source of Particulate Formation and Emission

Some operating strategies and design criteria can help reduce and sometimes eliminate fuel-rich zones due to liquid films in most surfaces, such as late fuel injection or multiple fuel injection events [30,31]. However, one surface wetting mechanism that cannot be avoided by calibration and is not well understood is injector tip wetting. Injector tip wetting occurs when liquid-phase fuel films or droplets remain on the exterior surface of the tip of the fuel injector due to the fuel injection event. In a certain engine-operating map, injector tip wetting can be the dominant soot formation mechanism. Figure 2.5 shows an endoscopic image of a typical diffusion flame resulting from fuel injector tip wetting in a GDI engine [29].

Figure 2.5: An endoscopic image showing a diffusion flame taking place on the injector tip due to the fuel injection process [29]

2.4.1 Physical Mechanisms of Injector Tip Wetting

During the fuel injection process, the fuel wets the injector tip surface as the fuel leaves the injector nozzle holes. Figure 2.6 shows schematics of the fuel flow leading to tip wetting in a GDI injector nozzle and the important features to describe the internal geometry of a GDI injector nozzle [32].

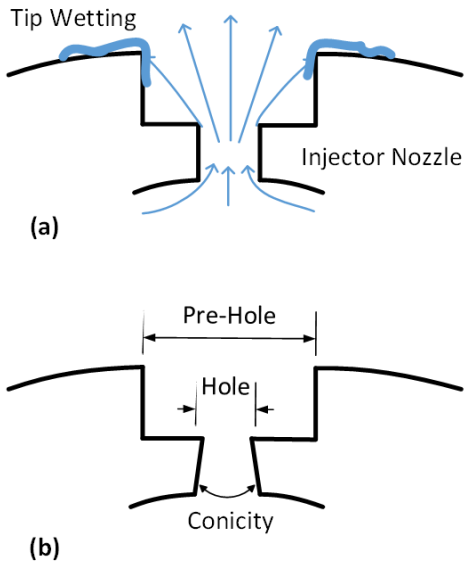

Figure 2.6: Schematics of the (a) general fuel flow leading to injector tip wetting in GDI engines, and (b) the basic internal features of GDI injector nozzle design [32]

The physical mechanisms that lead to injector tip wetting can be grouped into three categories [32]. The first is the fuel deposited on the injector nozzle tip *during the injection process*. The second is the fuel deposited on the nozzle tip *at the end of injection event via droplets, ligaments, and low momentum flow*. The third category is the fuel deposited on the nozzle tip from the *liquid and vapor inside the sac volume of the injector*. Two processes have been identified that contribute to injector tip wetting during injection. First, as the fuel flows through the nozzle hole and into the pre-hole (see Figure 2.6b), the fuel flow path widens. Depending on the geometry, flow dynamics, and operating conditions, the fuel flow interacts with the pre-hole wall and some of the fuel deposits on the surface of the wall and then flows around the corner and onto the outlet

of the orifice. The flow-through deposition process is shown schematically in Figure 2.7. Leick et al. [11] investigated tip wetting using laser-induced fluorescence and concluded that one of the most important conditions affecting injector tip wetting was flash boiling. Flash boiling is known to cause the spray plume to widen and under certain cases cause spray collapse [33,34]. Spray collapse has a direct impact on engine performance and emissions because it influences fuel-air mixing. Since flash boiling affects plume width, it subsequently affects injector tip wetting. This nozzle wetting mechanism was described as wide-plume wetting. As shown in Figure 2.7, wider plumes lead to more tip wetting compared with narrower plumes.

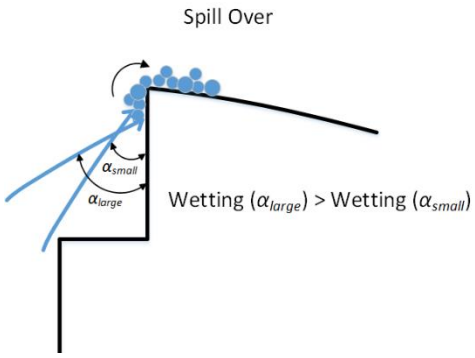

Figure 2.7: A conceptual model for injector tip wetting due to fuel spill over as a result of plumes hitting the edge of the pre-hole. Wider plumes leads to increased wetting [32]

The second process that leads to fuel films on the nozzle during fuel injection is caused by recirculation of the flow as it exits the orifice. During the injection process, a shear layer is formed between the ambient gases in the combustion chamber and the injected fuel. The shear layer is formed by a complex mixing process that is responsible for air-entrainment and mixing of the liquid and vapor phases of fuel with air. As part of the fluid mixing, vortices of fuel droplets and vapor are formed. The vortices re-entrain some of the fuel and air mixture back into the bulk flow, but some of the mixture escapes from the bulk flow. Fluid that escapes the vortices in the form of fuel droplets can be deposited on the injector tip due to the low-pressure zones formed near the nozzle exit. Droplets can deposit and stay on the injector tip due to the coandā effect, i.e. the

tendency for fluid to stay attached to a convex surface due to low pressure. A schematic of this vortex-droplet wetting process is shown in Figure 2.8.

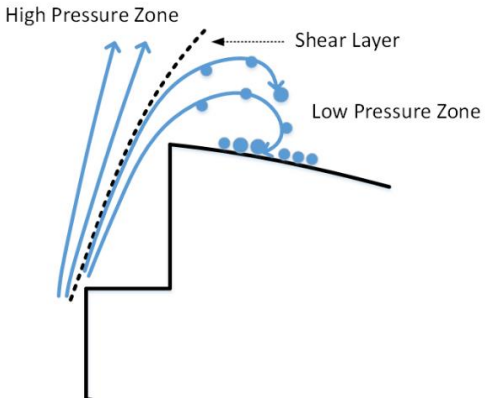

Figure 2.8: A conceptual model for injector tip wetting due to flow recirculation. Some droplets escape from the shear layer into the low-pressure zone and are deposited on the injector tip [32]

Injector tip wetting also occurs at the end of the injection event. During needle closing, the fuel flow rate decreases, which leads to lower flow velocities and lower momentum flow. The low flow rate results in 'fuel dribble' i.e. ligaments and large droplets formed at the end of injection [35–37]. Previous work on diesel injectors has focused mostly on identifying the end-of-injection needle effects on bubble ingestion inside the nozzle and total mass ejected from fuel dribble. Eagle and Musculus [38] provide a comprehensive categorization of dribble events for diesel fuel and heavy duty fuel injectors. They identified three dribble behaviors that occurred during one engine cycle as well as proposed five potential physical processes that contributed to diesel fuel dribble. It should be highlighted that these mechanisms describe old diesel injectors, which differ significantly from GDI injectors in terms of sack volume. This mechanism of tip wetting has also been recorded and reported by Peterson et al. [39] for gasoline in GDI engines. However, no studies to date have investigated connections between fuel dribble and injector tip wetting. Some large droplets and ligaments are likely to deposit onto the injector tip, because the liquid parcels do not have enough momentum to separate from the nozzle. A schematic of fuel-dribble tip wetting is shown in Figure 2.9.

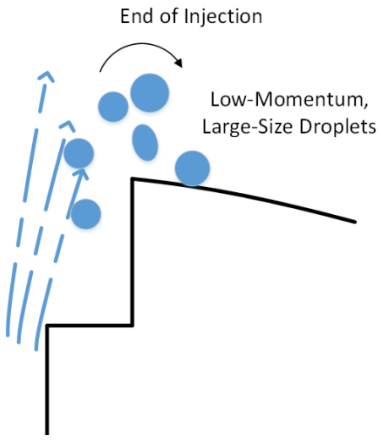

Figure 2.9: A conceptual model for injector tip wetting due to end of injection event as a result of low-momentum, large-size droplets [32]

The last mechanism to affect tip wetting is attributed to the liquid and gas mixture inside the nozzle or sac volume. During the expansion stroke of the engine cycle, the fuel mixture inside the sac volume is syphoned out of the injector. For diesel injectors, Eagle and Musculus [38] refer to this as late-cycle dribble, but made no connection to tip wetting. Tip wetting can occur during this process because the fuel mixture can condense onto the injector tip due to changing state conditions. The effects of this fuel-condensation tip wetting mechanism are also not well studied or understood.

2.4.2 Physical Mechanisms of Injector Tip Drying

The tip drying mechanisms are dictated by heat (or thermal) and mass transfer. Thermal evaporation of the liquid film on the injector tip is dependent upon several parameters including tip temperature, ambient pressure and temperature, total deposited fuel mass, and time. Fundamentally, the physics of liquid film thermal evaporation on an injector tip is analogous to sessile droplet evaporation on a hot plate. A droplet at steady-state conditions can go through two vaporization regimes: *single-phase evaporation* for tip temperatures below the liquid boiling point, and *boiling evaporation* for tip temperatures much higher than the boiling point. These mechanisms were observed by Karwa et al. [41] who investigated the effects of ambient pressure,

tip temperature and air flow velocity on tip drying rate in a controlled lab experiment using isooctane fuel. The single-phase evaporation thermal mechanism was observed to be significant for tip temperatures up to 10 °C higher than the boiling point, i.e. superheat of 10 °C. For tip temperatures higher than a superheat of 10 °C, the main thermal mechanism was controlled by boiling. Stanglmaier et al. [40] studied the evaporation behavior for Howell EEE certification gasoline at different system pressures, and the results indicated that at engine-like conditions, vaporization of multi-component fuels was best represented as single-phase evaporation.

Tip drying also occurs due to mass convection. Piston motion induces gas velocities that contributes to fuel film evaporation through mass convection, and importantly, the effects of airflow are only significant during single-phase evaporation, as reported by Karwa et al. [41]. Under this evaporation regime, the evaporation occurs dominantly at the liquid-gas interface and the flow of gas over the liquid surface assists in carrying out more molecules from the surface to the gas. Consequently, tip drying is attributed to single-phase evaporation and mass convection, which are shown schematically in Figure 2.10. Both tip drying mechanisms are a function of the bulk fluid temperature, T_g, and velocity, u_g, the fuel film or droplet temperature, T_L and the nozzle tip or wall temperature, T_w.

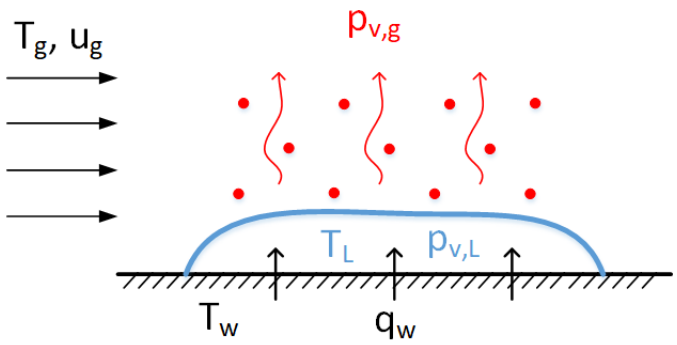

Figure 2.10: A conceptual understanding for injector tip drying based on single-phase evaporation and forced convection evaporation mechanisms

2.4.3 Physical Mechanisms of Deposit Formation on the Injector Tip

Incomplete evaporation of the liquid fuel film on injector tip leads eventually to deposit formation on the tip. There is a scarcity in literature on the available physical mechanisms that explain injector deposit formation in GDI engines. A physical mechanism that explains internal injector nozzle deposit formation was proposed by Kinoshita et al. [42]. The mechanism is schematically shown in Figure 2.11. It is proposed that deposit precursors, which formed through oxidation, condensation and precipitation of unstable HCs, are dispersed immediately in the liquid fuel after injection. Depending on the injector nozzle temperature and the 90% distillation temperature (T90) of the fuel, two different processes could proceed. (1) If the nozzle temperature is smaller than the T90 of the fuel, most of the fuel trapped in the nozzle will stay in the liquid state, and the precursors will be washed away by the next injection cycle. In this case, deposits do not form in the injector nozzle. (2) If the nozzle temperature is higher than the T90 of the fuel, most of the fuel in the nozzle would evaporate, and the deposit precursors adhere and stick to the nozzle wall. The precursors then nucleate and grow into agglomerates and form carbon deposits in the injector nozzle.

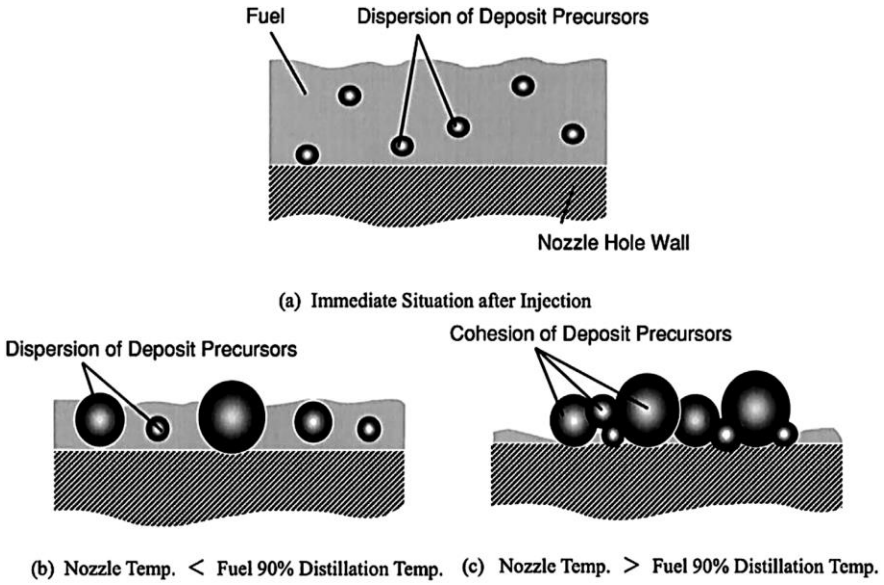

Figure 2.11: Mechanism of injector deposit formation proposed by Kinoshita et al. [42]

This mechanism shed light on the importance of the T90 parameter of the fuel in injector deposit formation. However, the role of the T90 of the fuel was disputed by Aradi et al. [43]. In their work, the fuel flow rate loss due to nozzle deposit plugging was measured for different nozzle temperatures and fuels with various T90s (Figure 2.12). It is generally observed that fuel rate loss increased with increasing nozzle temperature until a certain point after which it decreased. This shows that injector deposits is a strong function of nozzle temperature. For most of the situations where the nozzle temperature is higher than the T90 of the fuel, the fuel flow rate loss was lower than in the cases where the nozzle temperature is smaller than the T90. This indicates that there were less deposits for these cases, which contradicts the proposed mechanism by Kinoshita et al. It can be inferred from the work of Aradi and co-workers that injector deposits do not favor a very low or very high temperature range.

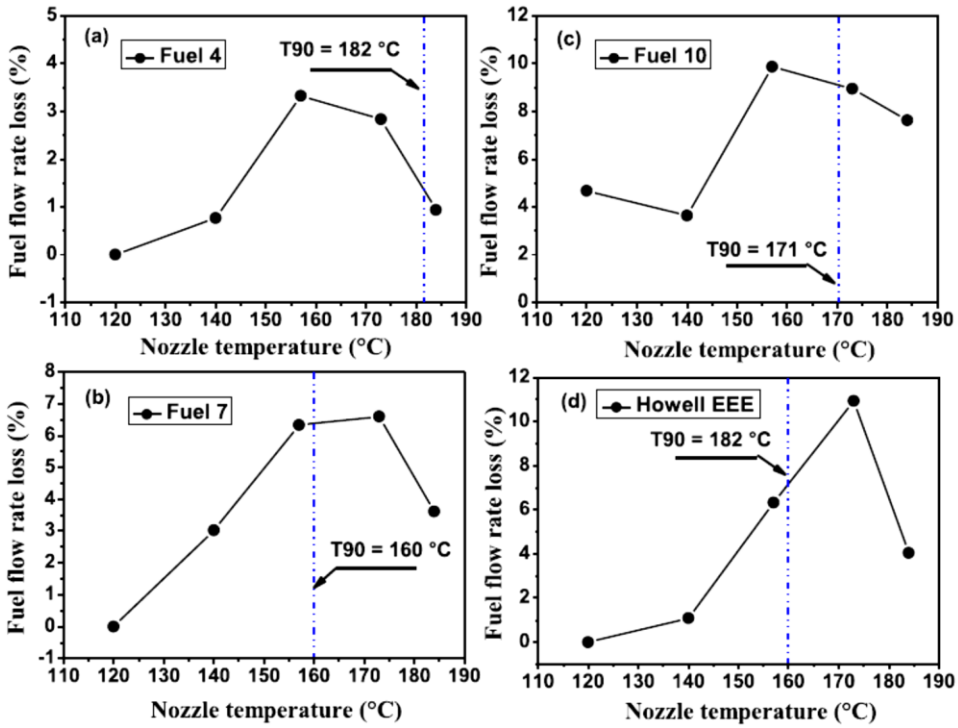

Figure 2.12: Percentage of fuel flow rate loss as a function of nozzle temperature for different fuels [21]

A more recent mechanism for external injector deposit formation was proposed by Slavchov et al. [44]. The mechanism is based on temporal variation of fuel film boiling

temperature, combustion gases temperature and injector tip temperature. As pressure changes during the engine cycle (Figure 2.13a), boiling point of the fuel film, in-cylinder gas temperature and injector tip temperature are assumed to vary according to Figure 2.13b. Accordingly, the authors assumed that the deposit formation mechanism proceeds according to the following process. (1) First, after the end of injection fuel droplets are hypothesized to leak out from the injector nozzle and sit on the external surface of the tip. During the cylinder peak pressure ($CAD_0 < CAD < CAD_b$), the droplet assumes the temperature of the tip, which is below its boiling temperature. (2) Once the combustion process takes place, radicals and deposit precursors formed in the gas transport into the liquid film. The liquid film then starts degrading by liquid oxidation reactions. (3) In the later stage of the cycle, where the boiling point of the droplet equals the tip temperature ($CAD > CAD_b$), the liquid film starts boiling until it evaporates completely. During boiling, the non-volatile degradation products are either adsorbed at the tip surface or precipitate in the liquid film. It is also assumed that for internal nozzle deposit formation, any materials that precipitated in the liquid film are washed away by the next injection event, and only materials that are strongly adsorbed and adhered to the nozzle wall remain.

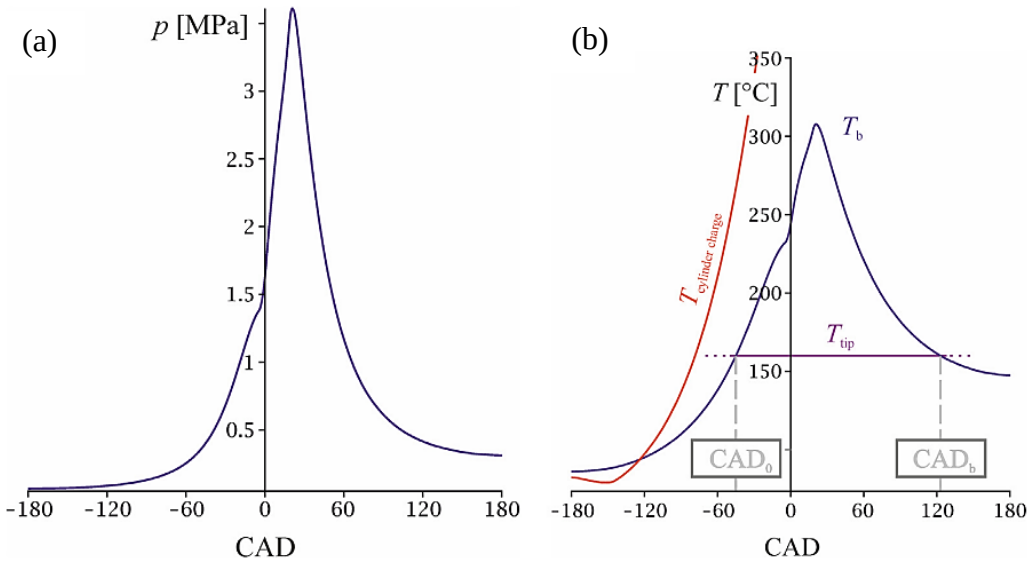

Figure 2.13: (a) variation of cylinder pressure p as function of crank angle degrees (CAD) during the engine cycle (SRM Engine Suite simulation). (b) variation of boiling temperature T_b calculated from the Clausius-Clapeyron equation, simulated temperature of the combustion gases $T_{cylinder\ charge}$, and average injector tip temperature T_{tip} during the engine cycle [44]

2.4.4 Correlations Between Injector Tip Wetting, the Resulting PN, and Deposit Growth on the Injector Tip

Injector tip wetting and tip drying have important effects on particulate emissions from GDI engines, and at specific conditions, combustion of fuel on the injector tip has been shown to be a significant source of particulates. For example, Berndorfer et al. [28] used in-cylinder imaging to identify and quantify luminescence from diffusion flames originating from the fuel injector tip of a large bore single-cylinder GDI engine. The large bore was used to reduce the effects of wall and piston wetting by the fuel spray. The imaging data of the injector diffusion flame were quantified and compared with experimental measurements of engine-out PM and PN. The diffusion flame results correlated well with the particulate measurements, leading the authors to conclude that combustion of the fuel on the injector tip was the dominant source of particulate emissions, whereas combustion of the bulk charge was not.

Similarly, Dageforde et al. [45] investigated the spray behavior including wall impingement, tip wetting, and PN emissions for injectors with different internal geometries using

different measurement techniques. The main differences in injector geometry were the pre-hole diameters and orifice inlets. When tested in a GDI engine, the authors observed a significant difference in PN emissions after a 20-hour endurance test for a reduced pre-hole diameter. The change in diameter decreased the penetration distance of the spray, reducing the likelihood of wall impingement of the fuel when visualized in a constant-volume chamber. Further testing using long distance microscopy revealed the reduced pre-hole diameter also resulted in qualitatively lower tip wetting. The authors concluded that the significant improvement in PN emissions was likely caused by the reduction in tip wetting from the pre-hole design modification.

Leick et al. [46] studied tip wetting using various methods both experimentally and computationally for gasoline sprays. Flash boiling and non-flash boiling operating conditions were compared to study the spray structure for a single injector. Simulations and constant volume chamber experiments helped understand differences in spray behavior between the different operating conditions. Compared to the non-flash boiling conditions, flash boiling sprays resulted in faster fuel vaporization and wider spray plumes at the orifice outlet. The wider spray plumes caused an interaction with the pre-hole surfaces resulting in tip wetting. However, the engine experiments revealed that flash boiling decreased PN emissions under certain operating conditions, and increased PN emissions for other operating conditions. The improvements in vaporization rates and worsening tip wetting could not be decoupled from the PN measurements in this engine study. However, in a related study on flash boiling, Leick et al. [11] performed laser-induced fluorescence to quantify the tip wetting area and height for different injector geometries and operating conditions. The results showed that flash boiling and injection pressure were the biggest factors affecting tip wetting. Changes in injector geometry did not reveal significant effects on tip wetting, contrary to what was found in Dageforde et al. for changes in geometry and PN emissions [45].

A study relevant to tip wetting and the resulting PN and deposit growth on the tip was performed by Peterson et al. [47], where they performed engine experiments of six multi-hole injectors having different geometries. The experiments were conducted in a single-cylinder GDI engine with optical access to the combustion chamber via both the head and the piston. Their study showed that all injectors had the same dominant soot formation mechanism, which is the liquid film on the injector tip surface resulting in diffusion flames that produce soot near TDC-firing. This soot fails to completely oxidize and carries on into the expansion stroke and eventually into the exhaust. Formation of the liquid film was owed to the occurrence of three phenomena (Figure 2.14). (1) A plume with extreme width, causing the external surface of the tip to be wetted. (2) End of spray fuel droplets, which are large and have low momentum, recirculating and landing on the external surface of the injector tip. (3) The incomplete clearance of the sac and internal nozzle volume from liquid fuel after the end of the spray.

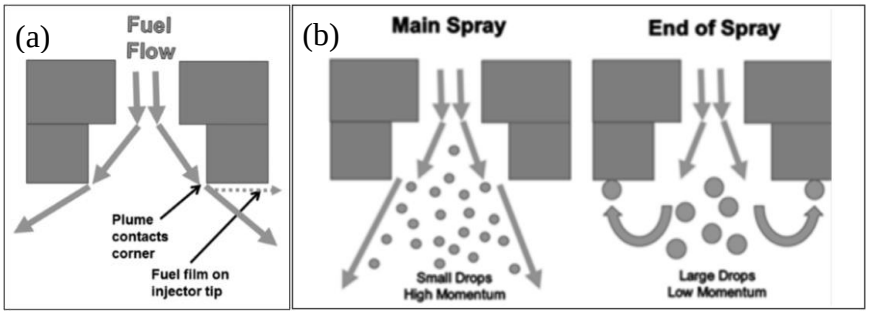

Figure 2.14: (a) Extreme width of plume causes the fuel to have contact with corners at the nozzle exit. This results in fuel film developing on the external surface of the injector tip. (b) During spray, high pressure difference results in high momentum flow and small drops. At the end of spray, low pressure difference results in low momentum flow and large drops that deposit on nozzle [47]

The three mechanisms are shown experimentally in Figure 2.15. All injectors were also observed to foul and injector fouling was related to injector tip wetting and PN emissions. Figure 2.16 shows a qualitative correlation between tip deposit and soot formation for three cases. In the first case, the injector tip was initially clean. For the second case, the initial condition of the injector is a fouled injector with a layer of deposit on the injector tip. The third case had half the injector

fouled and the other half cleaned. As shown in the figure, high soot production corresponds to the cases of fouled regions on the injector tip. In general, the authors observed that engine-out soot increased with increased injector fouling and decreased with increasing fuel rail pressure.

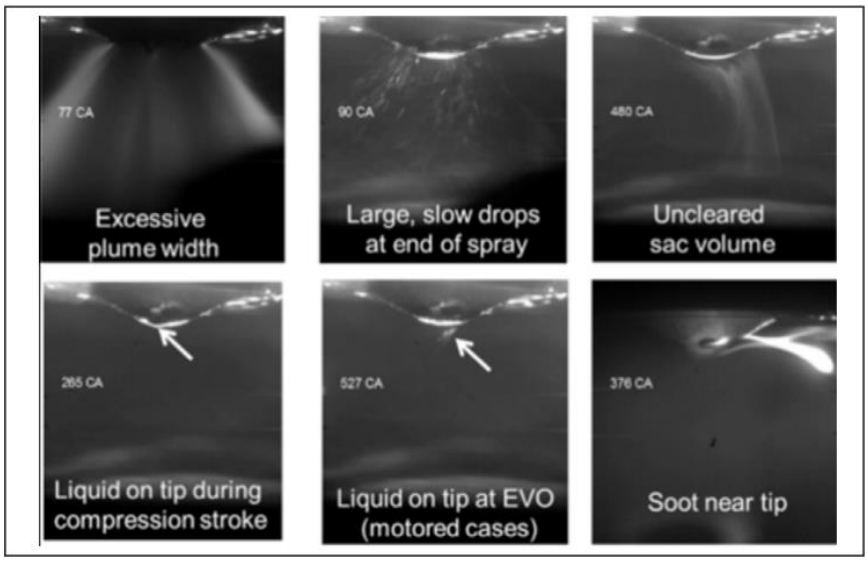

Figure 2.15: (Top row) Three mechanisms of injector tip wetting leading to diffusion flames on the tip. (Bottom row) Presence of liquid fuel on the tip and the resulting soot formation [47]

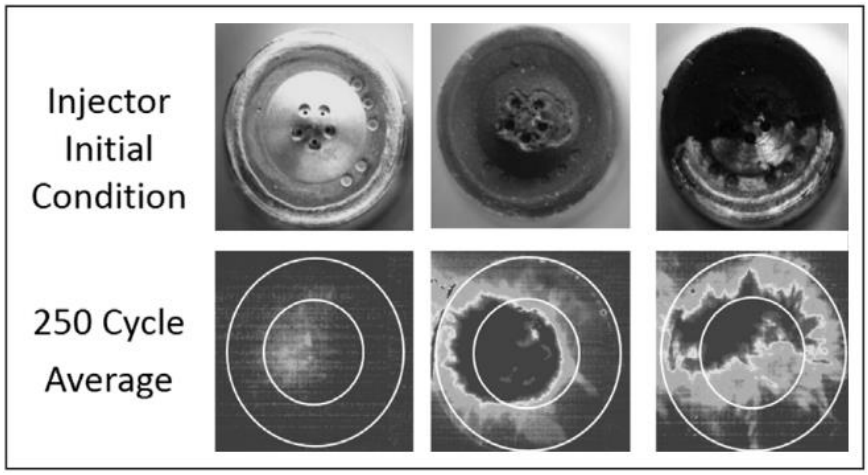

Figure 2.16: Effect of deposit growth on injector tip on soot formation [47]

Another work by Knorsch et al. [48] investigated the relationship between injector nozzle geometry and fuel films on the injector tip. The specific goal of the study was to understand the effect of cavitation forming inside the injector nozzle and the impact it has on PN emissions for an optimum design of nozzle geometry. The basic geometrical design of the injector nozzle studied

is similar to the design in Figure 2.6. The main design parameters studied were hole length, hole diameter, hole angle (conicity), pre-hole length and pre-hole diameter. A systematic variation of these parameters in a real engine was performed. The cavitation tendency for six nozzle geometries were evaluated in this study. In general, nozzles with higher hole length and stronger converging cone angle had lower cavitation tendency. This helped reduce the wetting of injector tip surface, resulting in lower PN emissions.

Berndorfer et al. [28] developed a measurement technique to derive a quantity called *injector diffusion flame* that quantifies the diffusion flame taking place on the injector tip. It was found that this quantity correlated well with the soot level (mass and number) measured in the exhaust, as can be seen in Figure 2.17. The figure also shows images of the clean injector before the beginning of the test and the coked (fouled) injector at the end of the test. Authors suggested that injector deposits act as a trap for fuel vapor that is later freed and combusted in a diffusion flame. Going to higher fuel rail pressures was also recommended for reducing injector diffusion flames.

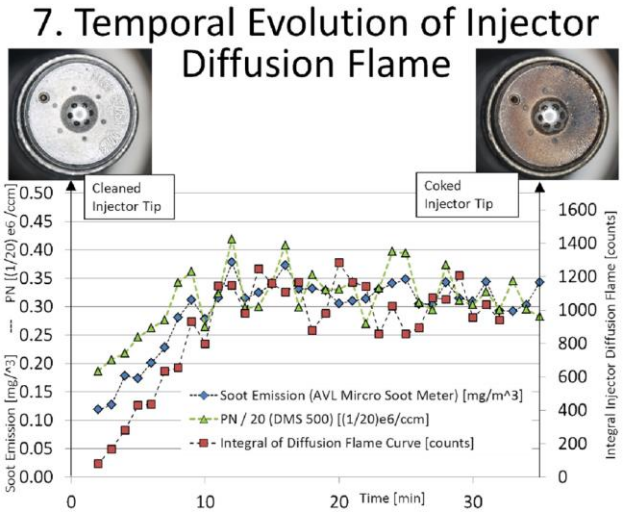

Figure 2.17: Injector diffusion flame has the same temporal evolution as soot emissions [28]

A recent study by Henkel et al. [49] looked at the effect of injector fouling on particulate mass and number emissions as well as spray characteristics. In this work, it was shown that injector

fouling has a negative impact on particulate emissions. The authors were able to reverse this negative effect by using fuel detergents. Four fuels (A, B, C and D) were used, two of which (B and C) contained a fuel detergent chemical. Engine tests were performed in two cycles: an injector fouling cycle and an injector clean-up cycle. The PN results can be seen for all of the fuels in Figure 2.18 for the injector fouling cycle and Figure 2.19 for the injector clean-up cycle. To check if there is a correlation between the level of particulate emissions and injector deposits, injectors were imaged after each cycle (Figure 2.20 and Figure 2.21). Clearly, the use of fuel detergency, which reduced PN levels resulted in cleaned-up regions inside the injector nozzles and on the external tip surface around the nozzles.

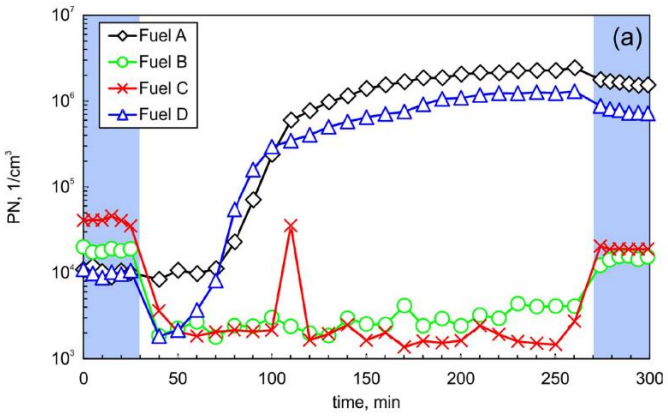

Figure 2.18: Time evolution of PN emitted by the engine for the four fuels studied for the injector fouling cycle. The blue region indicate 30-minute operation with reduced speed, load and fuel rail pressure [49]

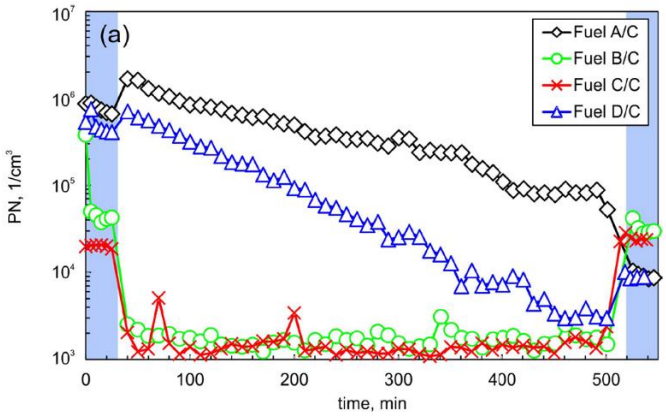

Figure 2.19: Time evolution of PN emitted by the engine for the four fuels studied for the injector clean-up cycle. The blue region indicate 30-minute operation with reduced speed, load and fuel rail pressure [49]

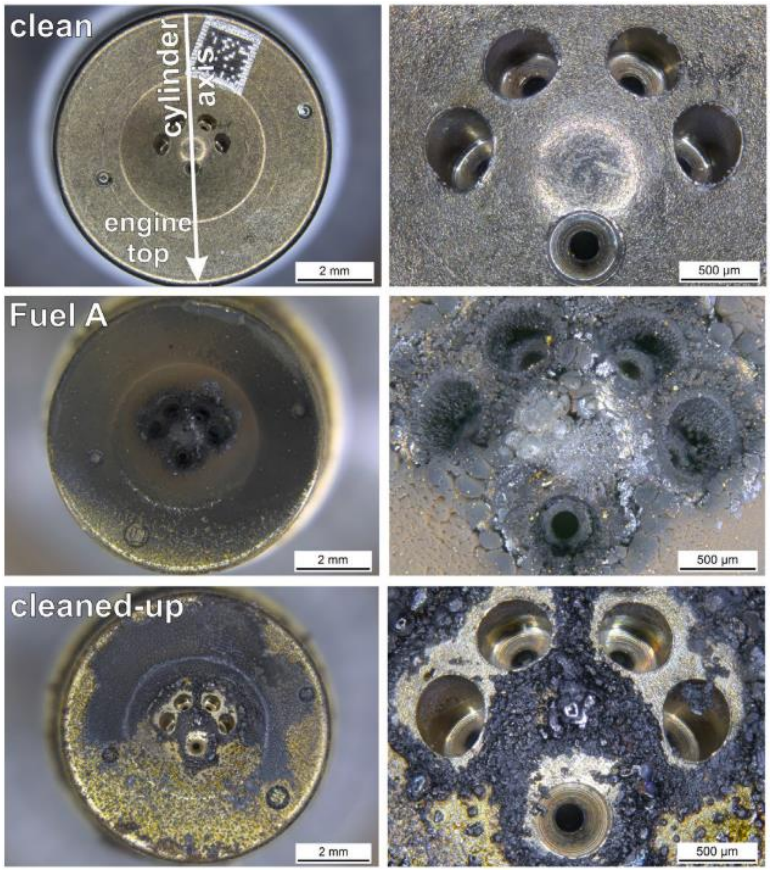

Figure 2.20: Clean (top), fouled (middle) and cleaned-up (bottom) injector images for engine running on Fuel A. Images in the right column are zoomed in versions of the images in the left column [49]

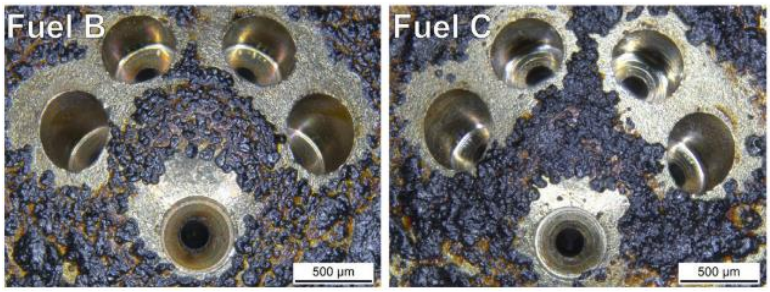

Figure 2.21: Images of injectors used in engine running on detergent Fuel B and C [49]

Effect of injection pressure and charge motion on particulate emissions was also studied by Piock et al. [50]. Figure 2.22 shows the effect of fuel rail pressure and charge motion on PN emissions. It is generally observed that increasing injection pressure results in lower tip wetting PN as evident by the luminosity shown in Figure 2.23, which shows endoscopic images of diffusion flames taking place at injector tip surface due to injector tip wetting for three different

injection pressures. Charge motion was also shown to result in lower PN emissions. The authors owed this to the enhancement in mixture formation, leading to better homogeneity, but made no connection to tip wetting. However, the lower PN could also be as a result of better fuel film evaporation, as observed by Karwa et al. [41].

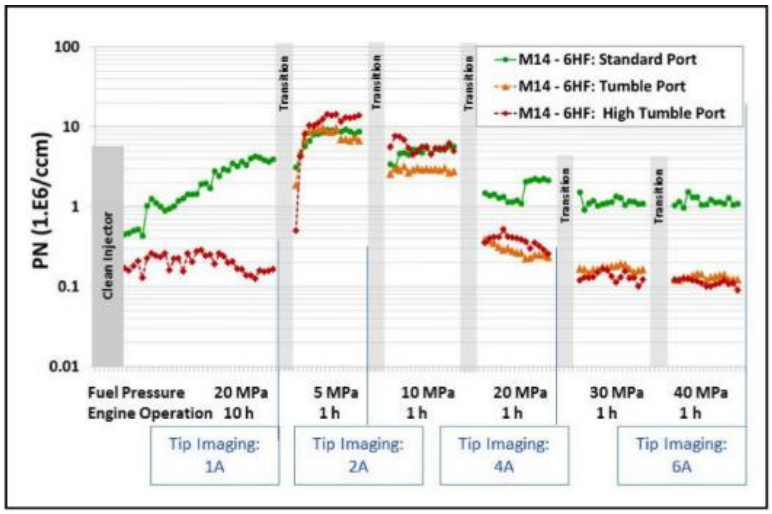

Figure 2.22: Effect of fuel rail pressure and charge motion on PN emissions [50]

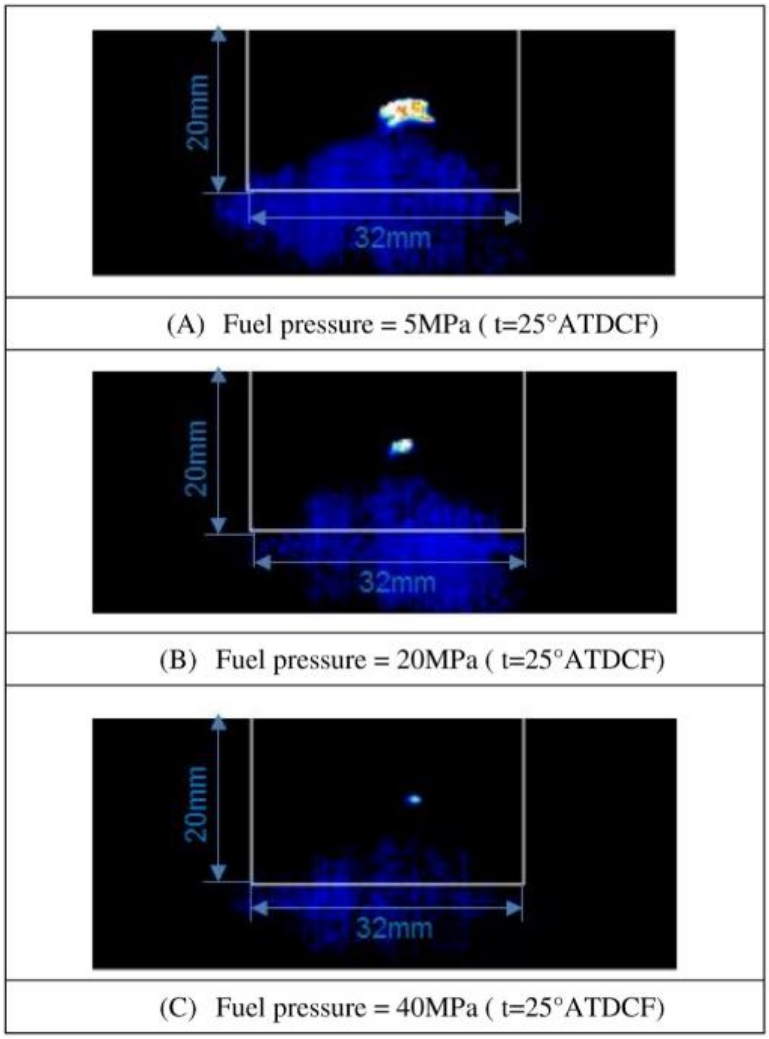

Figure 2.23: Endoscopic images of diffusion flames at injector tip surface because of injector tip wetting for three different injection pressures [50]

From the brief review above, it is generally observed that the correlations observed between tip wetting, the resulting PN and tip deposit are mainly qualitative. In addition, no direct measurement or quantification of the amount of injector deposit was observed. Nonetheless, the previous studies provide strong evidence that injector tip wetting contribute to soot formation and emission.

2.4.5 Modeling of Injector Tip Wetting, Tip Drying, and Deposit Growth on the Injector Tip

Modeling of injector tip wetting, tip drying and deposit growth on the GDI injector tip is another scarce area. This might be due to the complexity of the process and the unknown/unclear

physics of injector tip wetting and deposit formation. In terms of injector tip wetting and drying modeling, the most relevant work found in literature is the recent work by Fischer and Thelliez [51]. In their work, a complex chain of simulation tools was used to simulate fuel film formation and evaporation on the injector tip from the start of injection to ignition. The complex 3D CFD simulation procedure consisted of three consecutive parts. (1) In the first part, the injector nozzle geometry is modeled and fluid flow in the nozzle is simulated using an Euler multiphase technique. The flow conditions inside the injector nozzle are important and will change depending on fuel rail pressure, affecting the ensuing fuel film formation. The results from this part are stored in what the authors called, nozzle files, where they are used as input for later simulations. (2) The second part consisted of spray simulations by a Lagrangian spray method and using the nozzle files from the first part. This is coupled with a wall film model for fuel film formation and evaporation. Good agreement between spray simulations and measurements verified correct nozzle files as well as good spray and wall film models. (3) In the last part, a full engine cycle is simulated using the input nozzle files and spray and wall film models. The boundary conditions used in the engine simulation are shown in Table 2.1. These boundary conditions are varied for a fixed engine speed and load of 3000 RPM and 10 bar BMEP.

Table 2.1: Boundary conditions used in injector tip wetting and drying simulation in [51]

Engine Case	Fuel Temp	Tip Temp*	Hole Temp*	EGR Rate	Intake Temp	Fuel
#	°C	°C	°C	%	°C	-
E1	-	150	110	0	30	No injection
E2	50	150	110	0	30	Iso-Octane
E3	50	150	110	20	30	Iso-Octane
E4	50	150	110	20	50	Iso-Octane
E5	80	150	110	0	30	Iso-Octane
E6	50	180	160	0	30	Iso-Octane
E7	50	210	180	0	30	Iso-Octane

*The wall temperatures are uniform and constant for each case

The major findings from this simulation work are summarized in Figure 2.24. Fuel and tip temperatures had the most significant reduction effect on fuel film formation and evaporation, with fuel temperature (case #E5) having higher effect than tip temperature (case #E6 and #E7). Case #E3 and #E4, having higher flow velocities, showed lower fuel film mass at the end of the injection event. However, charge motion in this case did not influence fuel film evaporation compared to the reference case #E2 that had lower gas flow velocities. This indicates that charge motion is important only during injection, where it affects the film distribution on the tip.

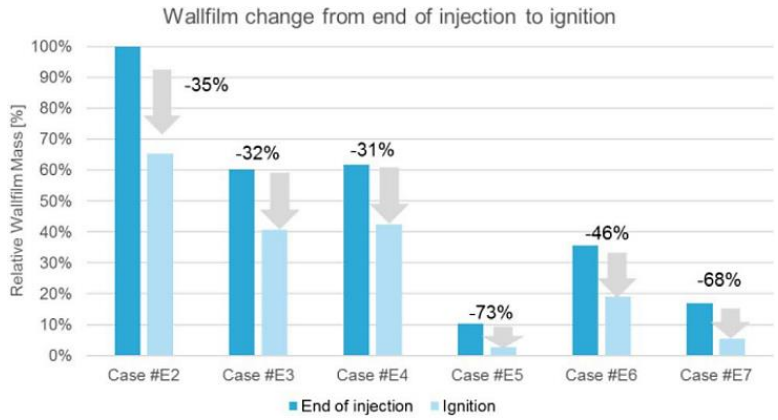

Figure 2.24: Change of fuel film mass (relative) from end of injection to ignition for boundary conditions in Table 2.1 [51]

In terms of modeling injector deposit formation, the model by Slavchov et al. [44], to our knowledge, is the only available model in the literature. The model is schematically shown in Figure 2.25. The model is based on liquid oxidation reactions at high temperatures, where the NOx formed during the combustion process transports to the quench layer of the liquid film, leading to fuel film degradation by reacting with the oxygen dissolved in it. The products of this liquid oxidation attach to the tip surface forming polar deposits. The model predicts deposit formation for two cases; adsorption and precipitation, and can be used to study the effect of deposit layer thickness on the rate fuel delivery and injector tip temperature. Worse deposit formation tendency was observed for branched alkanes compared to n-alkanes. More details on the chemical reactions and model development can be found in [44].

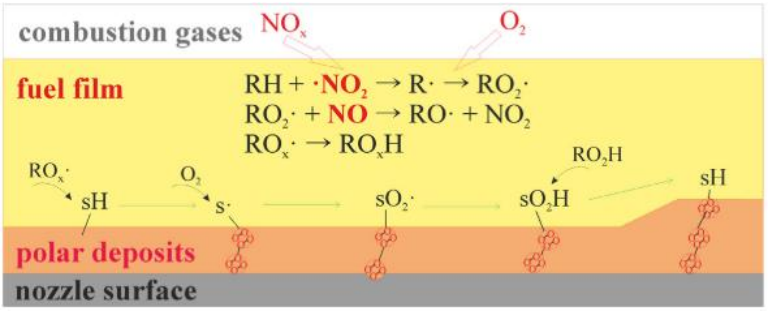

Figure 2.25: Deposit formation model proposed and developed by Slavchov et al. [44]

All other models, mainly focused on internal deposit formation, attempted to model the effect of deposit formation through modeling fuel flow rate loss. A model for injector plugging kinetics that describes the fuel flow rate loss was proposed by Aradi et al. [52] and was later adapted by Miura et al. [53]. Aradi et al. observed that temporal evolution of fuel flow rate loss followed an asymptotic behavior, starting with a fast initial flow rate loss followed by a stabilized flow rate loss after a certain period of time. An example for the described behavior is shown in Figure 2.26. This trend in flow rate loss was also observed in other research works [42,43,54–56].

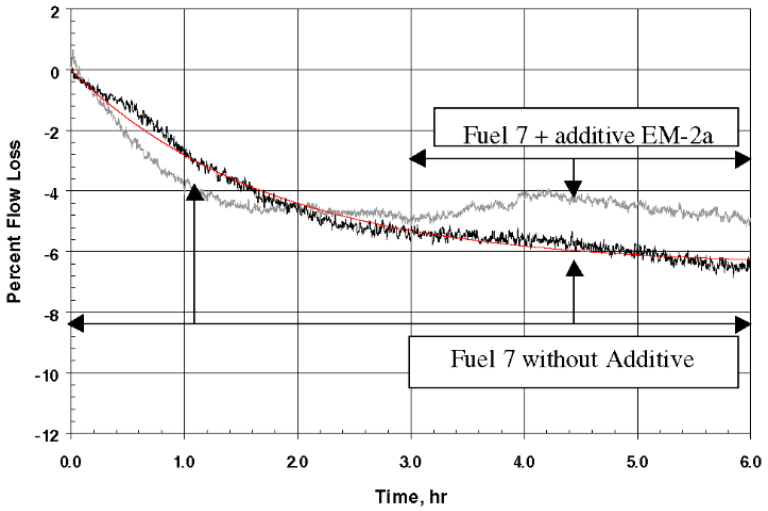

Figure 2.26: Percentage of fuel flow rate loss as a function of time starting with clean injectors [52]

2.5 Proposed Hypothesis for Liquid Film Evaporation on Fuel Injector Tip

In the literature review presented in Chapter 2, it is established that fuel films deposited on injector tip during the fuel injection process play an important role in soot formation and emission

from GDI engines. Therefore, managing the fuel film becomes crucial to reducing or eliminating PN emissions due to tip wetting. This can be done by either reducing or mitigating the initial fuel film that deposit on the tip during injection, or by evaporating all or most of the fuel film before ignition takes place. The former method requires a clear understanding of the dependence of the fuel film on injector nozzle parameters, which is still largely unclear as explained and analyzed in Section 2.4. On the other hand, fuel film evaporation from the injector tip depends on operating conditions of the engine and the injector such as in-cylinder pressure and temperature, engine speed, fuel properties, tip temperature, etc. Understanding of the physics of injector tip drying is therefore less ambiguous but remains a challenge. Clear understanding of tip drying physics can lead to significant reductions in PN emissions due to tip wetting.

The literature review on the physical mechanisms of tip drying and the work of Slavchov et al. [44] can be used as a guide to formulate a hypothesis on how the fuel film on the injector tip evaporates and leads to PN emissions. During an engine cycle, the combustion chamber pressure changes as the piston moves, as shown in Figure 2.13a. This causes the boiling point of the fuel film to increase with in-cylinder pressure, as Slavchov et al. highlighted in Figure 2.13b. The hypothesis is that the rate of fuel film evaporation reduces with time as the pressure (and the boiling point of the film) increases during the drying period, i.e. from end of injection to spark. Furthermore, in the peak pressure region or close to the spark timing, it is expected that no evaporation takes place since the boiling temperature of the film is much higher than the tip and fuel temperatures.

To validate this hypothesis, an attempt is made to model fuel film evaporation from the injector tip based on the evaporation and condensation theory. The model is then to be validated using two methods. First, the model is validated for isobaric evaporation by comparing with experimental data from literature, specifically from the work of Karwa et al. [41]. The second

method validates the model by performing engine experiments. Since direct fuel film mass measurements are difficult in a real engine, trend-wise comparisons with PN emissions and amount of deposit formed as a result of tip wetting are considered for the validation. The boundary conditions observed by other researchers for the wetted surface area and the initial film mass on the injector tip as well as other measured quantities such as fuel and tip temperatures are used as input to the developed model.

Chapter 3 Modeling of Liquid Film Evaporation on Fuel Injector Tip: Theoretical Approach

The proposed hypothesis was formulated as a theoretical model, which was then validated using experiments. In this chapter, the mathematical approach used in the theoretical model development is explained in details. The theoretical bases of the model are presented first, followed by the complete mathematical procedure. The solution algorithm used in the calculations is presented at the end of the chapter.

3.1 Fundamentals of Large Spherical Drop Evaporation

Naturally, the phenomenon of liquid drop evaporation involves many complexities. The physical processes involved are non-stationary with unequal temperature and vapor concentration gradients. In addition, conductive, convective and radiative heat transfer processes occur between the drop and the medium. For these reasons, idealized evaporation models had to be made using simplifying assumptions to form the basis of diffusion-controlled drop evaporation rate equations. These equations are often found to be valid for more complex, non-stationary evaporation processes. [57]

The basic theory begins with “quasi-stationary” assumption for drop evaporation and heat transfer. In this assumption, the rate of the process at any instance in time is considered equal to the rate of the stationary process with the boundary conditions attained at that instance. Maxwell [58] derived the general diffusion rate equation for a spherical drop in air that related the vapor concentration (or density) to the drop radial position. To derive the equation, Maxwell assumed that the concentration of the vapor at the drop surface was equal to the vapor equilibrium

concentration (i.e. the saturated vapor concentration at the drop surface temperature). Fuchs [59] showed that this assumption is applicable for large droplets, where the drop radius is much greater than the mean free path of the vapor molecules. For stationary evaporation process, the rate of mass transfer by evaporation was given by Eq. 3.1 [57].

$$\frac{dm}{dt} = A_s D \frac{d\rho}{dr} \dots (3.1)$$

where m is the mass [kg], t is the time [s], r is the radial distance from the center of the drop [m], $A_s = 4\pi r^2$ is the surface area of the spherical drop [m^2], D is the diffusion coefficient [m^2/s] and ρ is the vapor concentration [kg/m^3]. When air is the medium during drop evaporation, a mixture of vapor and air molecules forms the gas phase and the concentration equilibrium is locally reached at the drop-air interface. The diffusion of vapor molecules is therefore the rate-limiting process for drop evaporation.

3.2 Evaporation of a Cylindrical Liquid Film on Injector Tip

From experimental observations of liquid film surface area and thickness on the injector tip [11], the liquid film geometry differs significantly from spherical shape. The surface area of the liquid film is much higher than its thickness. A simple cylindrical geometry was found to be more representative of the liquid film shape. Therefore, the liquid film evaporating from the injector tip is assumed to have a cylindrical geometry as shown in Figure 3.1.

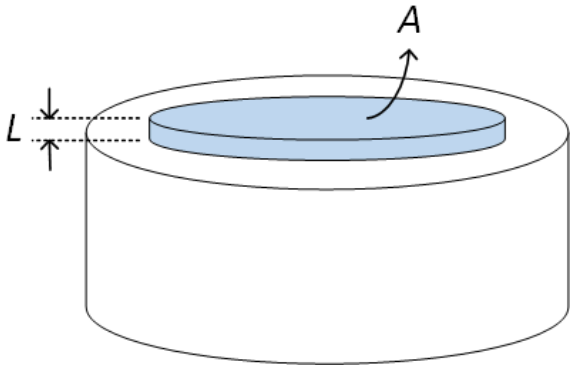

Figure 3.1: Assumed geometry of the liquid fuel film on the injector tip

In Eq. 3.1, which is based on spherical geometry, the drop radius was assumed to vary during evaporation. From the film geometry in Figure 3.1 evaporation is assumed to cause the film thickness to vary, with constant surface area of evaporation. Based on these assumptions, we can write an evaporation rate equation (Eq. 3.2), analogous to Eq. 3.1, for a cylindrical geometry.

$$\frac{dm}{dt} = A_s D \frac{d\rho}{dL} \dots (3.2)$$

where $A_s = \pi r^2$ is the surface area of evaporation [m^2] and L is the axial distance from the tip surface [m].

At the film surface ($L = L_s$), the vapor has concentration $\rho_{v,L}$. On the other hand, when the film is completely evaporated ($L = 0$), the vapor has concentration $\rho_{v,\mathrm{g}}$. Using these boundary conditions and the ideal gas relation ($\rho = \frac{\bar{M}}{RT} p$), Eq. 3.2 can be integrated to yield the rate of mass loss due to evaporation (Eq. 3.3).

$$\frac{dm}{dt} \int_0^{L_s} dL = A_s D \int_{\rho_\mathrm{g}}^{\rho_L} d\rho$$

$$\frac{dm}{dt} L_s = A_s D \left(\rho_{v,L} - \rho_{v,\mathrm{g}}\right)$$

$$\frac{dm}{dt} = \frac{\bar{M}}{RT} \frac{A_s D}{L_s} \left(p_{v,L} - p_{v,\mathrm{g}}\right) \dots (3.3)$$

where $\bar{M}$ is the average molecular weight of vapor [kg/mol], R is the universal gas constant [8.314 J/mol-K], T is the vapor temperature [K], $p_{v,L}$ is the liquid vapor pressure [Pa] and $p_{v,\mathrm{g}}$ is the pressure of vapor in gas [Pa].

Eq. 3.3 indicates that the difference in vapor pressure is the factor controlling the diffusion rate. If the vapor pressure in liquid-gas interface is greater than the vapor pressure in gas ($p_{v,L} > p_{v,\mathrm{g}}$), molecules will diffuse from the liquid surface to the gas (evaporation). In contrast, if the

vapor pressure in gas is greater than the liquid vapor pressure ($p_{v,L} < p_{v,g}$), molecules will diffuse from the gas to the liquid surface (condensation). This is shown schematically in Figure 3.2.

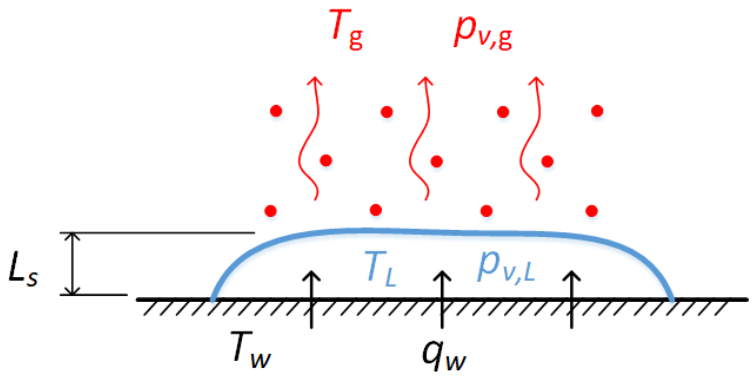

Figure 3.2: Physics of liquid film evaporation from injector tip. $p_{v,L} > p_{v,G}$ results in evaporation, whereas $p_{v,L} < p_{v,G}$ results in condensation

3.2.1 Assumptions and Boundary Conditions

A number of assumptions had to be made in order to find an analytical solution to Eq. 3.3. These assumptions are:

1) Quasi-stationary condition is assumed for all processes. As explained before, quasi-stationary condition assumes a stationary condition for the rates of mass and heat transfer at any moment in time at the boundary conditions obtaining at that moment. This allows for the solution of Eq. 3.3 assuming isothermal and isobaric conditions.
2) Surface area of evaporation is constant.
3) The liquid film and ambient gas are stationary i.e. motionless. The motionless liquid film assumption is supported by the fundamental experiments of injector tip wetting by Leick et al. [11] that showed that the film area stabilizes towards the end of injection.
4) Fuel properties are constant, and are taken at 90 °C and atmospheric pressure.
5) Heat transfer by conduction from the tip to the liquid film is the dominant heat transfer mechanism, and all other heat transfer mechanisms are considered negligible.
6) Heat transfer from the tip to the liquid film is one-dimensional.

7) Temperature gradient through the liquid film is constant.

Eq. 3.3 is subjected to the following boundary conditions:

$$t = 0 \Rightarrow m = 0$$

$$t = \infty \Rightarrow m = m_i$$

where m_i is the total mass evaporated after long time, which is the same as the initial liquid film mass the evaporation process started with [kg]. Based on experimental observations [11], this initial film mass is assumed to be 0.1% of the injected fuel mass.

3.2.2 Heat Transfer from the Tip to the Liquid Film

The main heat transfer mechanism for injector tip drying is the conduction heat transfer from the injector tip to the liquid film (Figure 3.3). Tip temperature is a significant parameter in the evaporation process since it affects the film temperature, which affects the liquid vapor pressure ($p_{v,L}$ in Eq. 3.3). In general, the rate of heat conduction through the liquid film is equal to the rate of heat change of the liquid film. Mathematically,

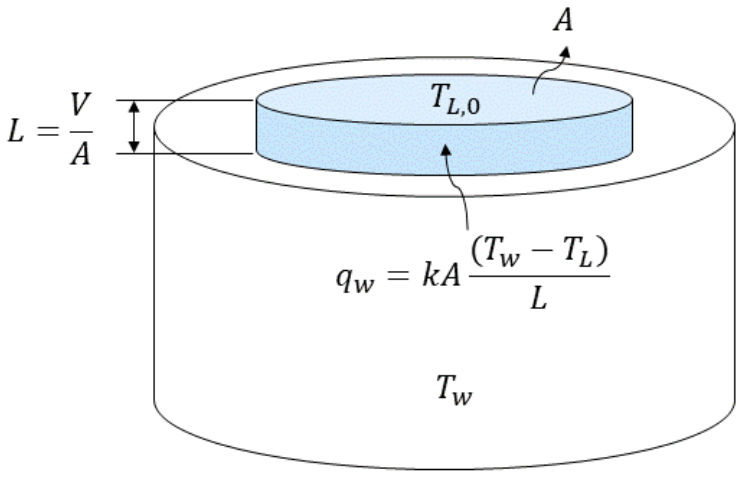

Figure 3.3: Conduction heat transfer (1-D) from the injector tip to the liquid fuel film

$$kA_s\frac{(T_w - T_L)}{L} = \rho V c_p\frac{dT_L}{dt} \ldots (3.4)$$

where k is the thermal conductivity of the liquid film [W/m^2-K], T_w is the tip or wall temperature [K], T_L is the liquid film temperature [K], ρ is the density of the film [kg/m^3], V is the volume of the liquid film calculated from ($V = {}^{m}/_{\rho}$) [m^3] and c_p is the specific heat capacity of the liquid film [J/kg-K]. Eq. 3.4 can be solved for $T_L(t)$ by integrating from the initial conditions $t = 0$ and $T_{L,0}$ to the final conditions t and T_L.

$$\int_{T_{L,0}}^{T_L} \frac{dT_L}{(T_w - T_L)} = \int_0^t \frac{kA}{\rho V c_p L} dt$$

$$T_L(t) = T_w \left(1 - e^{-\frac{k}{\rho L^2 c_p} t}\right) + T_{L,0} e^{-\frac{k}{\rho L^2 c_p} t} \quad \text{... (3.5)}$$

Therefore, at any instance in time, the film temperature changes according to Eq. 3.5. The film thickness also changes according to

$$L = \frac{V}{A_s} = \frac{m}{\rho A_s} \quad \text{... (3.6)}$$

3.2.3 Mass Transfer from the Liquid Film to the Gas

In Eq. 3.3, $p_{v,\mathrm{g}}$ can be expressed using the ideal gas relation as

$$p_{v,\mathrm{g}} = \frac{RT}{\bar{M} V_v} m \quad \text{... (3.7)}$$

where V_v is the vapor volume [m^3]. Substituting Eq. 3.7 into Eq. 3.3 and re-arranging yields

$$\frac{dm}{dt} + \frac{A_s D}{L_s V_v} m - \frac{A_s \bar{M}}{L_s RT} D p_{v,L} = 0 \quad \text{... (3.8)}$$

For stationary conditions (i.e. isothermal and isobaric evaporation), Eq. 3.8 represents a first-order ordinary differential equation (O.D.E.) in the form $a\frac{dm}{dt} + bm + c = 0$, where a, b and c are constants. The general solution of such O.D.E. can be written as

$$m(t) = C_1 e^{-\frac{b}{a}t} - \frac{c}{b}$$

subjected to the boundary condition $m(0) = 0$.

Following the above procedure, the general solution becomes

$$m(t) = \frac{\bar{M} V_v p_{v,L}}{RT}\left(1 - e^{-\frac{A_S}{L_S V_v} Dt}\right) \ldots (3.9)$$

In Eq. 3.9, all parameters are known or can be estimated except for the vapor volume V_v. However, Eq. 3.9 is a first-order asymptotic model with known features. One feature is that the term $\frac{\bar{M} V_v p_{v,L}}{RT}$, which has unit of mass [kg], represents the asymptotic value of the curve. In our case, this value is the final mass evaporated or alternatively the initial film mass that needs to be evaporated, which is known. From this understanding, if we let $m^* = \frac{\bar{M} V_v p_{v,L}}{RT}$, the vapor volume can be calculated according to Eq. 3.10.

$$V_v = \frac{RT}{\bar{M} p_{v,L}} m^* \ldots (3.10)$$

Thus, the final equation that describes the mass loss due to evaporation becomes

$$m(t) = m^*\left(1 - e^{-\frac{A_S}{L_S V_v} Dt}\right) \ldots (3.11)$$

3.2.4 Diffusion Coefficient Estimation

The diffusion coefficient (D in Eq. 3.11) is estimated from the theory of diffusion for binary gas systems at low to moderate pressures [60]. The Chapman and Enskog theory estimates the diffusion coefficient as

$$D_{AB} = \frac{0.00266 T^{3/2}}{p M_{AB}^{1/2} \sigma_{AB}^2 \Omega_D} \ldots (3.12)$$

where D_{AB} is the diffusion coefficient of gas A diffusing in gas B [cm^2/s], T is the temperature [K] and p is the pressure [bar]. M_{AB} is the net molecular weight [g/mol] defined as

$$M_{AB} = 2\left[\left(\frac{1}{M_A}\right) + \left(\frac{1}{M_B}\right)\right]^{-1} \ldots (3.13)$$

where M_A and M_B are the molecular weights of gas A and B, respectively. σ_{AB} is the average characteristic Lennard-Jones length [Å]

$$\sigma_{AB} = \frac{\sigma_A + \sigma_B}{2} \ldots (3.14)$$

where σ_A and σ_B are the characteristic Lennard-Jones lengths for gas A and B, respectively.

Ω_D is the diffusion collision integral, which is a dimensionless parameter function only of kT/ε_{AB}, where k is the Boltzmann constant and ε_{AB} is the net characteristic Lennard-Jones energy [J] defined from

$$\varepsilon_{AB} = (\varepsilon_A \varepsilon_B)^{1/2} \ldots (3.15)$$

where ε_A and ε_B are the individual characteristic Lennard-Jones energies for gas A and B, respectively. Ω_D is therefore given by [60]

$$\Omega_D = \frac{A}{(T^*)^B} + \frac{C}{e^{DT^*}} + \frac{E}{e^{FT^*}} + \frac{G}{e^{HT^*}} \ldots (3.16)$$

Where

$T^* = kT/\varepsilon_{AB}$	$A = 1.06036$	$B = 0.15610$
$C = 0.19300$	$D = 0.47635$	$E = 1.03587$
$F = 1.52996$	$G = 1.76474$	$H = 3.89411$

Appendix A tabulates the values of σ and ε/k for a number of pure substances.

3.2.5 Fuel and Gas Properties

The two working fluids used in the analysis were EPA Tier III premium certification gasoline and air. The Supplier Certificate of Analysis provided a number of properties for EPA Tier III premium certification gasoline, which allowed the calculation of other important chemical and thermal properties. For example, the average molecular weight of EPA Tier III premium certification gasoline (114.22 g/mol) was calculated based on its hydrogen, carbon and oxygen content data taken from Supplier Certificate of Analysis, which were measured using ASTM

D5291 (for H and C) and ASTM D4815 (for O) test methods. However, properties of isooctane as a surrogate fuel were used as needed whenever the Supplier Certificate of Analysis did not include the required property. The choice of isooctane was based on the enthalpy of vaporization comparison between EPA Tier III premium certification gasoline and isooctane. Fatouraie et al. [61], measured the heat of vaporization for a number of fuels, including EPA Tier III premium certification gasoline, and its value was found to be 37.2 kJ/mol at 15 °C. The value of enthalpy of vaporization for isooctane on the other hand is very well documented in literature [62] and it equals to 35.9 kJ/mol at the same temperature. The percentage difference between the two values is around 3.6%, which is acceptable. Thermal properties for isooctane used in the analysis are tabulated in Appendix A.

As presented in Section 3.2.4, the diffusion coefficient calculation required the knowledge of two-gas system properties, specifically the characteristic Lennard-Jones length and energy. In this case, the vapor molecules of isooctane were assumed to diffuse in the gas molecules of air. Lennard-Jones length and energy for air are well documented in [60] and are also shown in Appendix A. On the other hand, the corresponding properties for isooctane were unavailable and had to be estimated.

Leonard et al. [63] developed relationships between the Lennard-Jones force constants (length and energy) and the critical properties of the gas i.e. critical temperature, critical molar volume and critical pressure. The relationships were used in this work for the calculation of the Lennard-Jones constants for isooctane. These relationships are

$$\sigma = 0.1866 v_c^{1/3} z_c^{-6/5} \quad \ldots (3.17)$$

$$\frac{\varepsilon}{k} = \frac{0.424 T_c v_c}{\sigma^3} \quad \ldots (3.18)$$

where T_c is the critical temperature of the gas [K], v_c is the critical molar volume of the gas [cm^3/g-mol] and z_c is the compressibility factor of the gas calculated from

$$z_c = \frac{p_c v_c}{10 R T_c} \ldots (3.19)$$

where p_c is the critical pressure of the gas [bar]. Appendix A tabulates the critical properties used to calculate the Lennard-Jones potentials for isooctane for the calculation of the diffusion coefficient.

The liquid vapor pressure is another important property that show up in Eq. 3.10, which needed to be estimated. Antoine equation (Eq. 3.20) was used for this purpose.

$$\log_{10}(p_{v,L}) = A - \frac{B}{T_L + C} \ldots (3.20)$$

where A, B and C are the Antoine parameters and T_L is the liquid temperature [K]. Appendix A presents the Antoine parameters (provided by NIST) used for the calculation of the liquid vapor pressure for isooctane.

3.2.6 Estimation of In-Cylinder Gas Temperature

The vapor temperature is a required parameter in Eq. 3.10, Eq. 3.12 and Eq. 3.16. In the current analysis, the vapor temperature assumes the in-cylinder gas temperature. Therefore, it is important to estimate its value. For this purpose, an internal **B**osch **e**ngine **C**ombustion **A**nalysis **T**ool (BeCAT) was used to calculate the in-cylinder gas temperature from the measured in-cylinder gas pressure. The BeCAT is based on the work of Kulzer [64], where it can be used to perform different kinds of combustion analyses such as pressure trace statistics, burn rate analysis, gas exchange analysis, etc.

To calculate the in-cylinder gas temperature, two analyses are relevant: the gas exchange analysis and the burn rate analysis. The former analysis estimates the mixture gas temperature during the gas exchange period of the engine cycle as well as the mass residuals at the end of the

gas exchange. The burn rate analysis on the other hand can be used to estimate the gas temperature during the closed portion of the engine cycle. Both analyses estimate the gas temperature by solving the first law of thermodynamics, the ideal gas law, the mass balance and energy balance equations. More information about the equations and detailed calculation procedure can be found in [65].

3.3 Evaporation Time Constant: A Deterministic Factor

In Section 3.2, it was briefly mentioned that Eq. 3.9 (or 3.11) has the features of a first-order asymptotic model. In general, first-order asymptotic models are written in the form of Eq. 3.21.

$$m(t) = m^*\left(1 - e^{-t/\tau_c}\right) \ldots (3.21)$$

where $m(t)$ is the instantaneous value and m^* is the asymptotic value at $t = \infty$. τ_c is the time constant, which is the time needed for the instantaneous value to reach 63.2% of its asymptotic value. By comparing Eq. 3.11 and Eq. 3.21 and using Eq. 3.10, an evaporation time constant can be introduced as

$$\tau_c = \frac{L_s}{A_s D}\frac{RT}{\bar{M}p_{v,L}}m^* \ldots (3.22)$$

Using Eq. 3.12 in Eq. 3.22 yields

$$\tau_c = \frac{\sigma_{AB}^2\Omega_D}{0.00266}\frac{L_s}{A_s}\frac{R}{T^{1/2}}\frac{p}{p_{v,L}}\frac{M_{AB}^{1/2}}{\bar{M}_A}m^* \ldots (3.23)$$

By minimizing this time constant, the fuel film evaporation is maximized and PN emissions are minimized.

3.4 Solution Algorithm

MATLAB was used to implement a solution algorithm (see Appendix B for the MATLAB code) that solves all relevant equations presented in Section 3.2 and Section 3.3. Figure 3.4 shows the discretized time domain used in the algorithm. The specific solution procedure is as follows:

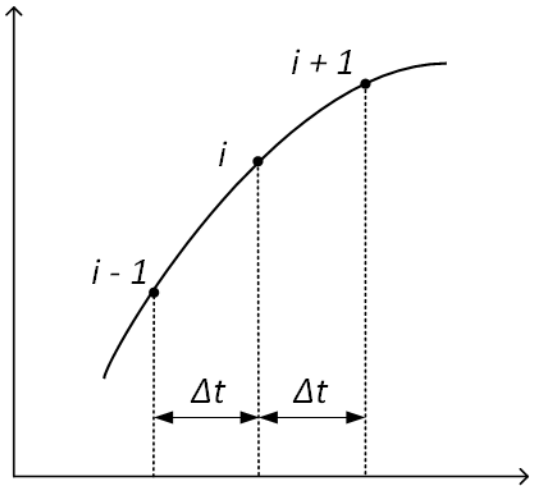

Figure 3.4: Discretized time domain used in the solution algorithm

(1) First, the in-cylinder gas temperature is estimated using BeCAT.

(2) Then, all data are imported into MATLAB for analysis. The imported data are:

a. Crank angle data.

b. Measured in-cylinder gas pressure.

c. Calculated in-cylinder gas temperature.

d. Measured PN.

e. Measured deposit volume.

f. Measured tip and fuel temperatures.

g. Engine speed.

h. Engine load.

i. Injected fuel mass.

j. End of injection (EOI) timing.

k. Spark timing.

l. Fuel and gas properties.

(3) After that, the individual Lennard-Jones length and energy constants for isooctane are calculated using Eq. 3.17 and Eq. 3.18.

(4) Then, the net Lennard-Jones length and energy constants are calculated from Eq. 3.14 and Eq. 3.15 using the individual Lennard-Jones constants for isooctane and air.

(5) The net molecular weight is calculated from Eq. 3.13.

(6) Initial film mass on injector tip and surface area of evaporation are calculated/assumed based on experimental observations:

a. Initial film mass equals to 0.1% of the injected fuel mass.

b. Surface area of evaporation is within 2 to 3 mm^2.

(7) The relevant equations are solved at each point in time (i = 1, 2, …, n) in the following order:

a. Liquid film temperature: $T_{L,i} = T_w\left(1 - e^{-\frac{k}{\rho L_i^2 c_p}t}\right) + T_{L,0}e^{-\frac{k}{\rho L_i^2 c_p}t_i}$

b. Liquid vapor pressure: $p_{v,L,i} = 10^{A - \frac{B}{T_{L,i}+C}}$

c. Vapor volume: $V_{v,i} = \frac{RT_i}{\bar{M}_{C_8H_{18}} p_{v,L,i}} m^*$

d. Collision integral: $T_i^* = \frac{T_i}{\left(\frac{k}{\varepsilon_{AB}}\right)_i}, \Omega_{D,i} = \frac{A}{\left(T_i^*\right)^B} + \frac{C}{e^{DT_i^*}} + \frac{E}{e^{FT_i^*}} + \frac{G}{e^{HT_i^*}}$

e. Diffusion coefficient: $D_{AB,i} = \frac{0.00266 T_i^{3/2}}{p_i M_{AB,i}^{1/2} \sigma_{AB,i}^2 \Omega_{D,i}}$

f. Mass evaporated: $m_i = m^*\left(1 - e^{-\frac{A_S}{L_i V_{v,i}} D_{AB,i} t_i}\right)$

g. New film thickness: $L_{i+1} = L_i - \frac{m_i}{\rho A_S}$

(8) The solver solves the previous equations for the whole time domain, and the mass on the tip at each time is predicted and the evaporation curve is constructed.

(9) After that, the fuel film mass remaining before the time of spark is determined. For all cases, it was observed that as pressure increases during the compression stroke, mass was added by condensation. Therefore, based on the assumption that no condensation occurs and in-cylinder gas motion assists in evaporation, the film mass that burns into a diffusion flame resulting in PN was assumed to be the minimum mass predicted between EOI to spark timing. i.e.

$$m_{@\,SPA} = \min(m_i)\,, i = 1, 2, \dots, n$$

(10) Comparisons between predicted film mass at the time of spark, and measured PN and deposit volume are then performed and quantitative correlations are calculated.

Chapter 4 Quantifying Particulate Formation and Deposition on the Injector Tip: Experimental Approach

Measurement of fuel film mass on injector tip of a GDI engine includes many experimental uncertainties, as shown by Leick et al. [11]. Therefore, to validate the theoretical model during an engine cycle, trends in predicted film mass calculated from the model were compared with trends in measured engine-out PN and injector deposit volume at different operating conditions. A combination of engine experiments and 3D digital microscopy techniques was used for this purpose.

Engine tests were performed at the R&D facility of Robert Bosch LLC in Farmington Hills, Michigan, USA. A schematic diagram for the experimental setup used to conduct engine experiments is shown in Figure 4.1. Multi-cylinder engine experiments were performed in an engine dynamometer cell, and tests were controlled from computers outside the cell.

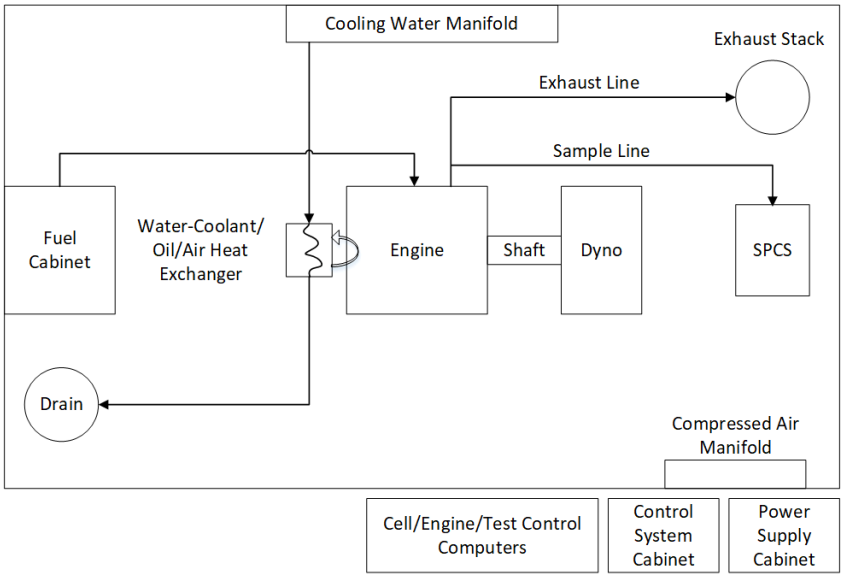

Figure 4.1: Schematic diagram showing the experimental setup used to conduct engine experiments

A 4-cylinder turbocharged GDI engine with centrally mounted injectors was used for engine experiments. A sample of engine exhaust was directed into a solid particle counting system (SPCS) to measure engine-out PN. Injector deposits were also quantified by measuring the volume of deposit formed on the injector tip using 3D digital microscopy. All engine experiments were performed using EPA Tier III premium certification gasoline, which has known and consistent properties. In addition, injector tip and fuel temperatures were measured using an instrumented GDI fuel injector. These temperatures were used as boundary conditions in the theoretical model.

4.1 Particulate Number (PN) Measurement

PN concentration was measured using the solid particle counting system MEXA-2100SPCS from Horiba, Ltd, where the PN is reported in number per cubic centimeter (#/cm^3). The SPCS system is based on laser scattering condensation particle counting (CPC) principle, in which particles are enlarged by condensation from a nanometer scale to a micrometer scale. The enlarged particles are then exposed to a laser beam where the particles cause the light to be scattered. From the light scattering theory, the number of particles can be estimated. The SPCS system has a lower particle size limit of 23 nm. The CPC principle used in the SPCS system is the same principle of operation used for vehicle certification. More information regarding the functionality and limitations of this device is found in [66].

A sample of engine exhaust (post-turbo) was directed into the SPCS system to measure engine-out PN in a 1 Hz data acquisition. The reported PN measurement represents a 30-second time average. The exhaust sample fluid was diluted for all engine experiments using a dilution ratio of 1500. The temperature of the exhaust at the sampling location was dependent on the operating point. Nonetheless, the diluted sample had a temperature of 190 °C for all engine experiments.

4.2 Volume Measurement of Injector Tip Deposit

In this work, as engine operated at a steady state operating point, injector deposit formed on the tip as time passed. The amount of this deposit, if correlated well with the measured PN, would be a good indicator of injector tip wetting at the operating point tested. As a result, trends in measured deposit volume can also be used to validate the theoretical model.

A novel experimental technique, based on 3D digital microscopy, is introduced to quantify the amount of deposit on the injector tip, while showing at the same time the deposit's macroscopic morphology and how it differs for various operating conditions and steady state coking times.

The digital microscope VHX-2000 from Keyence Inc. (Figure 4.2) is capable of automatically imaging a user-defined region (2D or 3D), a process called "image stitching", in addition to providing post-processing functions after images are taken.

Figure 4.2: VHX-2000 digital microscope and its components

The 3D imaging procedure works as follows. First, the user selects "3D Image Stitching" option in the microscope computer main screen. Then, the user defines three things:

(1) The four boundaries of the region to be imaged in the X- and Y- directions (see Figure 4.3). This sets the X and Y coordinates of the desired region with respect to the origin (center of

camera). Based on these coordinates, the region is divided into a number of pictures (frames) in the XY region. The number of frames depend on the lens magnification magnitude and the actual XY distance defined by the user. Higher magnification and larger XY distance result in larger number of frames. It should be mentioned that the camera is fixed in the X- and Y-directions, and the motorized stage is the one having motion in the XY plane.

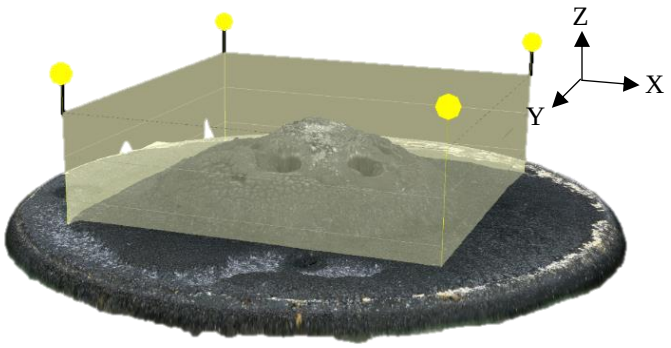

Figure 4.3: 3D coordinates of the injector tip position and the rectangular prism used to enclose a desired 3D region for volume measurement

(2) The top and bottom boundaries of the 3D region to be imaged in the Z-direction. This sets the Z coordinates of the desired 3D region. The top and bottom boundaries should be selected in a way that the camera is able to focus and clearly capture any part of the desired 3D region in its corresponding XY plane between the two boundaries.

(3) A focal depth step, called “pitch”, in the Z-direction. The pitch is defined as the distance between any two focused images in the Z-direction. This pitch is used by the camera’s motorized focus adjuster to scan through the desired 3D region, from bottom boundary to top boundary. The selection of this pitch has a significant effect on the resolution and quality of the 3D image.

Once these options are clearly defined, the user selects “Start Automatic Image Stitching” option, which starts the 3D imaging process.

The way the camera scans through the 3D region is by first moving the motorized stage to the starting point, which is the left-top frame in the XY region. Starting with that frame, the

motorized focus adjuster adjusts the camera's focus to start from the bottom boundary and then scan through the 3D region in the Z-direction to the top boundary, with a step size equals to the pitch between each focused image. The number of images in the Z-direction is proportional to the number of steps and the minimum and maximum coordinates in the Z-direction.

After the camera records all images (in Z-direction) in the first frame, the motorized stage moves in the X-direction (to the left) so that the next frame can be imaged. The camera's motorized focus adjuster also moves to the bottom boundary to start the imaging process for the new frame again. This automatic imaging process scans through each row (X-direction) and column (Y-direction) until all frames are captured and the full 3D image is constructed (see Figure 4.4).

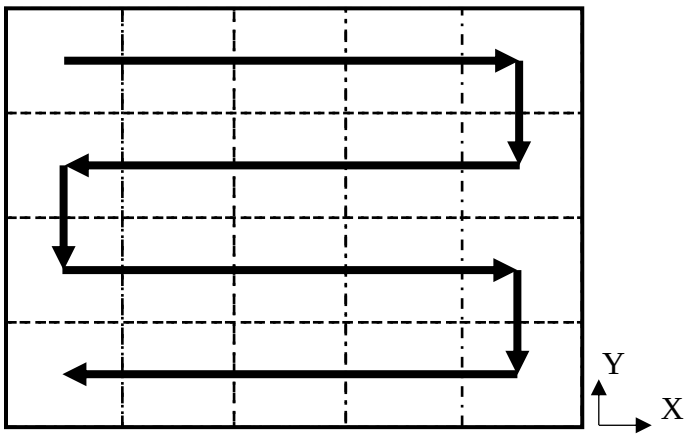

Figure 4.4: Direction of camera scanning process through the different frames in the XY plane. For each frame, the camera scans the 3D space from bottom boundary to top boundary

The total number of images taken by the microscope for the desired 3D region would be

$$\textit{Total number of images} = \textit{number of images in one frame} \times \textit{number of frames in X-direction} \times \textit{number of frames in Y-direction}$$

4.2.1 3D Resolution and Pitch Independence Test

The selection of the pitch in the Z-direction can have a significant influence on the resolution and quality of the 3D image. The smaller the step size, the better the 3D image. For this reason, a pitch independence test was performed at X200 magnification to select a pitch value that

results in a good quality image with optimal imaging time. The test started with a pitch size of 400 µm until a pitch of 12 µm. Table 4.1 shows the different pitch sizes used in the pitch independence test.

Table 4.1: Step sizes used in the pitch independence test

Pitch [µm]
400
200
100
50
25
12

A coked injector was used in this test and the imaged region used for comparison is shown in Figure 4.5. The resulting 3D images for the different step sizes are shown in Figure 4.6. The figure shows that the quality of the 3D image improved and better 3D resolution was achieved as the step size reduced. For a pitch size of 50 µm and lower, the 3D images were very similar qualitatively, and no distinguishable difference was observed.

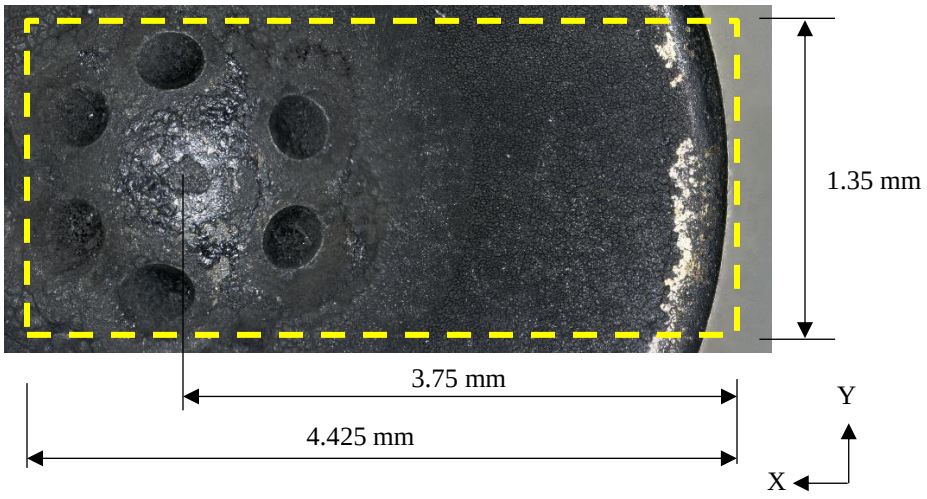

Figure 4.5: Region in a coked injector used in the volume independence test

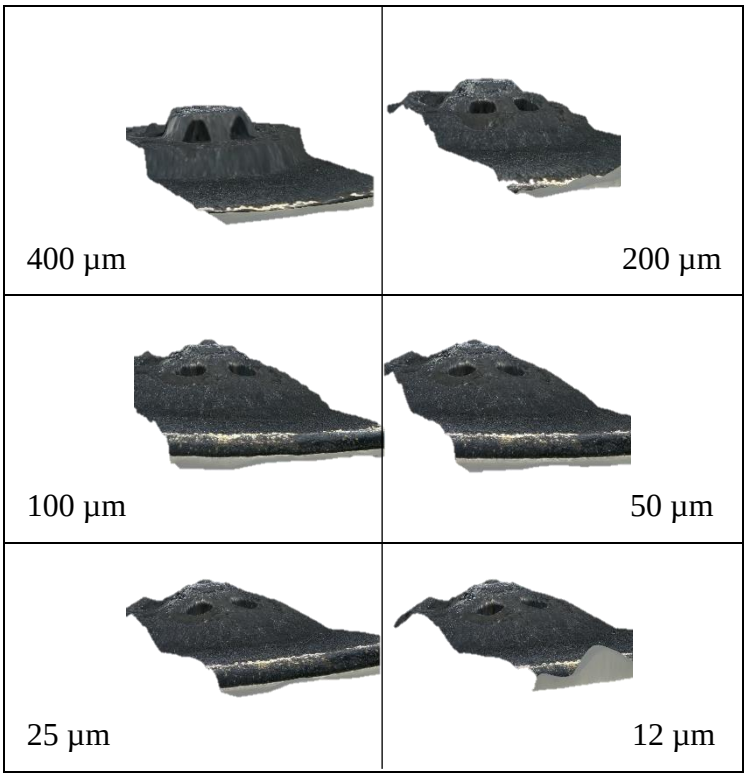

Figure 4.6: Quality of the 3D images of the injector region imaged for the different step sizes

A quantitative comparison was also performed by measuring the absolute volume of the imaged region for each step size. A post-processing function provided by the microscope software allows the volume to be measured by enclosing a 3D region within a user-controlled rectangular prism, as can be seen in Figure 4.3.

The volume calculation function works based on the fact that the constructed 3D image has known coordinates from the previously defined XYZ boundaries. The rectangular prism has also known coordinates that change by changing the XYZ planes of the prism. Therefore, the intersection between the prism's planes and any part of the imaged 3D region is known and is used to calculate its volume.

Three trials were performed to measure the volume of the enclosed region shown in Figure 4.3 for each step size in Table 4.1. The results are summarized in Table 4.2. The results show the percentage difference in volume measurement between any two consecutive pitch sizes. In general,

the measured volume converged as the step size reduced, with the less than 2% difference in volume for pitch size of 50 µm and smaller. Therefore, 50 µm was selected as the optimum pitch size for future volume measurement.

Table 4.2: Percentage difference in volume measurement between each two consecutive step sizes

Step Size	**Volume Difference [%]**		
	Trial 1	**Trial 2**	**Trial 3**
400 – 200	31.7	23.5	33.4
200 – 100	30.7	23.3	30.1
100 – 50	0.85	1.10	2.13
50 – 25	1.35	0.95	0.87
25 – 12	0.50	1.47	0.64

4.2.2 Uncertainty in Volume Measurement

Two sources of uncertainty in volume measurement were identified and were added as error bar for each measurement point. The sources were the systematic error due to the automatic 3D image stitching, and the random error due to manually placing the XYZ planes of the rectangular prism. In order to assess the first type of uncertainty, the human error had to be isolated. This was performed by repeatedly imaging a fixed 3D region (shown in Figure 4.7), and measuring the volume for the complete 3D region defined by the XYZ coordinates, eliminating the need to manually placing the XYZ reference planes of the prism.

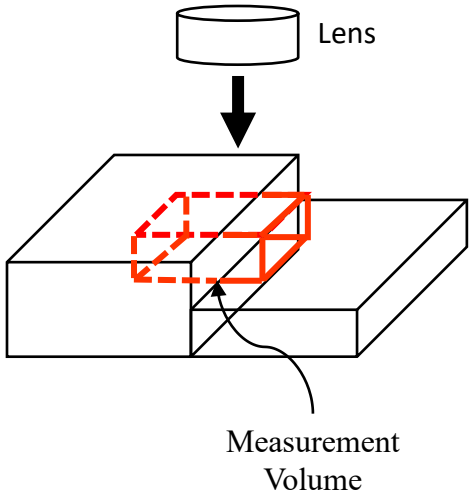

Figure 4.7: Fixed volume used to identify the uncertainty in the automatic 3D image stitching

The region shown in Figure 4.7 was imaged a number of times and its volume was defined as

$$V_{avg} \pm \varepsilon_a$$

where V_{avg} is the average volume for all repeated measurements, and $\varepsilon_a = \text{SD}$ is the automatic stitching error, taken as one standard deviation (SD) for the repeated volume measurements. The percentage systematic error were finally found from

$$\frac{\varepsilon_a}{V_{avg}} \times 100$$

By performing six repeated measurements, the systematic error associated with the automatic 3D image stitching was found to be 1.1%. This percentage error was rounded to 2% and was added to the total uncertainty in any volume measurement later on.

The human error was also taken into account in the total uncertainty in volume measurement. This type of error was found by performing multiple placements of the XYZ reference planes of the prism and recording the measured volume a number of times. The human error therefore was calculated as

$$\varepsilon_h = SD$$

where SD is one standard deviation for the repeated volume measurements.

Finally, the total uncertainty in volume measurement that includes both types of error were defined as

$$\varepsilon_t = \sqrt{\varepsilon_a^2 + \varepsilon_h^2}$$

4.2.3 Volume Estimation of Injector Tip Deposit

The volume of deposit on a GDI injector tip was approximated by performing volume measurements of the injector tip at two different states: a clean injector tip and a coked injector tip (see Figure 4.8). The volume of the deposited carbon on the injector tip was then estimated as

$$V_{deposit} = V_{coked} - V_{clean}$$

with uncertainty

$$\varepsilon_{deposit} = \sqrt{\varepsilon_{t,coked}^2 + \varepsilon_{t,clean}^2}$$

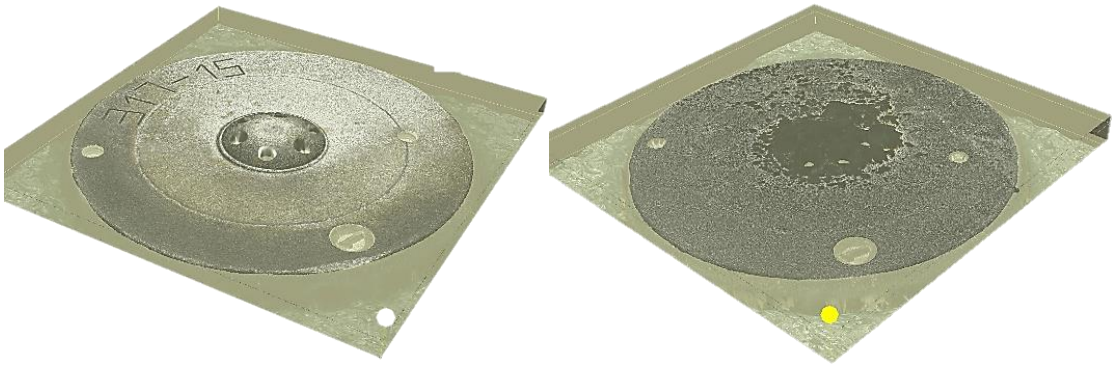

Figure 4.8: An example of 3D imaging of clean (left) and coked (right) injector tips

The engine-out PN from injector tip wetting is a result of tip wetting from all cylinders. Therefore, the average deposit volume for all cylinders was calculated according to

$$V_{deposit,avg} = \frac{1}{n}\sum_{i=1}^{n} V_{deposit,cyl(i)}$$

with uncertainty

$$\varepsilon_{deposit,avg} = \frac{1}{n}\sqrt{\sum_{i=1}^{n} \varepsilon_{deposit,cyl(i)}^2}$$

where n is number of cylinders and $V_{deposit,cyl(i)}$ and $\varepsilon_{deposit,cyl(i)}$ are the average deposit volume and its corresponding uncertainty, respectively, for injector in cylinder i.

4.3 Tip and Fuel Temperatures Measurement

A GDI injector was modified by instrumenting it with two K-type thermocouples for tip and fuel temperatures measurements (Figure 4.9). For consistency, this injector was installed in the same cylinder (cylinder 1, located farthest from the flywheel) for all engine experiments.

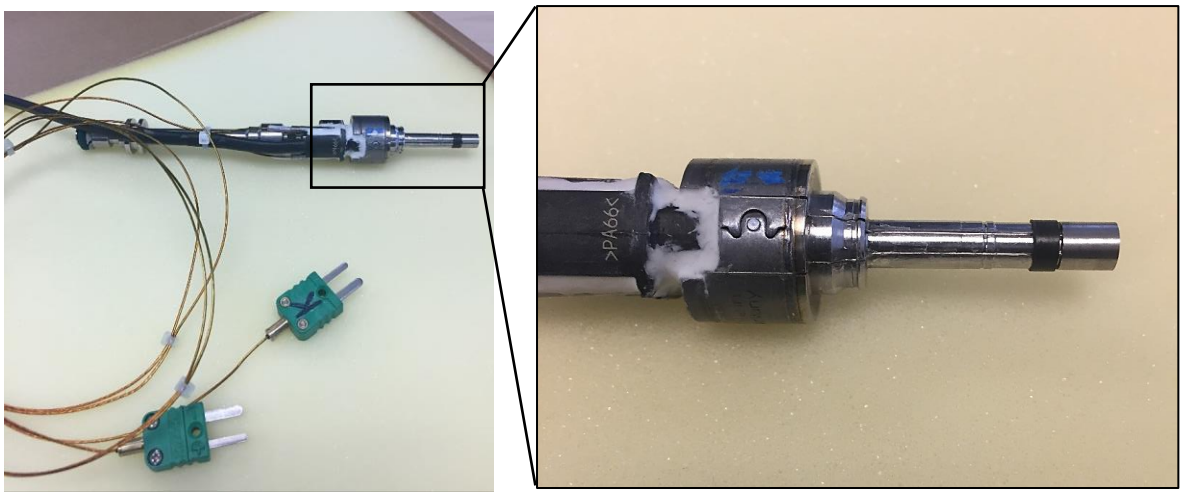

Figure 4.9: Instrumented GDI injector for tip and fuel temperatures measurement. The injector was installed in cylinder 1 for all engine experiments

The exact locations of the sensors are shown in Figure 4.10. The tip temperature sensor was placed 0.4 mm below the tip surface and 1.13 mm away from the external sidewall of the injector tip. The fuel temperature sensor on the other hand was installed just before the needle ball, 3.9 mm away from the tip surface. These temperatures were used in the initialization of the tip and fuel temperature boundary conditions in the validation of the theoretical model during engine cycle.

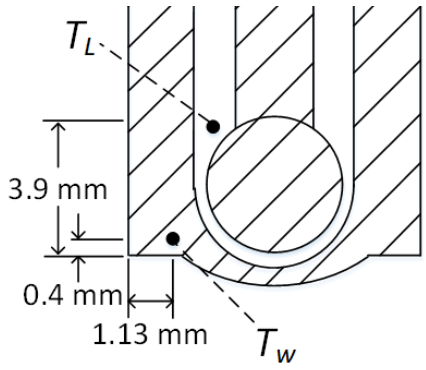

Figure 4.10: Locations of the tip and fuel temperature sensors in the instrumented GDI injector tip

4.4 Experimental Test Matrix

The objective for engine experiments was to perform a systematic variation of the initial film mass on tip (after end of injection) for a constant drying time i.e. period from end of injection to spark, as well as varying the drying time for a fixed initial film mass. This was achieved by varying engine load (characterized by brake mean effective pressure, BMEP) and engine speed. Different engine load demand leads to variation in injected fuel mass, which causes the initial film mass on injector tip to vary. Different injected fuel mass also leads to different peak gas temperatures, directly affecting chamber walls temperature, specifically the injector tip temperature. By varying the engine speed on the other hand, the absolute time allowed for fuel film evaporation is varied. The variations in engine load and speed lead to different levels of engine-out PN and deposit volume formed on the injector tip. Table 4.3 shows the experimental test matrix that includes systematic variation of engine load and speed. In particular, the engine loads and speeds tested were 6, 10, and 14 bar BMEP, and 1000, 2000, and 3000 RPM, respectively. It might be worth mentioning that at 1000 RPM, high loads (above 10 bar BMEP) could not be achieved due to the knocking at stoichiometric combustion at low engine speed. The remaining of the operating parameters were held constant, according to Table 4.4, at fuel rail pressure (p_f) of 200 bar, start of injection timing (SOI) of 290 CAD bTDC with reference to power storke, engine-out coolant (and oil) temperature (T_c) of 90 °C and single injection mode. These

operating parameters were selected for optimized PN emissions, and where tip wetting is the dominant PN formation mechanism. The PN optimization was performed by varying the SOI timing at any given load, and measuring the PN emissions. The effects of engine operating conditions on the different fuel wetting mechanisms have been confirmed using in-situ high speed imaging and the images are reported in Fatouraie et al. [67].

Table 4.3: Experimental test matrix used in engine experiments

SPEED [RPM] / BMEP [bar]	1000	2000	3000
6	Test 1	Test 2	Test 3
10	Test 4	Test 5	Test 6
14	-	Test 7	Test 8

Table 4.4: Operating parameters held constant when varying engine load and speed

p_f [bar]	SOI [CAD bTDC]	T_c [°C]	# Injections
200	290	90	1

4.5 Test Procedure

The test procedure was designed to achieve two objectives. The first objective was to build injector deposits that cause minimal PN drift. In this case, the deposits formed on the injector tip would be a good indicator of the amount of tip wetting, with minimal influence on engine-out PN when operating the engine at the desired operating points in Table 4.3. The measured PN at these different conditions should then correlate well with the corresponding measured deposit volume. The second objective was to cause variation in engine-out PN at different deposit levels but at the same operating point. In this way, the amplification effect of injector deposits on injector tip wetting can be observed quantitatively. The specific test procedure is shown as a timeline in Figure 4.11. The procedure included a steady state engine operation for five hours with intermittent stops at certain points in time (hour 1, 3 and 5) for injector tip imaging.

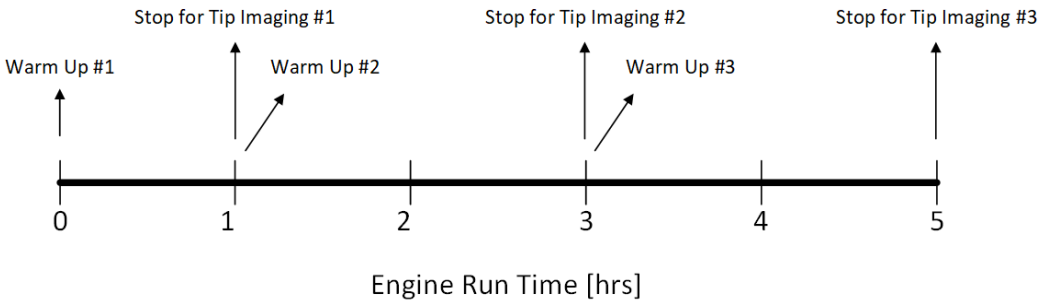

Figure 4.11: Timeline of engine test procedure

4.5.1 Engine Warmup Procedure

Before the beginning of the test, a set of clean multi-hole GDI injectors was installed in the engine at room temperature. The engine was then fired and warmed up for 10-12 minutes at low load and speed, i.e. 4 bar BMEP and 1000 RPM. The engine was considered warm when the engine-out coolant temperature reached the desired value of 90 °C. PN was recorded every one second throughout the warmup period. The engine warmup procedure was repeated every time the engine was stopped for injector tip imaging.

A sample plot of engine-out PN (in logarithmic scale) during engine warmup is shown in Figure 4.12. PN is shown as a function of engine-out coolant temperature. The results showed a spike in PN emissions during the startup phase, which decreased as the engine became hotter. One important feature of the warmup curve is that a stabilized PN level was reached when the engine-out coolant temperature exceeded 65 °C. Depending on the deposit level formed on the injector tip, this stabilized value of PN differed. This allowed the nature of increased tip wetting PN with deposit level to be explored in a quantitative manner. Tip and fuel temperatures were also measured and were observed to increase with engine-out coolant temperature during engine warmup. A sample plot showing both temperatures is given in Figure 4.13. It might be worth mentioning that both temperatures reached stabilized values after reaching a coolant temperature of 90 °C, but this is not reflected in the figure due to the data logging procedure implemented.

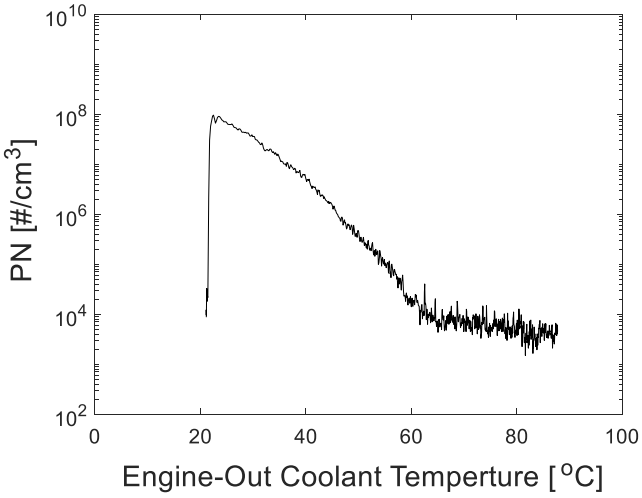

Figure 4.12: A sample plot of PN as a function of engine-out coolant temperature during engine warmup. Data for 4 bar BMEP and 1000 RPM at time 0 hrs (clean injector tip)

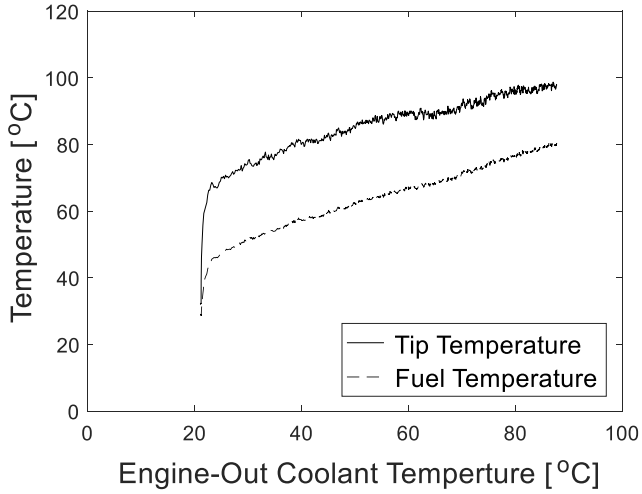

Figure 4.13: A sample plot of tip and fuel temperatures as a function of engine-out coolant temperature during engine warmup. Data for 4 bar BMEP and 1000 RPM at time 0 hrs (clean injector tip)

4.5.2 Injector Coking Procedure

After engine warmup, the engine was brought to the desired operating point of load and speed. The engine operated at this point steadily for the desired amount of time (1 hour after the start of the test, 2 hours after the first stop, and 2 hours after the second stop). During the steady state operation, the injector tip was coked and carbon deposit formed on the tip. In addition, PN was recorded every 5 minutes, and each reported PN represents a 30-second time average. An

example plot is shown in Figure 4.14, showing PN emissions as a function of time during the coking period. It is observed that PN level stayed within the same order of magnitude for the complete coking time of five hours. On the other hand, a sample plot for tip and fuel measurements during a coking period is shown Figure 4.15. Consistent temperature measurement is observed in general.

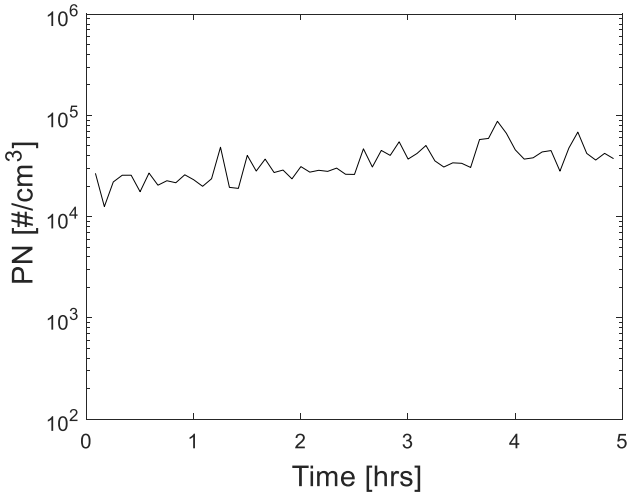

Figure 4.14: A sample plot of PN as a function of time during injector coking test. Data for 10 bar BMEP and 2000 RPM

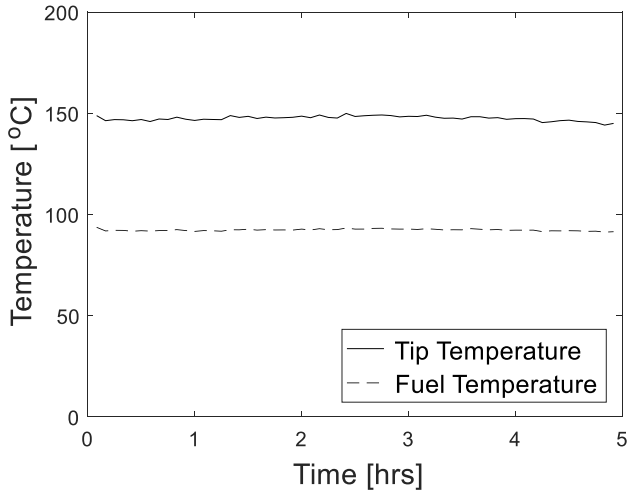

Figure 4.15: A sample plot of tip and fuel temperatures as a function of time during injector coking test. Data for 10 bar BMEP and 2000 RPM

4.5.3 Repeatability

To ensure the repeatability and consistency of measurements, the warmup procedure and coking procedure were repeated three times for 10 bar BMEP and 2000 RPM. Both the stabilized PN level at the end of the warmup test (last 60 seconds) and the PN during the coking period were found to be repeatable within a percentage error of around 20%, calculated from one standard deviation for all measurement points in time. This percentage error is within the expected range of deviation in the area of PN measurements for the SPCS. Tip and fuel temperatures on the other hand were found to be repeatable within 5%, calculated from one standard deviation. Therefore, error bars for PN measurements represent 20% error, while error bars for tip and fuel temperatures, if any, represent 5% error. Repeatability plots are shown in Appendix C for reference.

Chapter 5 Results and Discussion

This chapter presents the results of the theoretical model and the experimental measurements. The correlation results of PN and deposit volume are discussed first, followed by the validation of the evaporation model by comparison with experiments. Once validated, the evaporation model was used to perform a parametric study for the effect of operating conditions on liquid fuel film evaporation on injector tip. Lastly, an attempt was made to relate engine operation and calibration parameters to the evaporation time constant, which is the deterministic factor influencing the amount of fuel film remaining on the tip at the time of spark. By minimizing this factor, PN emissions could then be minimized.

5.1 PN and Deposit Volume Correlation

During steady state operation, engine experiments showed that injector tip wetting led to deposit formation on the injector tip. These deposits evolved with time during engine operation and eventually correlated well with engine-out PN at each varied operating condition (Table 4.3). To show this, PN was plotted against deposit volume ($V_{deposit}$) for all operating points in Figure 5.1. The figure shows the temporal evolution of the PN-$V_{deposit}$ correlation, characterized by R^2. The improved R^2 value with time shows that injector deposits were good indicators of the amount of tip wetting for the engine structure and the operating conditions tested. It also shows that injector tip wetting was the dominant PN formation mechanism for the operating points selected.

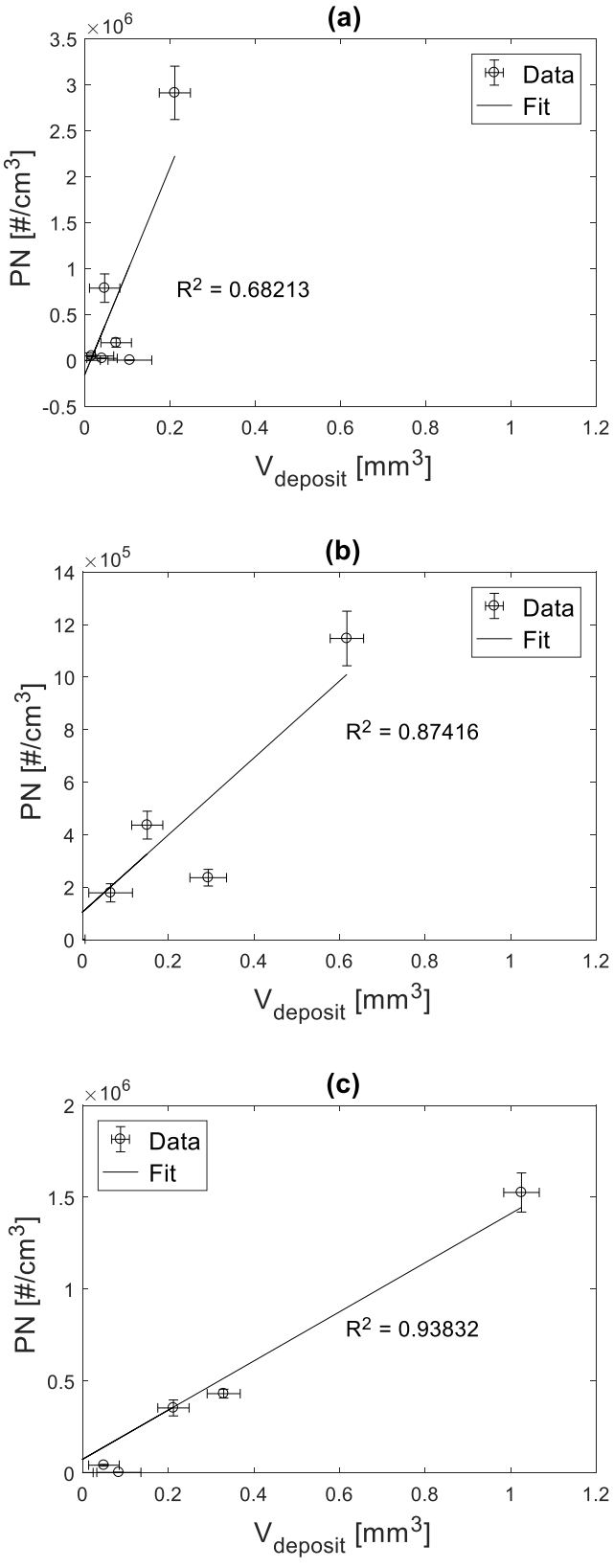

Figure 5.1: Temporal evolution of PN-$V_{deposit}$ correlation. R^2 is shown (a) after 1 hour, (b) after 3 hours and (c) after 5 hours. R^2 is observed to improve with time, indicating good one-to-one correlation between injector tip wetting (and deposit level) and engine-out PN

5.2 Model Validation

The theoretical model developed in Chapter 3 was validated using two methods. First, the model was validated for isobaric evaporation by comparison with evaporation times data from literature. The second method involved validating the model during an engine cycle by comparison with PN and deposit volume measurements at different operating conditions (Table 4.3). PN and deposit volume data after 5 hours of coking time (Figure 5.1c) were used in engine cycle validation.

5.2.1 Isobaric Evaporation

Evaporation or drying times data from the work of Karwa et al. [41] were used to validate the theoretical model for liquid film evaporation at isobaric conditions i.e. constant system pressure. Data existed for two system pressures: 0.8 and 1.0 bar. For each system pressure, evaporation time of isooctane in quiescent air was measured at different tip temperatures. The specific boundary conditions used in the validation are detailed in Table 5.1. Other conditions were held constant at (Table 5.2) initial film mass of 3.44 mg, initial film temperature of 25 °C and air temperature of 25 °C.

Table 5.1: Boundary conditions used in the validation of the evaporation model for isobaric conditions

System Pressure [bar]	**0.8**	**1.0**
Tip Temperature [°C]	60	80
	80	110
	110	130
	130	150
	140	160
	150	-

Table 5.2: Boundary conditions held constant when varying the system pressure and tip temperature

Fuel	Isooctane
Initial Film Mass [mg]	3.44
Wetted Surface Area	40 – 50 % of HDEV5 Bosch injector tip surface area
Initial Film Temperature [°C]	25
Air Temperature [°C]	25

The wetted surface area was approximated as 40 – 50 % of the surface area of HDEV5 Bosch injector tip. These values were used based on image processing of the snap shots of the wetted area, as shown in Figure 5.2.

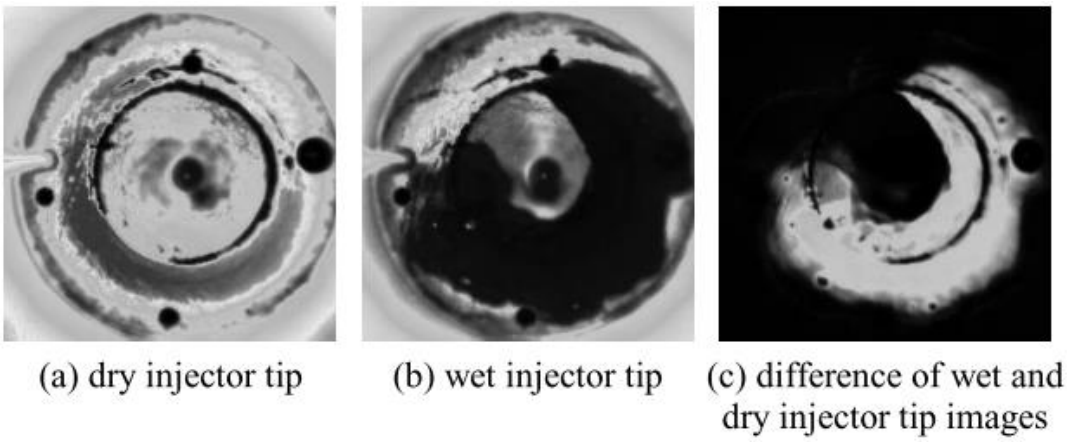

Figure 5.2: Images of the HDEV5 Bosch injector tip showing (a) dry injector tip, (b) wet injector tip with the wetted area shown in black color and (c) difference of wet and dry injector tip images with the wetted area shown in white color. The film area shown to covers 40 – 50 % of the injector tip area [41]

Each operating condition had an evaporation curve similar to the one in Figure 5.3. The drying time was defined as the time it took to evaporate 99% of the initial film mass.

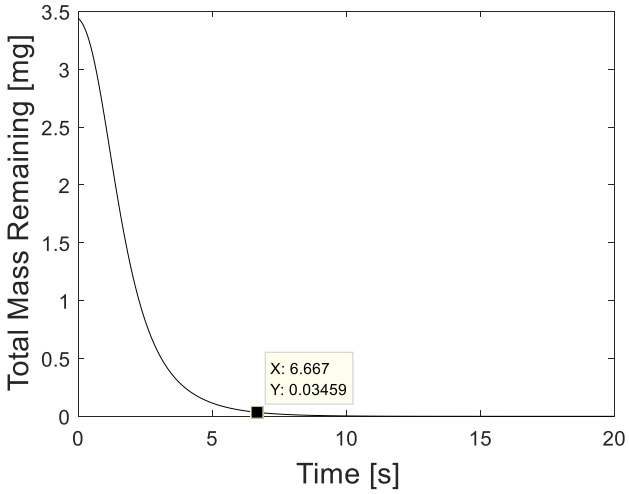

Figure 5.3: Evaporation curve from the model showing the exponential decay of film mass during evaporation as a function of time. Results are for system pressure of 0.8 bar, injector tip temperature of 80 °C, and 42 % film area

Following this procedure, the drying time was calculated for all operating conditions in Table 5.1 and the results of comparisons with experimental values are shown in Figure 5.4a and

Figure 5.4b for system pressure of 0.8 bar and 1.0 bar, respectively. The error bar in the experimental data represents the 95% confidence interval (two standard deviation) calculated from 30 repeated measurements for one data point, which is system pressure of 1.0 bar and tip temperature of 110 °C. The percentage error in this case was 6% and this percentage was extended to the other data points. The uncertainty in the model represents the variation in model output due to the variation in the surface area (i.e. 40 – 50 %) used in the calculations. In general, a good agreement between the experimental values and predictions are observed. The deviation between the experimental values and predictions above 110 °C can be owed to the fact that above 110 °C the evaporation mechanism is not only controlled by single-phase evaporation, and boiling regime had a dominant contribution, as observed by the authors, which is not included in the model. However, the trend-wise agreement between experiments and predictions, indicated by the change in slope, infers that single-phase evaporation could have a significant contribution during the boiling evaporation regime as well.

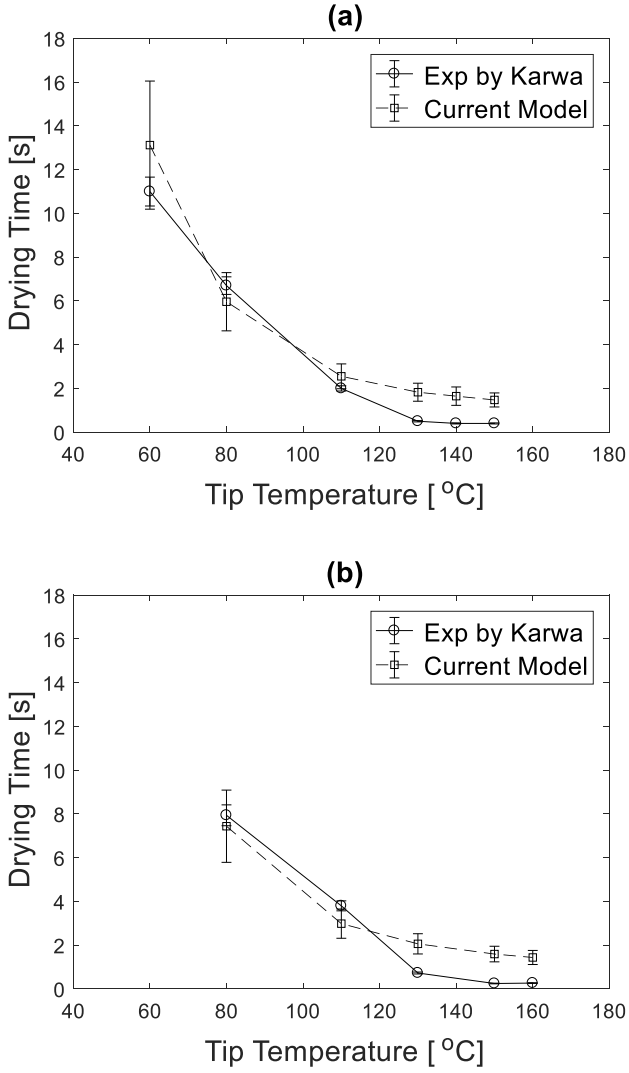

Figure 5.4: Comparison of evaporation times from experiments by Karwa et al versus the evaporation model at (a) 0.8 bar system pressure and (b) 1.0 bar system pressure for different injector tip temperatures. Good agreement is observed between experiments and predictions. Deviation above 110 °C is owed to the contribution of the boiling regime to evaporation, which is not included in the current model

5.2.2 Real Engine Conditions

Figure 5.5 shows the predicted evaporation curve for 10 bar BMEP and 2000 RPM operating point during an engine cycle. The change of film mass on the injector tip is shown as a function of crank angle degrees (CAD) from end of injection to spark. The pressure of vapor in liquid (predicted) as well as in gas (measured) are also plotted for the same evaporation period. It can be seen that mass is removed initially by evaporation until the vapor pressure in gas becomes

high enough to cause the molecules to diffuse from the gas to the liquid film, after which mass is added by condensation. This result agrees well with the expectation from Eq. 3.3, which describes the rate of film mass change as function of the vapor pressure difference in liquid and quiescent gas. This is shown in Figure 5.6, where the positive rate indicates evaporation whereas the negative rate indicates mass addition by condensation. All other operating points had evaporation curves similar to the one in Figure 5.5, and they are shown in Appendix D.

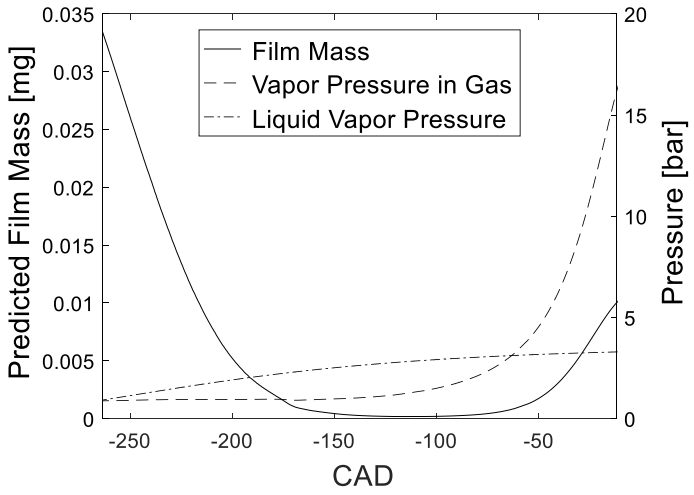

Figure 5.5: Evaporation curve showing film mass on injector tip (calculated from Eq. 3.11) as a function of time (shown as CAD) during an engine cycle. Pressures of vapor in liquid as well as in gas are also plotted. Results are for 10 bar BMEP and 2000 RPM

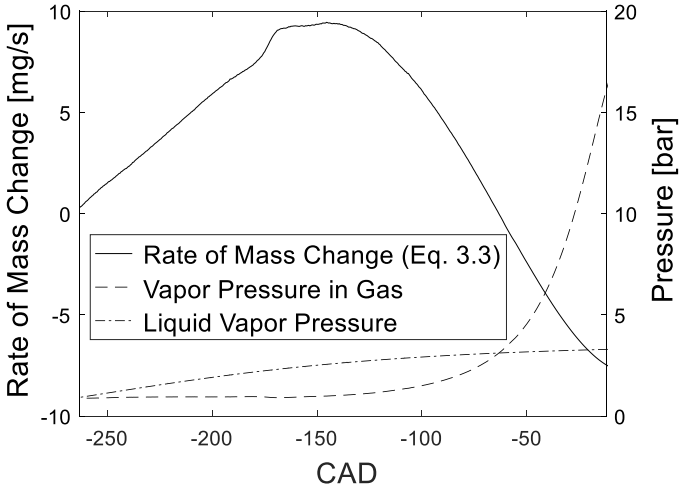

Figure 5.6: Rate of film mass change (calculated from Eq. 3.3) as a function of time (shown as CAD) during an engine cycle. Pressures of vapor in liquid as well as in gas are also plotted. Results are for 10 bar BMEP and 2000 RPM

The evaporation time constant was also calculated for all conditions and a sample plot is shown in Figure 5.7 for 10 bar BMEP and 2000 RPM (complete plots are shown in Appendix D). Since conditions are not stationary, the time constant is observed to change with time, in a similar manner as the predicted film mass. To define a representative time constant for each operating condition tested, the average time constant across the period from end of injection to spark was calculated.

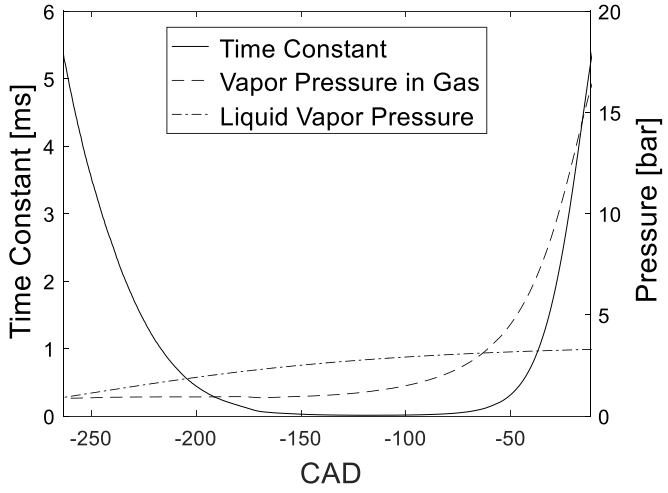

Figure 5.7: Calculated time constant of film on injector tip as a function of time (shown as CAD) during an engine cycle. Due to non-stationary conditions, time constant is observed to change with time from end of injection to spark time. Pressures of vapor in liquid as well as in gas are also plotted. Results are for 10 bar BMEP and 2000 RPM

Condensation of the vaporized fuel on the injector tip in the engine is, however, mostly unlikely to happen due to the influence of in-cylinder gas motion. The assumption is that any mass evaporated from the liquid film to the gas will be carried away by the gas flow. This assumption leads to the determination of the film mass remaining on the tip at time of spark as being the minimum predicted mass on the tip in the drying period i.e. from the end of injection to spark.

Based on this definition, trend-wise comparisons between the predicted film mass at time of spark and measured PN were performed for all operating conditions in the experimental test matrix (Table 4.3). Figure 5.8 shows a comparison of the line plots for the measured PN and predicted film mass as a function of injected fuel mass for the different speeds. Good trend-wise agreement is generally observed between the measured PN and predicted film mass at the time of spark. The predictive model was able to capture the non-linear behavior of increased PN emissions with engine load.

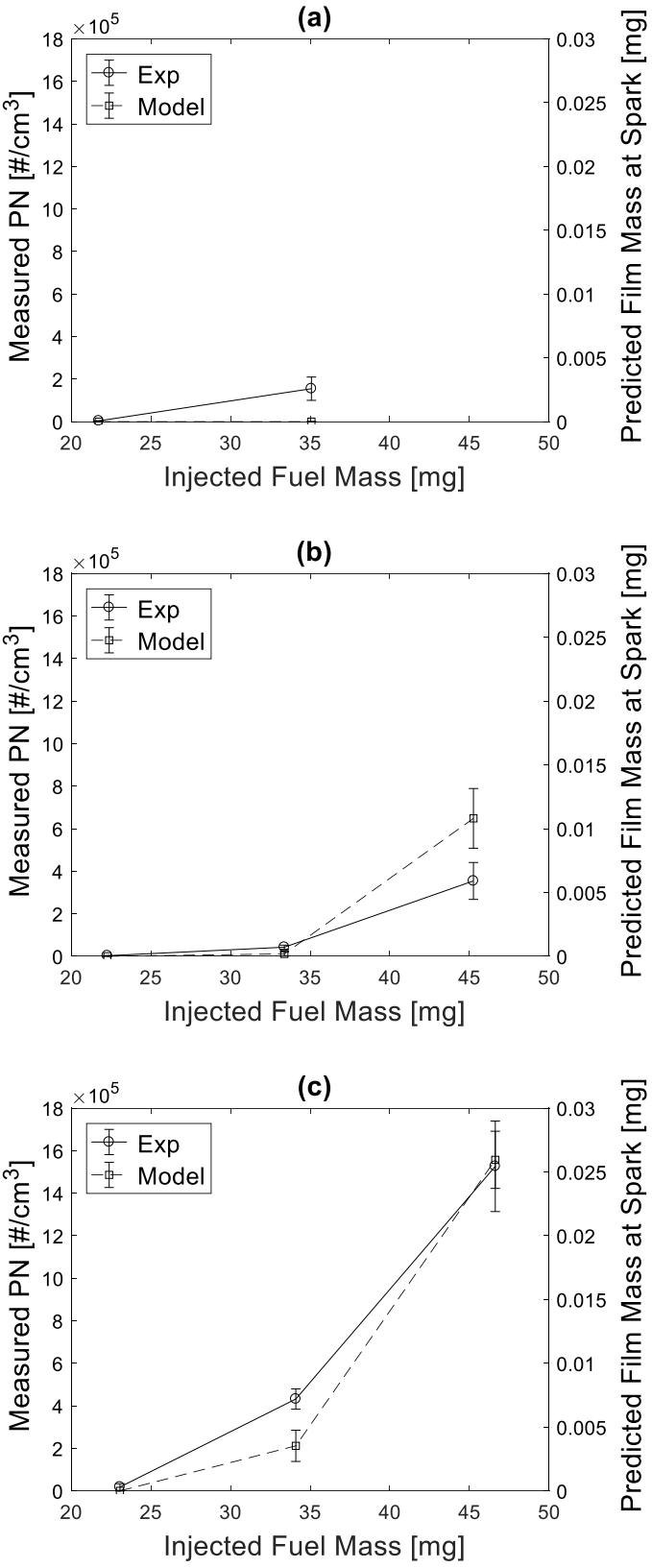

Figure 5.8: Line plots showing PN and predicted film mass at spark time as a function of injected fuel mass (i.e. engine load) for (a) 1000 RPM, (b) 2000 RPM and (c) 3000 RPM. Error bars for the model represents the variation in model output due to the uncertainty in the measured tip and fuel temperatures

A similar comparison between the average time constant and measured PN emissions was performed in Figure 5.9. The average time constant is observed to have good trend-wise agreement with experimental PN for all engine loads and speeds. This shows that the average time constant is a good measure of how much fuel film evaporates and affects PN in the tip wetting dominant region of a GDI engine.

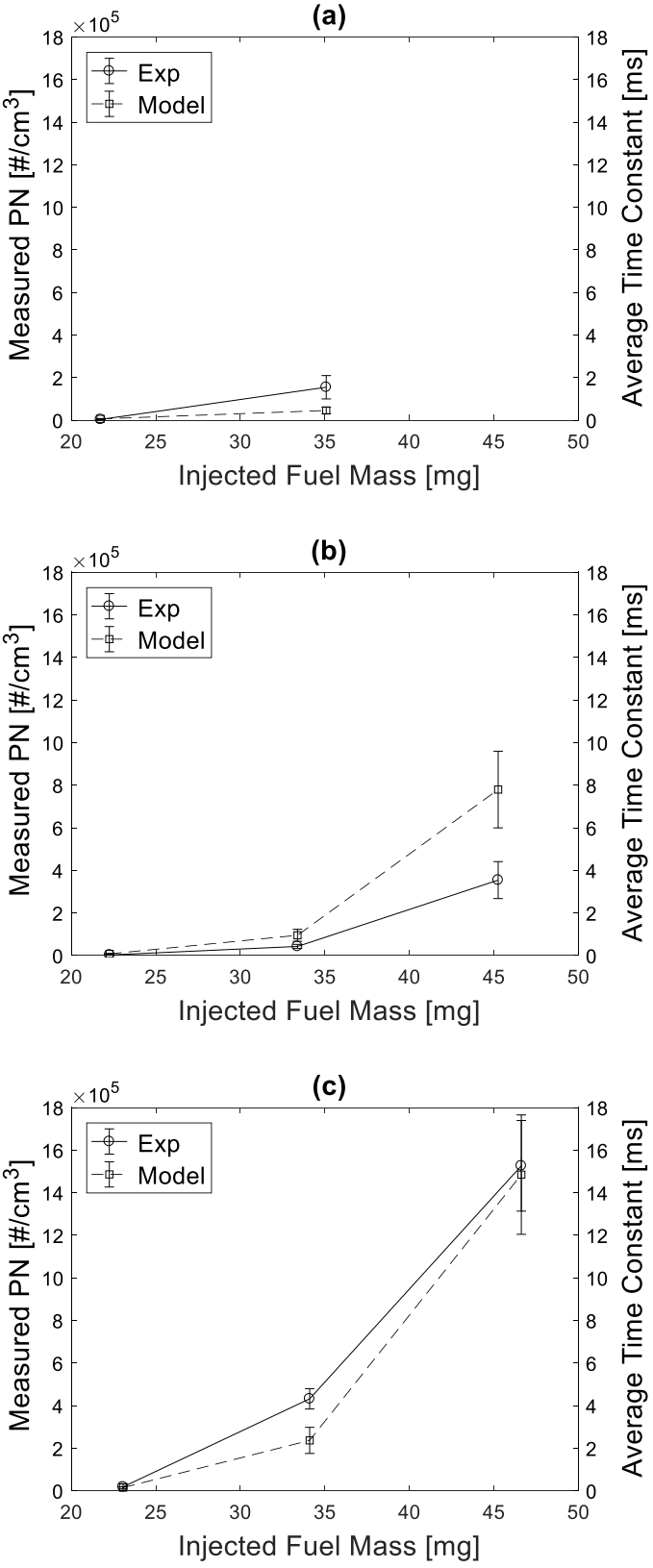

Figure 5.9: Line plots showing PN and calculated average time constant as a function of injected fuel mass (i.e. engine load) for (a) 1000 RPM, (b) 2000 RPM and (c) 3000 RPM. Error bars for the model represents the variation in model output due to the uncertainty in the measured tip and fuel temperatures

Quantitative correlations between predicted film mass and both measured PN and deposit volume were also calculated. Data from Figure 5.1c was used for the comparison. The correlation results are shown in Figure 5.10 for measured PN versus predicted film mass and in Figure 5.11 for measured deposit volume versus predicted film mass. Overall, the high R^2 value indicates good one-to-one correlation between predictions and experiments.

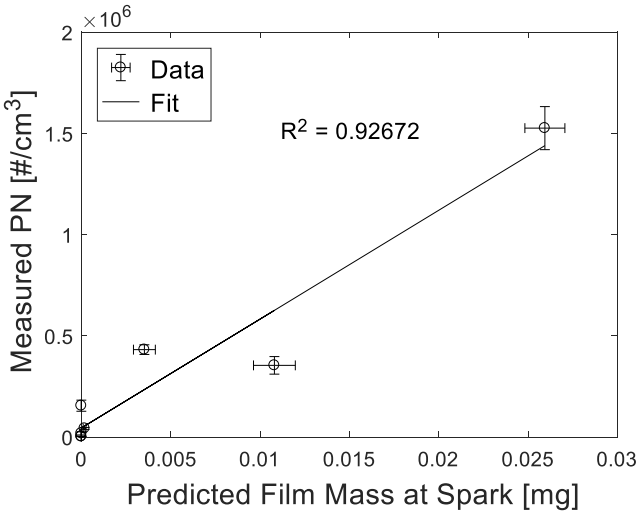

Figure 5.10: Quantitative correlation between measured PN and predicted film mass at spark time. Error bars for the model represents the variation in model output due to the uncertainty in the measured tip and fuel temperatures

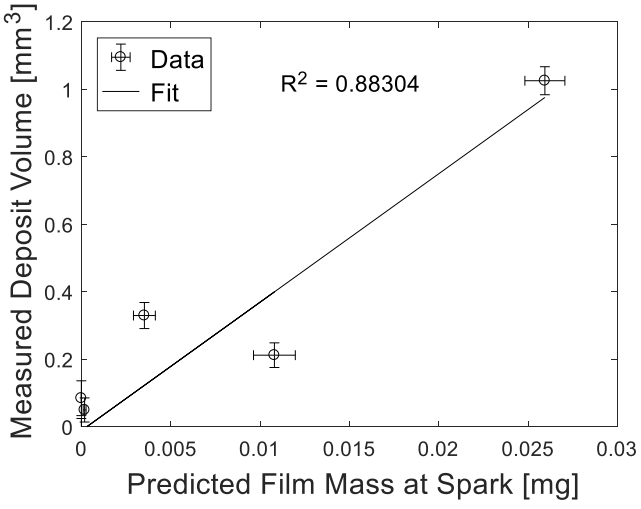

Figure 5.11: Quantitative correlation between measured deposit volume and predicted film mass at spark time. Error bars for the model represents the variation in model output due to the uncertainty in the measured tip and fuel temperatures

The correlation in Figure 5.10 could also be used to infer an estimate of the contribution of tip wetting to the total PN emissions. The equation fitted in Figure 5.10 has the form

$$PN[\#/\text{cm}^3] = 9 \times 10^7 m_{tip@spark}[\text{mg}] + 88791 \ldots (5.1)$$

At $m_{tip@spark} = 0$, $PN = 88791\ \#/\text{cm}^3$. This PN value represents the particulate emissions from all other sources of PN, which are assumed constant for all conditions tested. Now, if this PN value is subtracted from the total PN calculated using Eq. 5.1 for all other conditions, the PN due to tip wetting could be estimated. In other words

$$\text{Tip Wetting } PN\ [\#/\text{cm}^3] = \text{Total } PN\ [\#/\text{cm}^3] - 88791 \ldots (5.1)$$

The results of such analysis are shown in Table 5.3. The table shows that PN due to tip wetting contributed up to 95 % of the total PN emissions at high engine loads.

Table 5.3: Contribution of PN due to tip wetting to the total PN emissions for all conditions tested

Engine Speed	**BMEP**	**Predicted Film Mass at Spark**	**Total PN**	**Tip Wetting PN**	**Tip Wetting PN**
RPM	**bar**	**mg**	**#/cm^3**	**#/cm^3**	**%**
1000	6	2.38×10^{-16}	8.879×10^4	0.000	0.00
1000	10	2.83×10^{-09}	8.879×10^4	0.250	0.00
2000	6	1.48×10^{-13}	8.879×10^4	0.000	0.00
2000	10	7.09×10^{-06}	8.943×10^4	638.0	0.71
2000	14	0.003860	4.362×10^5	3.474×10^5	79.6
3000	6	7.18×10^{-10}	8.879×10^4	0.060	0.00
3000	10	0.000672	1.492×10^5	6.045×10^4	40.5
3000	14	0.016653	1.588×10^6	1.499×10^6	94.4

5.2.3 Sensitivity Analysis

In the calculation procedure presented in Chapter 3, the initial film mass and wetted surface area were assumed based on previous experimental observations in literature [11]. It is desired, however, to investigate how sensitive the results and correlations are to these assumptions. For that, a sensitivity analysis was performed by varying the initial film mass from 0.05% to 0.15% with increment of 0.025% of injected fuel mass at 10 bar BMEP. The wetted surface area was also varied from 2.0 to 3.0 mm^2 with 0.25 mm^2 increment. This is summarized in Table 5.4, with initial

film mass of 0.1% of injected fuel mass held constant when varying the wetted surface area and, a surface area of 2.5 mm^2 held constant when varying the initial film mass.

Table 5.4: Variations in assumed parameters used in the sensitivity analysis

Initial Film Mass [% of Injected Fuel Mass]	**Wetted Surface Area [mm^2]**
0.050	2.00
0.075	2.25
0.100	2.50
0.125	2.75
0.150	3.00

The R^2 value for all cases were calculated and the results are shown in Figure 5.12 for the effect of initial film mass variation and in Figure 5.13 for the effect of wetted surface area variation. It is understood that R^2 is usually used with much higher number of data points, but it is used in this case to give an estimate of the correlations. In general, high correlations (above 80%) can be noticed for all cases. R^2 was, however, less sensitive to the wetted surface area, compared to the initial film mass. The highest R^2 was found to be for the condition with initial film mass of 0.1% of injected fuel mass and wetted surface area of 3.0 mm^2.

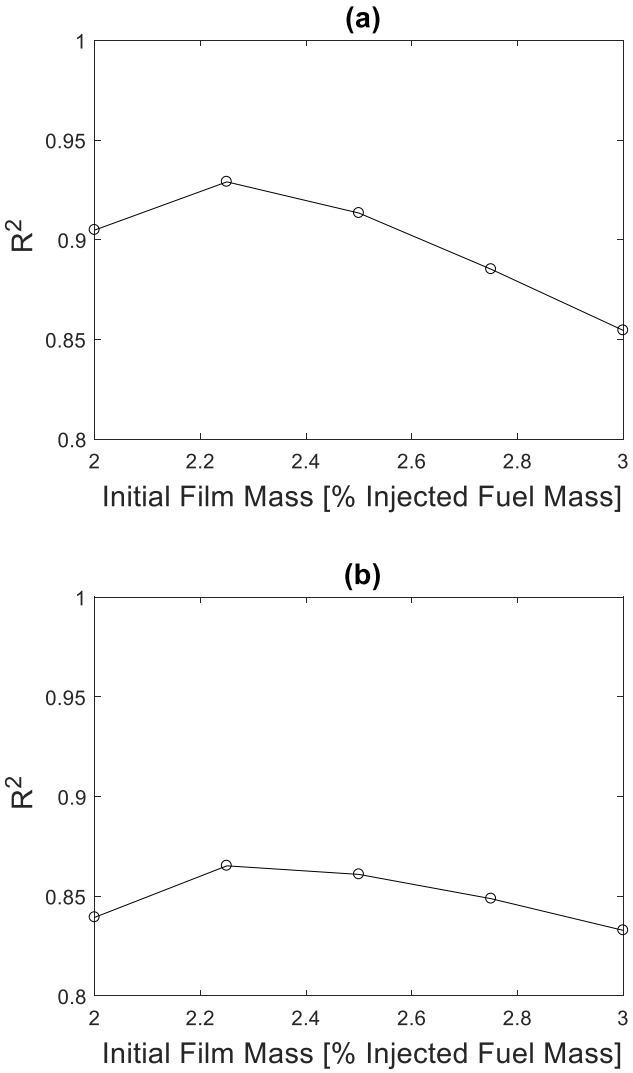

Figure 5.12: Sensitivity analysis results showing R^2 as a function of initial film mass. Results are for correlations between (a) measured PN and predicted film mass, and (b) measured deposit volume and predicted film mass. R^2 is observed to be sensitive to the initial film mass

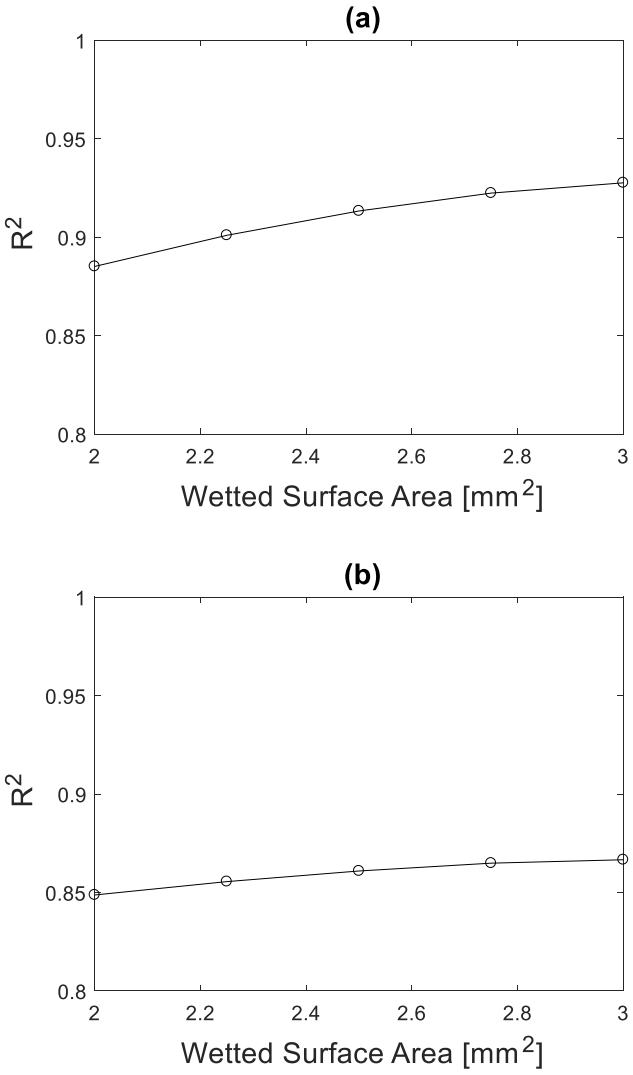

Figure 5.13: Sensitivity analysis results showing R^2 as a function of wetted surface area. Results are for correlations between (a) measured PN and predicted film mass, and (b) measured deposit volume and predicted film mass. R^2 is observed to be less sensitive to the wetted area than the initial film mass

5.3 Parametric Study

During the intake stroke, the variation in the calculated in-cylinder gas temperature between all conditions tested was found to have negligible effect on the results, meaning that if the average in-cylinder gas temperature for all conditions was used for the analysis of each operating point, the conclusions would be the same (see Appendix E). This gives us the opportunity to perform a wider parametric study to investigate the effect of the initial and boundary conditions on liquid film evaporation on injector tip using the average in-cylinder gas temperature.

Table 5.5 shows the parameters that were varied in this parametric study. Specifically, the varied parameters were: initial film mass ($m_{film,i}$, based on BMEP), wetted surface area (A), tip temperature (T_{tip}), initial film temperature ($T_{film,i}$), start of injection timing (SOI) and engine speed (N). When varying each parameter, all other parameters were fixed at the baseline condition, which is $m_{film,i}$ of 0.1% (of injected fuel mass at 10 bar BMEP), A of 2.5 mm^2, T_{tip} of 150 °C, $T_{film,i}$ of 90 °C, SOI of 290^o bTDC and engine speed of 2000 RPM. For each condition, the film mass on injector tip at the time of spark and the average time constant were calculated and were normalized by the baseline condition. In this way, an order of magnitude comparison could be performed.

Table 5.5: Initial and boundary conditions varied for the parametric study. The baseline conditions is $m_{film,i}$ = 0.1%, A = 3 mm^2, T_{tip} = 150 °C, $T_{film,i}$ = 90 °C, SOI = 290^o bTDC and 2000 RPM

$m_{film,i}$ [BMEP, bar]	A [mm^2]	T_{tip} [°C]	$T_{film,i}$ [°C]	SOI [^{o} bTDC]	N [RPM]
6	2.00	120	60	260	1000
8	2.25	135	70	270	1500
10	2.50	150	80	280	2000
12	2.75	165	90	290	2500
14	3.00	180	100	300	3000

The influence of each parameter is discussed in terms trend-wise effect on the predicted film mass at the time of spark and the order of magnitude change in predicted film mass caused by the systematic variation of the parameter within the range tested.

5.3.1 Effect of Initial Film Mass

The effect of initial film mass after end of injection on liquid fuel film evaporation on the injector tip is shown in Figure 5.14. It can be seen that with the linear increase in initial film mass, the remaining film mass on the injector tip increased in an exponential manner. This result in fact agrees well with current and previous experimental observations of exponential increase in PN emissions with injected fuel mass i.e. engine load [32]. A similar trend can be observed for the

average time constant. In general, varying the initial film mass resulted in more than an order of magnitude change in the predicted film mass at spark.

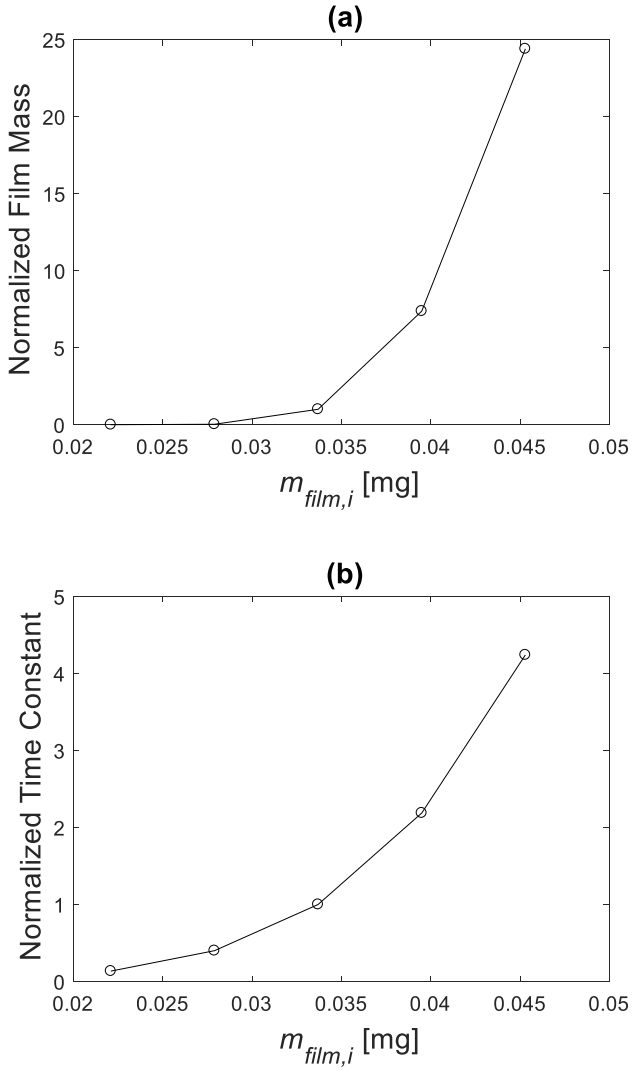

Figure 5.14: Effect of initial film mass after injection on (a) the predicted film mass at the time of spark and (b) the average time constant for the period: end of injection to spark. A = 3 mm^2, T_{tip} = 150 °C, $T_{film,i}$ = 90 °C, SOI = 290^o bTDC and N = 2000 RPM

5.3.2 Effect of Wetted Surface Area

The influence of the wetted surface area on the predicted film mass at the time of spark and the average time constant can be seen in Figure 5.15. Higher wetted area for the same initial film mass allowed more heat transfer from the tip to the liquid film, which increased the evaporation and reduced the film mass on the tip at the time of spark in an exponential manner. The variation

in the wetted surface area in Figure 5.15 led to an order of magnitude reduction in the predicted film mass remaining on the injector tip.

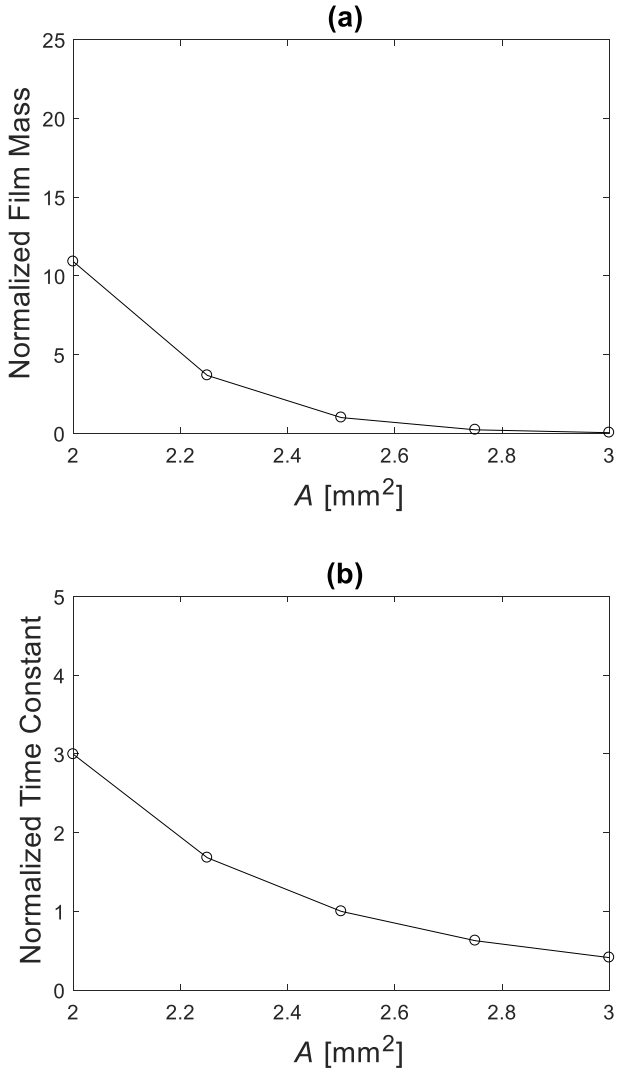

Figure 5.15: Effect of wetted surface area on (a) the predicted film mass at the time of spark and (b) the average time constant for the period: end of injection to spark. $m_{film,i}$ = 0.1% of injected fuel mass at 10 bar BMEP, T_{tip} = 150 °C, $T_{film,i}$ = 90 °C, SOI = 290° bTDC and N = 2000 RPM

5.3.3 Effect of Tip Temperature

The tip temperature also showed an order of magnitude reduction in the predicted film mass at the time of spark in a similar trend as the wetted surface area as can be seen in Figure 5.16. The tip temperature had a direct influence on the liquid vapor pressure, which directly influenced film evaporation.

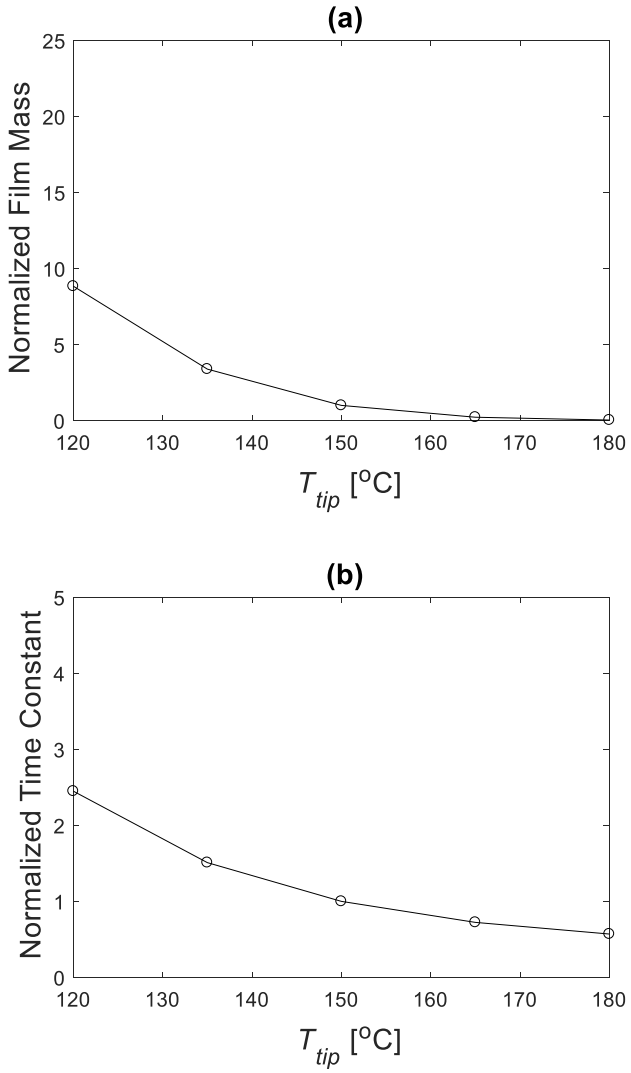

Figure 5.16: Effect of injector tip temperature on (a) the predicted film mass at the time of spark and (b) the average time constant for the period: end of injection to spark. $m_{film,i}$ = 0.1% of injected fuel mass at 10 bar BMEP, A = 3 mm^2, $T_{film,i}$ = 90 °C, SOI = 290^o bTDC and N = 2000 RPM

5.3.4 Effect of Initial Film Temperature

As shown in Figure 5.17, the initial film temperature had a smaller effect on the predicted film mass at the time of spark compared to the aforementioned parameters. The average time constant was also affected similarly by the initial film temperature.

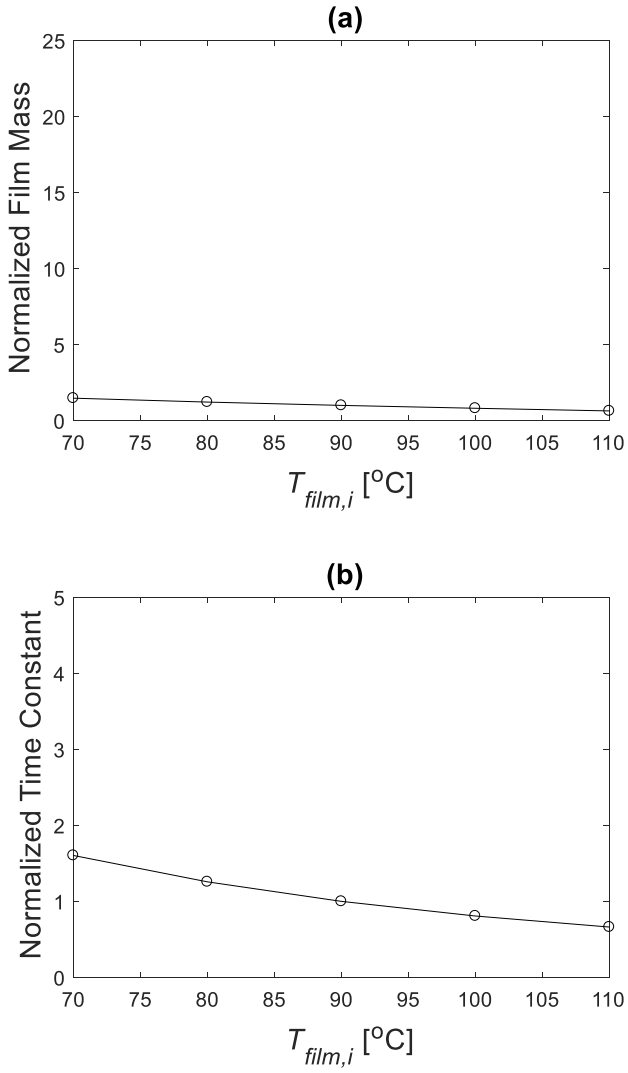

Figure 5.17: Effect of initial film temperature on (a) the predicted film mass at the time of spark and (b) the average time constant for the period: end of injection to spark. $m_{film,i}$ = 0.1% of injected fuel mass at 10 bar BMEP, A = 3 mm^2, T_{tip} = 150 °C, SOI = 290^o bTDC and N = 2000 RPM

5.3.5 Effect of Drying Time

The available time for tip drying, affected by engine speed and start of injection timing, showed a reduction influence on the predicted film mass at the time of spark and the average time constant as seen in Figure 5.18. As the absolute drying time increased, the predicted film mass at time of spark and the average time constant decayed exponentially. This exact trend was observed in previous work [32], which showed the decay in measured PN as a function of drying time (for different engine speeds and start of injection timings). In the range considered in Figure 5.18, the drying timescale resulted in an order of magnitude change in the predicted film mass at spark.

The closely matched trends between model predictions and current as well as previous experimental measurements of PN emissions show high potential to use the model to develop operations and technologies for PN emissions reductions.

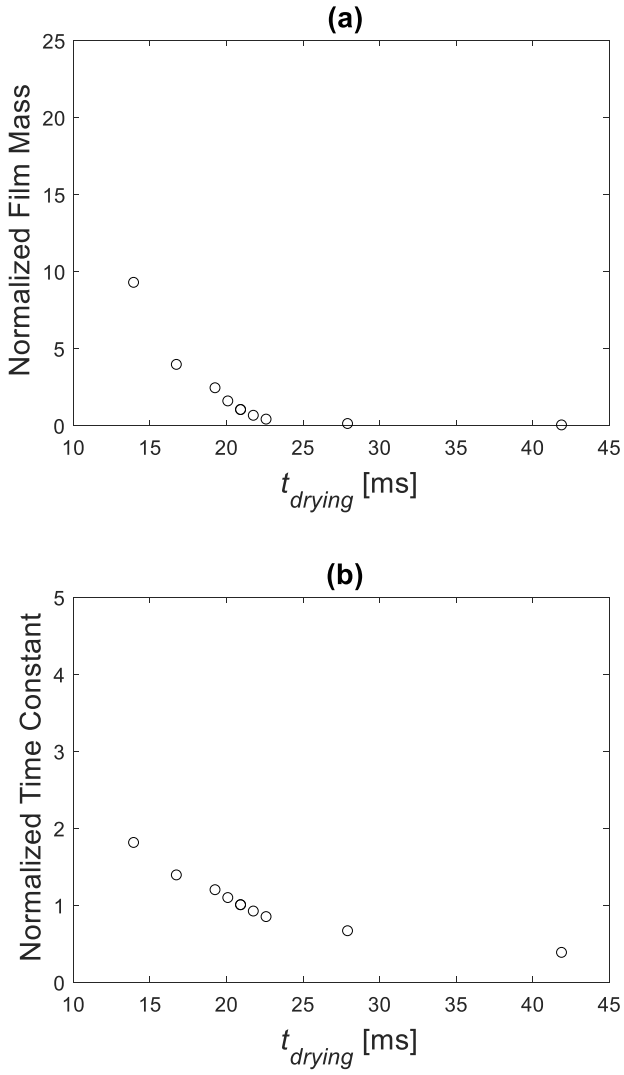

Figure 5.18: Effect of drying time (affected by engine speed and SOI) on (a) the predicted film mass at the time of spark and (b) the average time constant for the period: end of injection to spark. $m_{film,i}$ = 0.1% of injected fuel mass at 10 bar BMEP, A = 3 mm^2, T_{tip} = 150 °C, and $T_{film,i}$ = 90 °C. Lower engine speeds and early injections lead to longer drying times

5.4 Relating Engine Operation and Calibration Parameters to the Evaporation Time Constant for Reduced PN Emission

Figure 5.9 showed that the time constant, described by Eq. 3.21, captured the physical trend in PN emissions in a similar manner to the predicted film mass at the time of spark (Figure 5.8). The study in Section 5.3 highlighted the effect of the different initial and boundary conditions on the average time constant. Understanding the variability in the average time constant was important because it will be reflected on the variation of PN emissions due to tip wetting. The next

step would be to relate the changes in initial and boundary conditions to changes in engine operation and calibration parameters.

The evaporation time constant equation (Eq. 3.21 or 3.22) shows that the time constant reduces with *reduced* film thickness, ambient gas pressure, net molecular weight, and initial film mass. On the other hand, the time constant reduces with *increased* wetted surface area, diffusion coefficient, gas temperature, and liquid vapor pressure of the film. The effect of some of these parameters were investigated in the parametric study in Section 5.3.

An attempt is made here to relate the previous parameters to changes in engine hardware and calibration and suggest methods to reduce tip wetting PN. The film thickness could be reduced and wetted surface area could be increased by means of material selection and surface finish of the injector tip. Smooth surfaces have the potential to result in higher wetting areas and smaller film thicknesses, which both result in better evaporation and lower PN.

The initial film mass after injection on the other hand depends to a high extent on the injector design, operating conditions and fuel flow conditions. Large reductions in tip wetting had been achieved in the past through changes in injector pre-hole and valve seat designs, which influenced how the fuel flows through the injector nozzle, onto the pre-hole and eventually depositing on the external surface of the injector tip. However, these reductions are not going to be enough in the near future and better understanding is needed on how the other injector design parameters, e.g. the ratio of nozzle hole length to hole diameter, affect the initial film mass on the injector tip.

The diffusion coefficient is a function of gas temperature and pressure, and fuel vapor properties. Based on the diffusion coefficient equation (Eq. 3.12), the diffusivity increases with gas temperature, and in contrast, decreases with gas pressure. In an engine cycle, both gas temperature and pressure increase from end of injection to spark. Nonetheless, the influence of

increasing the gas pressure outweighs the influence of increasing the gas temperature, resulting eventually in reduced diffusivity during the compression stroke. This can be seen in Figure 5.19 for the case of 10 bar BMEP and 2000 RPM. Therefore, lower intake pressures would seem appropriate to achieve better diffusivity and evaporation. However, this is impractical, and higher or boosted intake pressures are normally desirable to achieve better thermal efficiency. This imposes a practical limitation on this parameter as a potential degree of freedom. In terms of fuel properties, the selection of the fuel has also a direct impact on the diffusivity coefficient. It is generally desired to use a fuel with better mass diffusivity characteristics.

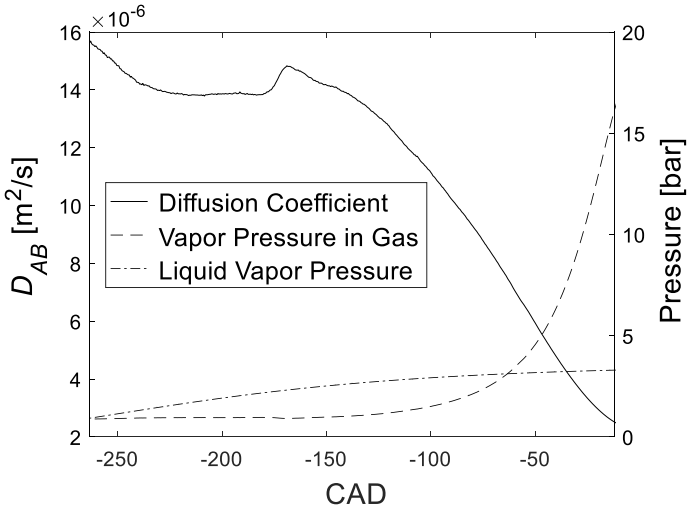

Figure 5.19: Calculated diffusion coefficient as a function of time (shown as CAD aTDC) during an engine cycle. Pressures of vapor in liquid as well as in gas are also plotted. Results for 10 bar BMEP and 2000 RPM

Increasing liquid vapor pressure by means of increasing tip temperature, results in better evaporation and reduced time constant. Increasing the tip temperature could be achieved through protruding the injector tip into the combustion chamber. An external heater could also be used to heat up the injector body, which results in increasing the tip temperature. Lower net molecular weight on the other hand results in reduced time constant as shown by Eq. 3.22. However, this property is not independent from all other fuel properties that affect the evaporation. For example, ethanol has lower molecular weight (46.07 g/mol) compared to EPA Tier III premium certification

gasoline (114.22 g/mol). Thus, ethanol would seem to be a better choice for increased evaporation than EPA Tier III premium certification gasoline. However, ethanol has much lower liquid vapor pressure than gasoline (5.95 kPa versus 62.5 kPa at standard temperature and pressure) [68], which makes ethanol more difficult to evaporate than gasoline. The combined effect of all fuel properties in Eq. 3.22 should be investigated to better understand how the choice of fuels influence film evaporation on injector tip.

5.5 Effect of Injector Tip Deposit on PN Emission

It is desired to explore the behavior of increased tip wetting PN with injector tip deposit. For that, stabilized PN at the end of the warmup procedure at 4 bar BMEP and 1000 RPM was recorded and plotted against the corresponding deposit level at which PN was stabilized. The different deposit levels were formed as a result of the coking procedure at different coking times and conditions. The results of such graph are shown in Figure 5.20. It is generally observed that deposit level amplified the tip wetting behavior, despite the fact that the same amount of fuel mass was injected in each case.

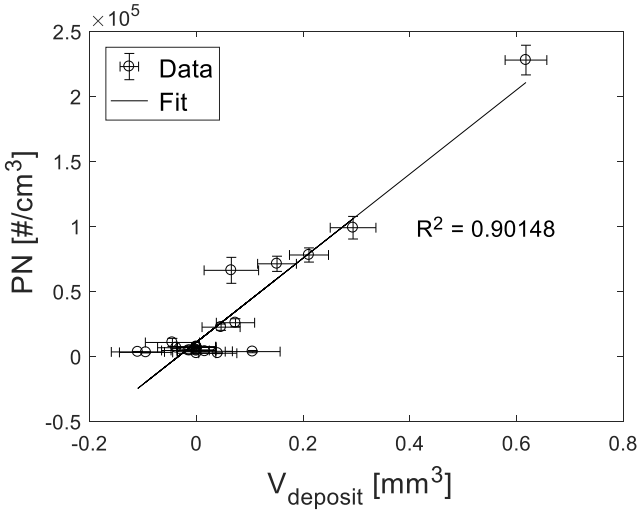

Figure 5.20: Measured stabilized PN at the end of the warmup procedure as a function of deposit level at 4 bar BMEP and 1000 RPM operating point

There could be a number of reasons for the tip wetting amplification behavior. First, the deposit might have a rougher surface than the original clean tip surface. The increased roughness might lead in decreased wetted surface area and increased film thickness. In addition, the tip deposit might act as a sponge, absorbing more fuel during injection, and resulting in increased initial film mass after EOI. The macroscopic morphology of these sponge-like deposits can be observed in Figure 5.21 for 10 bar BMEP operating load. It can be seen that as the drying timescale reduced (by increasing engine speed) and the coking time increased, deposit level increased. Tip deposits could also reduce the evaporation rate of the fuel film due to the insulating and porous nature of carbon deposits.

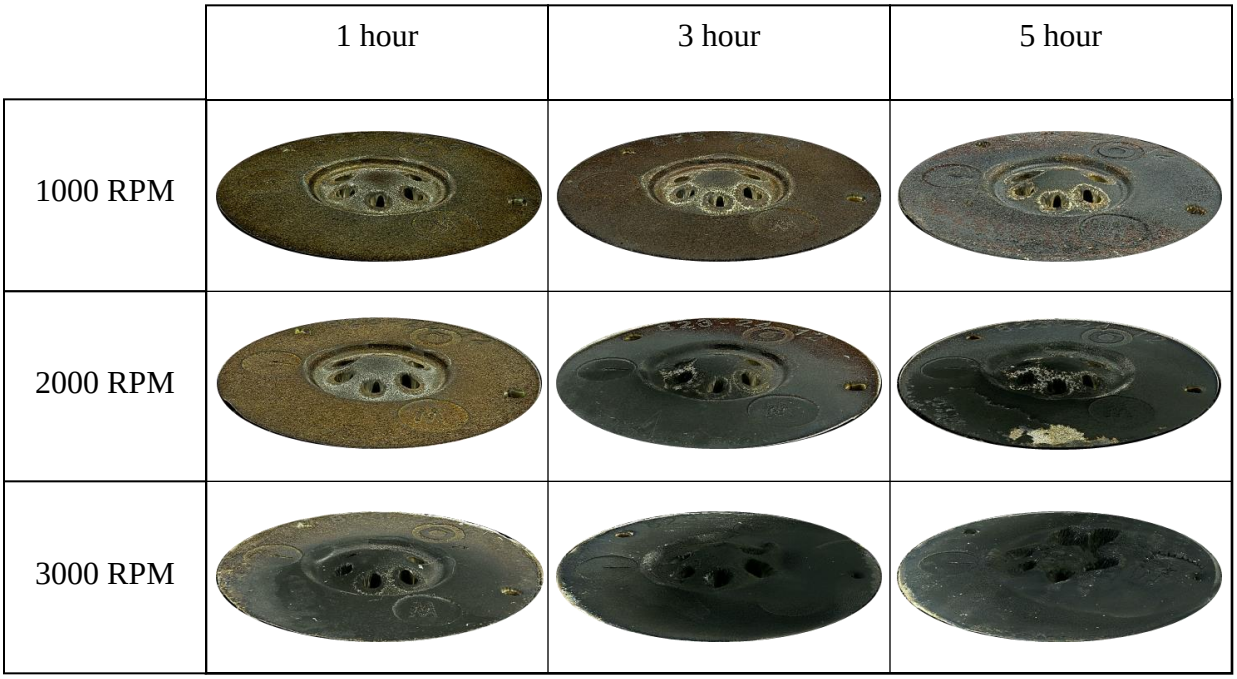

Figure 5.21: Macroscopic morphology of injector tip deposit at different engine speeds and steady state coking times at 10 bar BMEP. Images are for injector installed in cylinder 1 (cylinder farthest from the flywheel)

Chapter 6 Conclusions and Future Outlook

6.1 Summary

The reported particulate number levels for vehicles equipped with gasoline direct-injection engines in many studies between 2009 and 2017 were within 6×10^{11} and 2×10^{13} particles/km [29,69,70]. Current particulate number standards in Europe limits the PN to 6×10^{11} particles/km [7], and the same limit must be met by 2020 in China [8]. Identifying and mitigating the sources of PN emissions for gasoline direct-injection engines is therefore critical to meet the challenging future emissions targets. Among the different sources, injector tip wetting has been identified as a significant source of particulate number emissions in regions where tip wetting is the dominant PN formation mechanism. In the tip wetting dominant regions studied in this work (where other sources of PN were less significant and kept constant), tip wetting contributed up to 95 % of the total PN emissions. Thus, eliminating tip wetting as a source of particulates would contribute significantly to meeting future limits.

This dissertation developed an analytical model for liquid film evaporation on the fuel injector tip for the mitigation of injector tip wetting as a source of particulates in GDI engines. The physical model explains theoretically how fuel films on the injector tip evaporate with time from end of injection to spark. The model takes into consideration engine operating conditions, such as engine speed, engine load, tip temperature, fuel temperature, gas temperature and pressure, and fuel properties. The model was able to explain for the first time the observed trends in particulate emissions due to injector tip wetting. Engine experiments were leveraged to validate the theoretical model by correlating the predicted film mass at the time of spark to PN emissions and tip deposit

volume measurements at different operating conditions. A novel technique for measuring the volume of deposit on injector tip based on 3D digital microscopy was developed for this purpose. In addition, an evaporation time constant was defined and was also found to correlate well with the measured PN.

6.2 Conclusions

The key findings of this research are listed below.

- The liquid film evaporation on the injector tip follows a first order, asymptotic behavior. This exponential nature of the tip drying has a direct impact on the amount of film mass remaining on the injector tip at the time of spark. PN emissions have always been observed to increase in an exponential manner with injected fuel mass, i.e. engine load. It was originally hypothesized that the initial film mass after end of injection increased exponentially with engine load, hence the exponential increase in PN. However, the model results showed that as the initial film mass after end of injection increased linearly with injected fuel mass, the film mass at the time of spark increased in an exponential manner. Similarly, the observed exponential decay in PN with drying timescale for different engine speeds and start of injection timings was also explained by the model, where the predicted film mass at the time of spark decayed exponentially with the absolute drying time. Consequently, it is concluded that injector tip wetting increases linearly with injected fuel mass.
- Most of the injector's initial and boundary conditions studied had a significant effect (more than an order of magnitude change) on liquid film evaporation on the injector tip in the range of conditions studied. These parameters include the initial film mass, the surface area of the wetted film, the injector tip temperature and the available time for tip drying. The initial film temperature had the least effect on film mass evaporation.

- An evaporation time constant equation was defined, which can be minimized for better evaporation and lower PN emissions. The minimization of this time constant, as shown by its equation, could be achieved by *reducing* the film thickness, the gas pressure, the net molecular weight of fuel and air and the initial film mass after end of injection. The time constant can also be reduced by *increasing* the wetted surface area, the diffusion coefficient, the gas temperature, and the liquid vapor pressure of the film. Injector manufacturers can use this information to maximize liquid film evaporation by correlating these variables to changes in hardware and calibration.

6.3 Future Outlook

In addition to understanding of the film evaporation process from end of injection to the spark time, complete elimination of injector tip wetting as a source of particulate emissions requires also understanding of the liquid film formation process during injection. The development of a theoretical model for liquid film formation from start to end of injection, which is a function of injector design, operating conditions and fuel flow conditions, would help achieve that goal.

The model developed in this study showed, through correlating the predicted film mass to measurements of PN emissions, injector tip drying is an essential process, which can utilized to mitigate particulate emissions due to injector tip wetting. The model could be extended to study other fuel impingement mechanisms and liquid film geometries in internal combustion engines, such as liquid films on piston crown and/or liner walls. This would significantly improve the understanding of the evaporation processes for better management and mitigation of these liquid films, which are the major contributors to particulate emissions under certain operating conditions.

The current theoretical model had a limitation where the effect of in-cylinder gas motion was not included in the evaporation equation. In-cylinder gas flow will result in non-equilibrium conditions at the liquid-gas interface, changing conditions of the partial pressure of the vapor in

the gas affecting evaporation. This effect was compensated for in the current model by assuming no condensation and using the minimum predicted mass as the film mass at time of spark. The model, however, could be improved by including the influence of in-cylinder gas motion in the evaporation equation. This would improve the understanding of the in-cylinder gas motion effects on evaporation, especially at high engine speeds.

The effects of some initial and boundary conditions have been highlighted in this study, and the wetted surface area was shown to be the most influential parameter affecting liquid film evaporation on injector tip. Understanding of the effect of tip surface properties, such as surface roughness and surface material, on the wettability behavior of fuel films would be crucial to maximizing the wetted area and reducing particulate emissions due to tip wetting. In a similar manner, raising injector tip temperature was found to be important in reducing particulate emissions. Finding ways to heat up injector body and raise the injector tip temperature would be very beneficial in mitigating particulates due to tip wetting.

Injector deposit was shown to cause amplification of injector tip wetting, increasing the total particulate emissions, i.e. PN drift. The mitigation of the amplification behavior could be achieved by either understanding the physical mechanisms at which injector tip deposit causes PN drift or by understanding and minimizing the growth of the deposit layer on the injector tip. Fundamental experiments of liquid droplets on injector tip surfaces with and without carbon deposit could be performed to understand the wettability behavior and sponge-like effect of injector deposit. The mitigation of the deposit growth on the other hand could be achieved by modeling the carbon deposit formation process as a fouling problem, which will enable better understanding of the effect of different design and operating conditions on deposit growth.

Appendices

Appendix A Fuel and Gas Properties

A.1 Lennard-Jones Potentials

Table A.1 lists the characteristic Lennard-Jones lengths and energies for a number of pure substances [71].

Table A.1: Lennard-Jones potentials determined from viscosity data [71]

Symbol	**Substance**	σ **[Å]**	ε/k **[K]**
Air	Air	3.711	78.6
CH_4	Methane	3.758	148.6
CO	Carbon monoxide	3.69	91.7
CO_2	Carbon dioxide	3.941	195.2
C_2H_2	Acetylene	4.033	231.8
C_2H_4	Ethylene	4.163	224.7
C_2H_6	Ethane	4.443	215.7
C_2H_5OH	Ethanol	4.53	362.6
C_3H_8	Propane	5.118	237.1
n-C_4H_{10}	*n*-Butane	4.687	531.4
n-C_5H_{12}	*n*-Pentane	5.784	341.1
H_2	Hydrogen	2.827	59.7
N_2	Nitrogen	69.143.798	71.4
O_2	Oxygen	3.467	106.7

A.2 Thermal Properties of Isooctane

The thermal properties of isooctane used in the analysis are summarized in Table A.2. In general, the properties were taken from NIST, unless the source is mentioned otherwise.

Table A.2: Thermal properties of isooctane used in the analysis. Properties are taken at 90 °C and atmospheric pressure. Source: NIST, unless otherwise mentioned

Property	**Symbol**	**Unit**	**Magnitude**
Molecular Weight	$\bar{M}$	g/mol	114.23
Heat of Vaporization	ΔH_{vap}	kJ/mol	31.675
Density	ρ	Kg/m^3	679.10
Thermal Conductivity (Liquid) [72]	k	W/m-K	0.0803
Specific Heat (Liquid) [73]	c_p	J/kg-K	2331.9
Critical Temperature	T_c	K	543.90
Critical Molar Volume	v_c	cm^3/g-mol	468.00
Critical Pressure	p_c	bar	25.700
First Antoine Constant	A	-	3.93679
Second Antoine Constant	B	-	1257.84
Third Antoine Constant	C	-	-52.4150

Appendix B MATLAB Code

A MATLAB script has been written (in MATLAB R2016b on Microsoft Windows 10 Enterprise) to implement the solution algorithm discussed in Chapter 3.

```
% This script describes how fuel film on injector tip evaporates with time
% in an engine cycle. In-cylinder gas temperature (approximated from
% in-cylinder gas pressure) is required for calculations.

%% Import Data
clc
clear

% Import in-cylinder pressure and temperature data
CAD = xlsread('Pressure and Temperature Data.xlsx','Pressure','A1:A10000');
%Crank angle recorded experimentally [CAD]
CAD_T = xlsread('Pressure and Temperature Data.xlsx','CAD-
Temperature','A1:H10000'); %Crank angle from gas temperature calculation
[CAD]
p = xlsread('Pressure and Temperature
Data.xlsx','Pressure','B1:I10000')*100000; %Measured in-cylinder gas pressure
(average of 300 cycles) [Pa]
T_g = xlsread('Pressure and Temperature
Data.xlsx','Temperature','A1:H10000'); %In-cylinder gas temperature
calculated from BeCAT [K]

% Interpolate in-cylinder gas temperature to match the size of pressure
nanx = isnan(T_g);
T = zeros(size(p,1),size(p,2));
for i = 1:size(p,2)
    x = CAD_T(:,i);
    y = T_g(:,i);
    T(:,i) = interp1(x(~nanx(:,i)),y(~nanx(:,i)),CAD,'spline','extrap');
end

% Import measured PN and deposit volume data
PN = xlsread('PN and Deposit Volume Data.xlsx','Sheet1','P3:P10000');
%Particle number [#/cm^3]
PN_err = xlsread('PN and Deposit Volume Data.xlsx','Sheet1','Q3:Q10000');
%Particle number error [deg]
V_dep = xlsread('PN and Deposit Volume Data.xlsx','Sheet1','N3:N10000');
%Deposit volume [mm^3]
V_dep_err = xlsread('PN and Deposit Volume Data.xlsx','Sheet1','O3:O10000');
%Deposit volume error [deg]

% Import operating conditions
```

```
RPM = xlsread('Boundary Conditions.xlsx','Sheet1','A3:A10000')'; %Engine
speed [RPM]
BMEP = xlsread('Boundary Conditions.xlsx','Sheet1','B3:B10000')'; %Engine
load [bar]
IFM = xlsread('Boundary Conditions.xlsx','Sheet1','C3:C10000')'; %Injected
fuel mass [mg]
Tw = xlsread('Boundary Conditions.xlsx','Sheet1','D3:D10000')'+273.15; %Tip
temperature [K]
Ti = xlsread('Boundary Conditions.xlsx','Sheet1','E3:E10000')'+273.15';
%Initial film temperature [K]
EOI = xlsread('Boundary Conditions.xlsx','Sheet1','F3:F10000')'; %End of
injection timing [CAD bTDC]
SPA = xlsread('Boundary Conditions.xlsx','Sheet1','G3:G10000')'; %Spark
timing [CAD bTDC]

%% Fuel and Air Properties
T90 = 162.5+273.15; %90 percent distillation temperature of Tier 3 at
standard pressure [K]
HOV = 31675; %Heat of vaporization of Tier 3 (isooctane) for 100+ degC
[J/mol]
p0 = 101325; %Standard pressure [Pa]
R = 8.314; %Ideal gas constant [J/mol-K]
k = 0.0803; %Thermal conductivity of isooctane [W/m-K]
rho = 679.1; %Density of Tier 3 at 90C [kg/m3]
cp = 2331.9; %Specific heat of isooctane [J/kg-K]
mw_a = 18.01528E-3; %Average molecular weight of air [kg/mol]
mw_f = 0.11422; %Average molecular weight of Tier 3 [kg/mol]
T_c = 543.9; %Critical temperature of isooctane [K]
v_c = 468; %Critical molar volume of isooctane [cm^3/g-mol]
p_c = 25.7; %Critical pressure of isooctane [bar]

% Calculation of the boiling point of liquid film
BP = (T90./(1-((R*T90/HOV).*log(p./p0)))); %Fuel boiling temperature as a
function of in-cylinder pressure based on T90 [K]
Delta_T = Tw - BP; %Tip superheat [K]

% Diffusion coefficient parameters
z_c = p_c*100000*v_c/1000000/R/T_c; %Compressibility factor of isooctane
sigma_f = 0.1866*v_c^(1/3)*z_c^(-6/5); %Collision diameter (Lennard-Jones
length) of isooctane [Å]
sigma_a = 3.711; %Collision diameter of air [Å]
sigma = (sigma_a+sigma_f)/2; %Net Lennard-Jones length
epsilon_a = 78.6; %Energy of interaction (Lennard-Jones energy) of air
(epsilon/k_B)
epsilon_f = 0.424*T_c*v_c/sigma_f^3; %Energy of interaction of isooctane
(epsilon/k_B)
epsilon = sqrt(epsilon_a*epsilon_f); %Net Lennard-Jones energy
mw_t = 2*(1/(mw_f*1000)+1/(mw_a*1000))^(-1); %Net molecular weight (M_AB)
p_bar = p/100000; %Ambient (in-cylinder) pressure in bar, which is the unit
used in the diffusion equation

%% Quasi-Steady Assumption Solution Method

% Defining initial film mass and wetted surface area
Mf = IFM*0.1/100*1E-6; %Initial film mass on tip after EOI [kg] (% of
injected fuel mass)
```

```
slope = (Mf(5)-Mf(3))/(BMEP(5)-BMEP(3)); %Slope of the linear curve of
initial film mass vs. load
A_6bar = 2E-6; %Assumed surface area of evaporation for 6 bar [m^2]. For 10
and 14 bar, A is automatically calculated based on "slope"
y_int = A_6bar-slope*BMEP(1); %Y-intercept for the linear curve for A vs.
load
A = slope*BMEP+y_int; %Surface area of evaporation [m^2](assuming a
cylindrical liquid film)
Vl0 = Mf/rho; %Initial film volume [m^3]
L0 = Vl0./A; %Initial film thickness [m]

% Changing engine time from CAD to seconds (t = 0 @ EOI)
n = length(CAD);
n0 = length(RPM);
t = zeros(n,n0);
dt = zeros(n0,1);
for i = 1:n0
    t(:,i) = (CAD-EOI(i))/6/RPM(i); %Engine time [s]
    dt(i,1) = t(n,i) - t(n-1,i);
end

% Solving eqs. for the complete time domain
Tl = zeros(n,n0);
pv = zeros(n,n0);
V = zeros(n,n0);
T_star = zeros(n,n0);
omega = zeros(n,n0);
D = zeros(n,n0);
M = zeros(n,n0);
Vl = zeros(n,n0);
L = zeros(n,n0);
tau_c = zeros(n,n0);
M_l = zeros(n,n0);
L_l = zeros(n,n0);
for j = 1:n0
    for i = 1:n
        Tl(i,j) = Tw(j)+(Ti(j)-Tw(j))*exp(-k*t(i,j)/(rho*(L0(j)-
L(i,j))^2*cp)); %Liquid temperature [K]
        pv(i,j) = 10^(3.93679-(1257.84/(Tl(i,j)-52.415)))*100000; %Liquid
vapor pressure of isooctane calculated from Antoine Eq. for temps > 25C [Pa]
        V(i,j) = R*T(i,j)*Mf(j)/(pv(i,j)*mw_f); %Vapor volume [m^3]
        T_star(i,j) = T(i,j)/epsilon;
        omega(i,j) =
real(1.06036/(T_star(i,j)^(0.1561))+0.193/exp(0.47635*T_star(i,j))+1.03587/ex
p(1.52996*T_star(i,j))+1.76474/exp(3.89411*T_star(i,j))); %Collision integral
        D(i,j) =
real(0.00266*T(i,j)^(3/2)/(p_bar(i,j)*mw_t^(1/2)*sigma^2*omega(i,j))/10000);
%Diffusion coefficient [m^2/s]
        M(i,j) = Mf(j)*(1-exp(-A(j)/(L0(j)-L(i,j))*D(i,j)/V(i,j)*t(i,j)));
%Evaporated mass
        Vl(i,j) = M(i,j)/rho; %Lquid film volume removed by evaporation [m^3]
        L(i,j) = Vl(i,j)/A(j); %Liquid film thickness removed by evaporation
[m]
        tau_c(i,j) = Mf(j)*(L0(j)-
L(i,j))/(A(j)*D(i,j))*R*T(i,j)/(mw_f*pv(i,j)); %Evaporation time constant [s]
    end
```

```
    M_l(:,j) = Mf(j) - M(:,j); %Liquid film mass remaining on tip [kg]
    L_l(:,j) = L0(j) - L(:,j); %Liquid film thickness remaining on tip [m]
end


% Injector tip conditions at time of spark assuming no condensation and
tumble gas flow is to remove any evaporated vapor
M_tip = zeros(n0,1);
L_tip = zeros(n0,1);
Tl_tip = zeros(n0,1);
tau_tip = zeros(n0,1);
DT = zeros(n0,1);

for i = 1:n0
    ind1 = find(CAD==EOI(i));
    ind2 = find(CAD==SPA(i));
    DT(i) = (SPA(i)-EOI(i))/6/RPM(i)*1000; %Drying time [ms]
    M_tip(i) = min(M_l(ind1:ind2,i))*1000000; %Fuel film thickness @ SPA [mg]
    L_tip(i) = min(L_l(ind1:ind2,i))*1000; %Fuel film thickness [mm]
    Tl_tip(i) = min(Tl(ind1:ind2,i))-273.15; %Fuel film temperature [deg C]
    tau_tip(i) = mean(tau_c(ind1:ind2,i))*1000; %Evaporation time constant
[ms]
end
```

Appendix C Repeatability Analysis

To ensure the consistency and integrity of the experimental setup and measurement systems, the warmup and coking tests was repeated three times for 10 bar BMEP and 2000 RPM.

C.1 Repeatability of Warmup Test

Figure C.1 shows the measured PN for the three warmup trials at time 0 hrs (clean injector tip). Good repeatability is observed, where the peak PN was similar as well as once the engine-out coolant temperature exceeded 60 °C, all trials converged to the same PN level. The stabilized PN in the last 60 seconds was found to be repeatable within 20% error, calculated from one standard deviation.

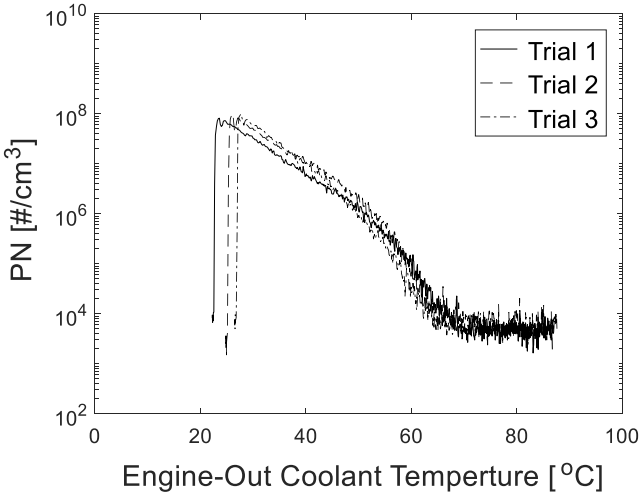

Figure C.1: Repeatability of PN measurement for the warmup procedure at time 0 hrs. Results for 4 bar BMEP and 1000 RPM

Figure C.2 shows the three trials for the measured tip and fuel temperatures at time 0 hrs. The measurement of tip and fuel temperatures was found to be repeatable within 5% error, calculated from one standard deviation.

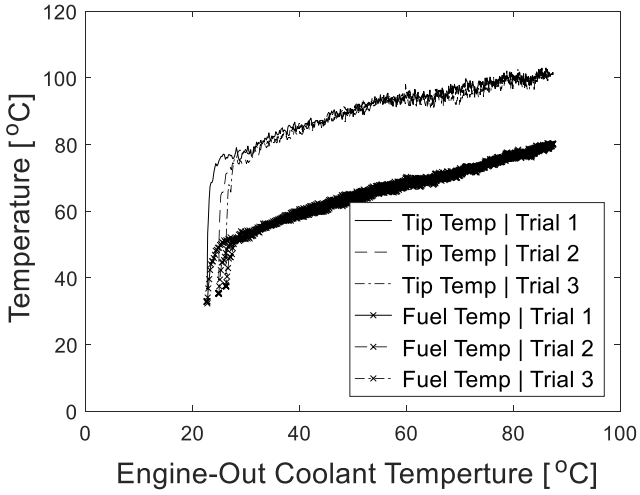

Figure C.2: Repeatability of tip and fuel temperatures measurement for the warmup procedure at time 0 hrs. Results for 4 bar BMEP and 1000 RPM

C.2 Repeatability of Coking Test

Figure C.3 shows the measured PN for the three trials of the coking test. The tests were also found to be repeatable within 20% error. This error is expected when using the SPCS for particle counting.

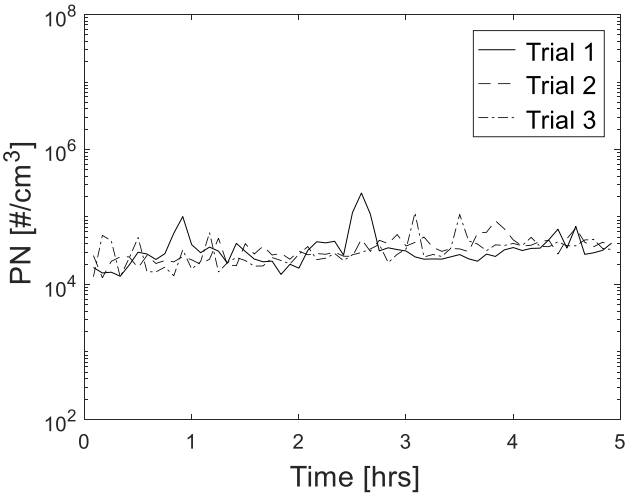

Figure C.3: Repeatability of PN measurement for the coking procedure. Results for 10 bar BMEP and 2000 RPM

Figure C.4 shows the repeated measurements for the tip and fuel temperatures for the coking test. These measurements also show good repeatability, within the same percentage error of 5%.

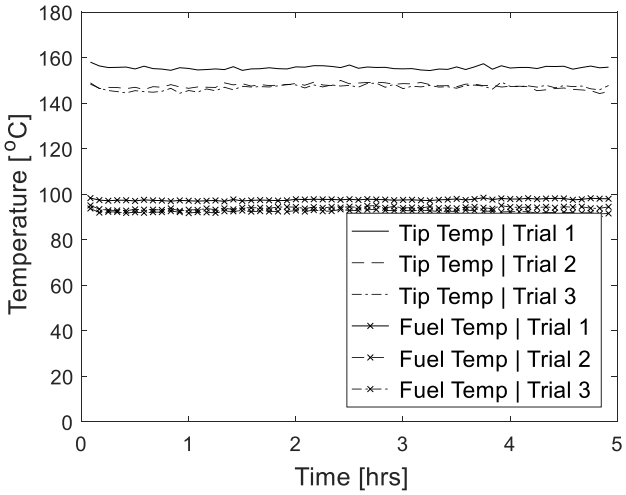

Figure C.4: Repeatability of tip and fuel temperatures measurement for the coking procedure. Results for 10 bar BMEP and 2000 RPM

Appendix D Evaporation Curves

Shown here are the complete evaporation curves, i.e. the predicted film mass and evaporation time constant, as a function of time during an engine cycle for all operating conditions tested.

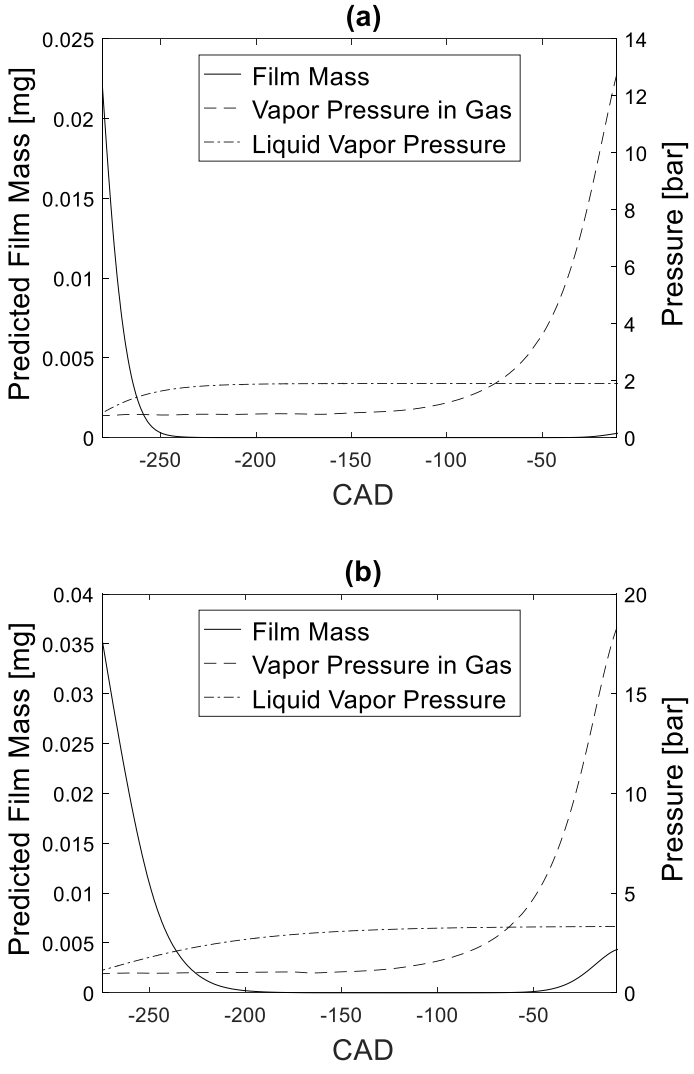

Figure D.1: Change of film mass during an engine cycle for 1000 RPM and (a) 6 bar and (b) 10 bar BMEP

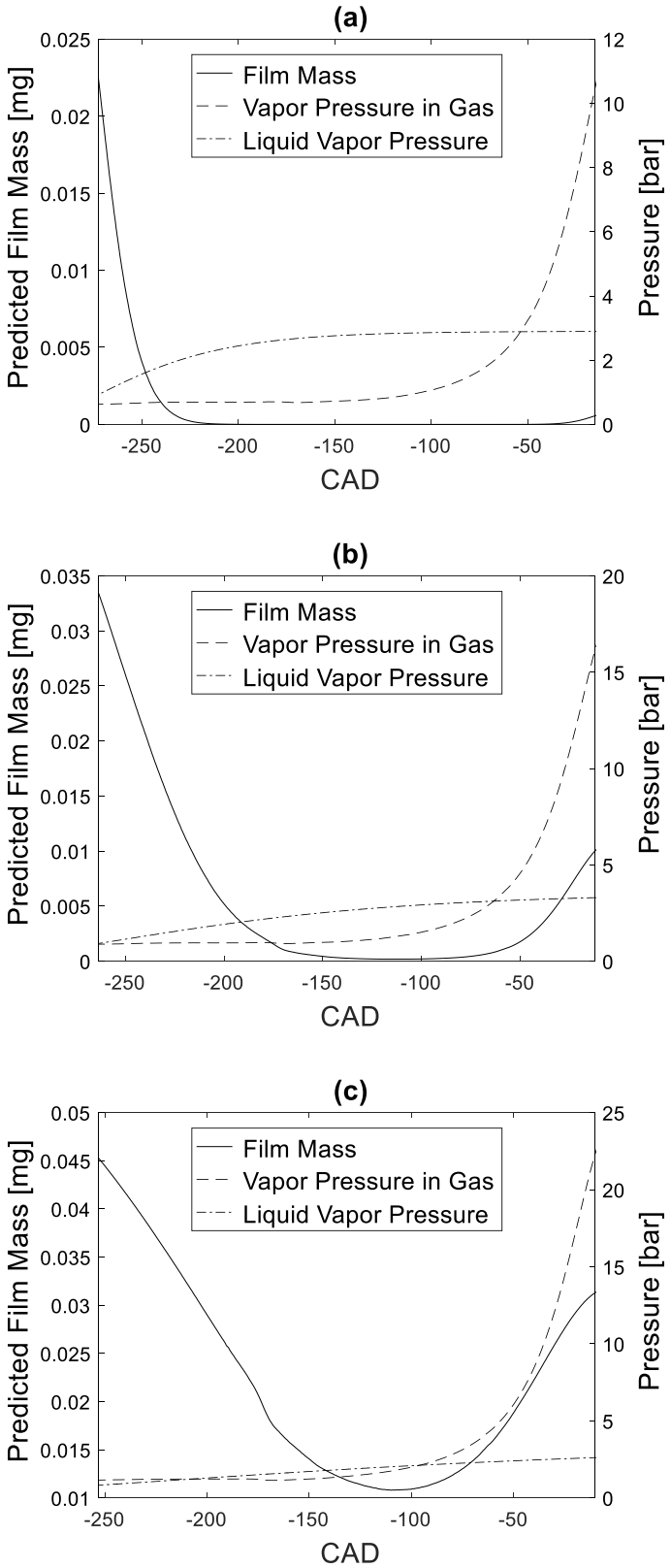

Figure D.2: Change of film mass during an engine cycle for 2000 RPM and (a) 6 bar, (b) 10 bar and (c) 14 bar BMEP

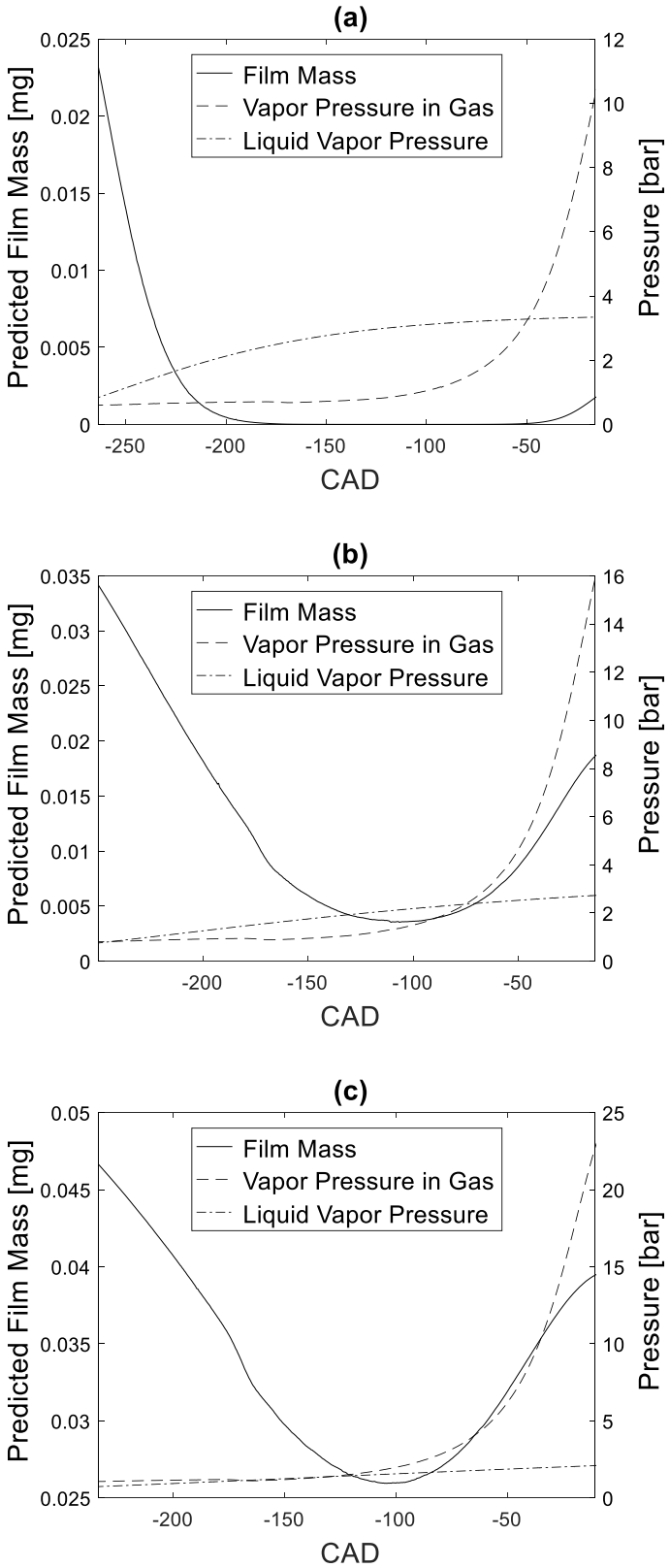

Figure D.3: Change of film mass during an engine cycle for 3000 RPM and (a) 6 bar, (b) 10 bar and (c) 14 bar BMEP

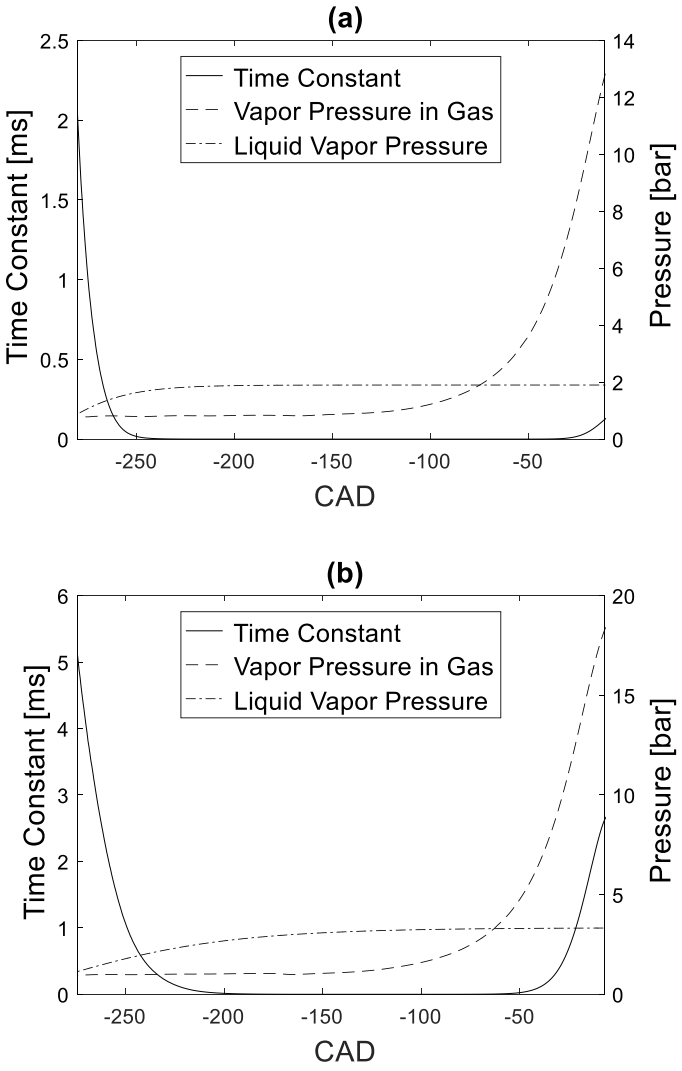

Figure D.4: Calculated time constant during an engine cycle for 1000 RPM and (a) 6 bar and (b) 10 bar BMEP

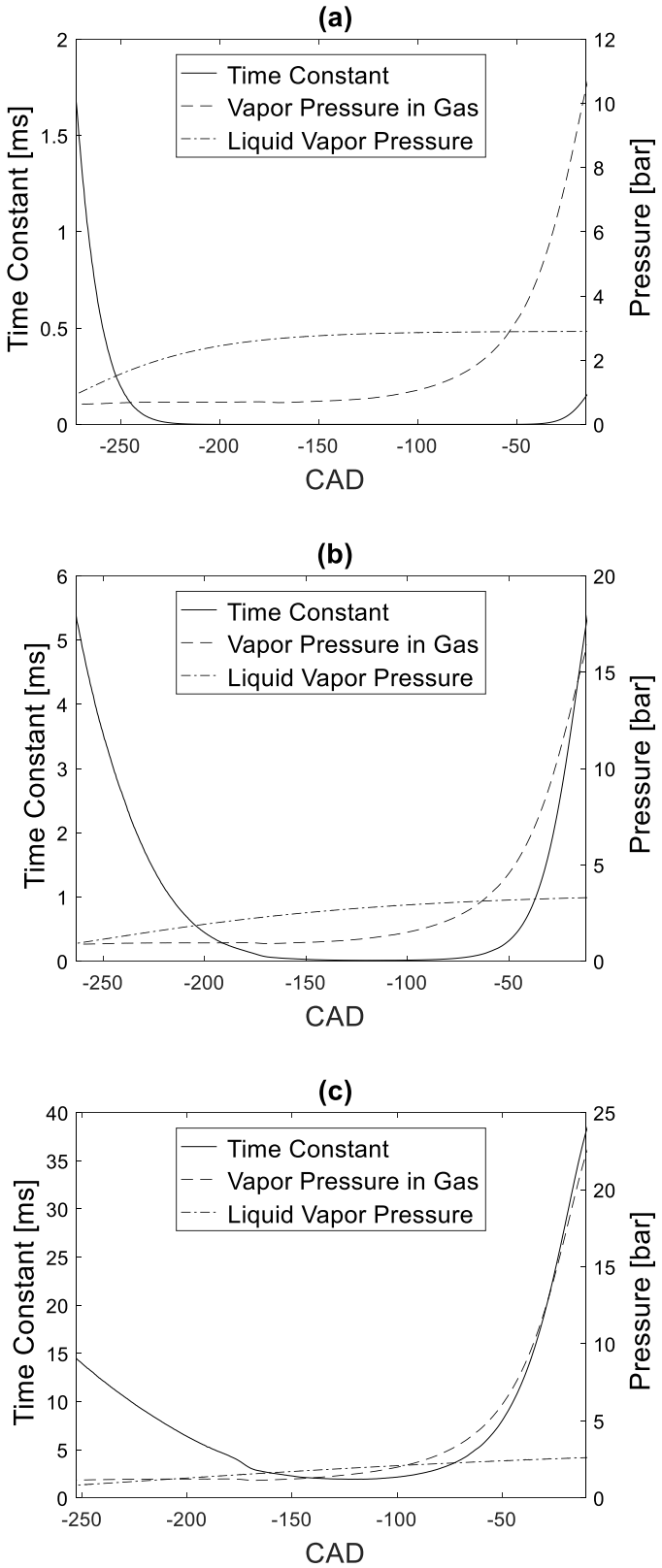

Figure D.5: Calculated time constant during an engine cycle for 2000 RPM and (a) 6 bar, (b) 10 bar and (c) 14 bar BMEP

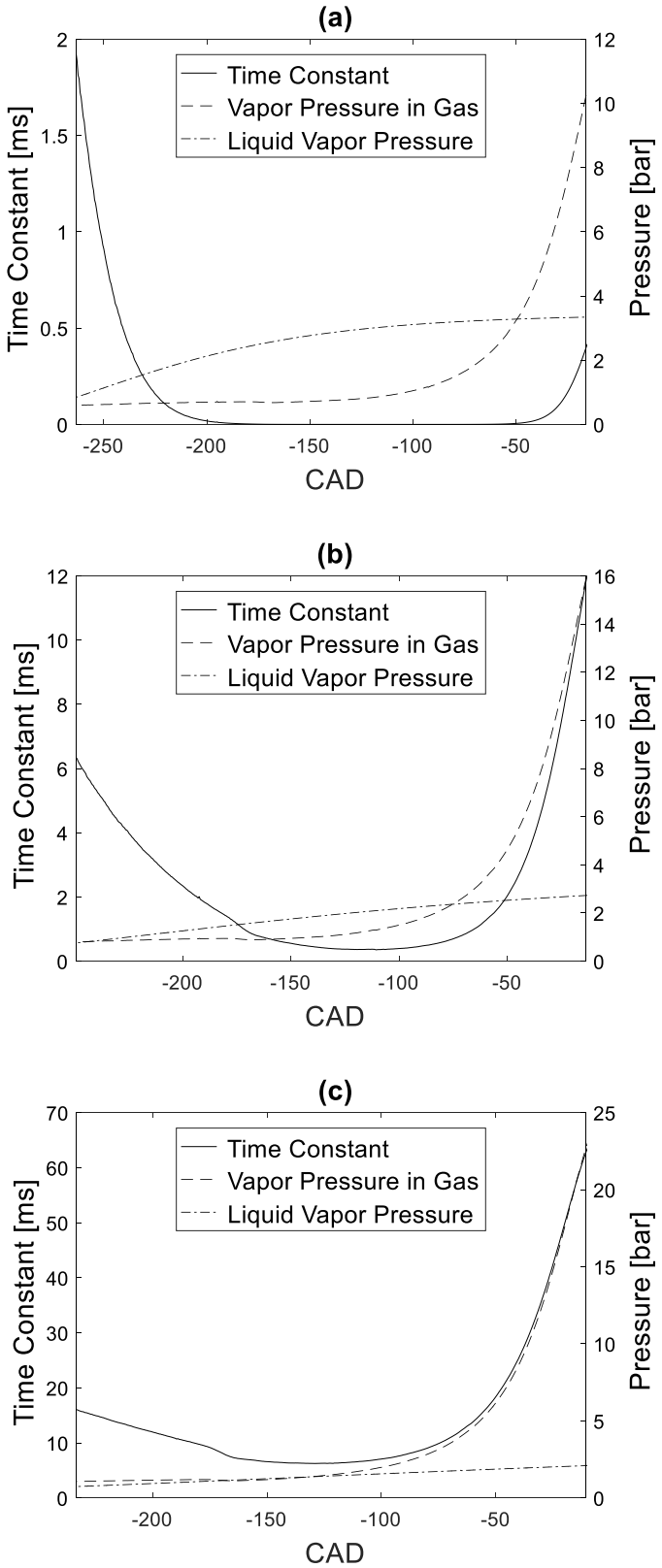

Figure D.6: Calculated time constant during an engine cycle for 3000 RPM and (a) 6 bar, (b) 10 bar and (c) 14 bar BMEP

Appendix E Sensitivity of Gas Temperature

Using the average gas temperature for all conditions in the analysis of each single operating point led to the same results as using the corresponding gas temperature profile for each condition. An example of this is shown in Figure E.1 for 10 bar BMEP and 2000 RPM. The figure shows the predicted film mass from the model calculated using the corresponding gas temperature for the operating point, as well as using the average gas temperature for all operating points. As seen in the figure, the predicted film mass was insensitive to the gas temperature, and the two evaporation curves overlapped. Thus, the average gas temperature for all conditions was used to perform a wider parametric study to investigate the effect of initial and boundary conditions on the predicted film mass and time constant.

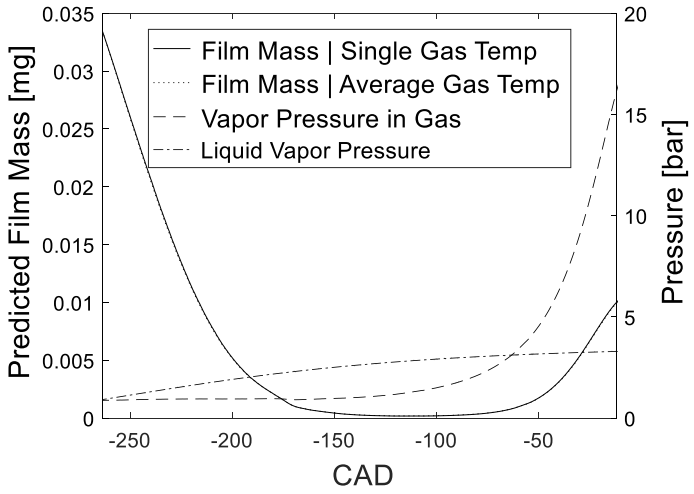

Figure E.1: Comparison of predicted film mass using the gas temperature profile for a single operating point (10 bar BMEP and 2000 RPM) versus the average gas temperature profile for all operating ponits

Bibliography

1. Li, X. and Wallace, J.S., “In-Cylinder Measurement of Temperature and Soot Concentration Using the Two-Color Method,” *SAE Technical Paper Series*, 1995, doi:10.4271/950848.

2. Dec, J.E., “A Conceptual Model of DI Diesel Combustion Based on Laser-Sheet Imaging,” *SAE Technical Paper Series*, 1997, doi:10.4271/970873.

3. Zhao, H. and Ladommatos, N., “Optical diagnostics for soot and tempeature in diesel engines,” *Prog. Energy Combust. Sci.* 24(97):221–255, 1998.

4. Flynn, P.F., Durrett, R.P., Hunter, G.L., Loye, A.O. zur, Akinyemi, O.C., Dec, J.E., and Westbrook, C.K., “Diesel Combustion: An Integrated View Combining Laser Diagnostics, Chemical Kinetics, And Empirical Validation,” 1999, doi:10.4271/1999-01-0509.

5. Akihama, K., Takatori, Y., Inagaki, K., Sasaki, S., and Dean, A.M., “Mechanism of the Smokeless Rich Diesel Combustion by Reducing Temperature,” *SAE Technical Paper Series*, 2001, doi:10.4271/2001-01-0655.

6. Spicher, U., Reissing, J., Kech, J.M., and Gindele, J., “Gasoline Direct Injection (GDI) Engines - Development Potentialities,” *SAE Technical Paper Series*, 1999, doi:10.4271/1999-01-2938.

7. Commission Regulation (EU) 2017/1151 of 1 June 2017 supplementing Regulation (EC) No 715/2007 of the European Parliament and of the Council on type-approval of motor vehicles with respect to emissions from light passenger and commercial vehicles (Euro 5 a, *Off. J. Eur. Union* (692):1–643, 2017.

8. He, H. and Yang, L., “China’s Stage 6 Emission Standard for New Light-Duty Vehicles,” *Int. Counc. Clean Transp.* (March):13, 2017.

9. Koczak, J., Boehman, A., and Brusstar, M., “Particulate Emissions in GDI Vehicle Transients: An Examination of FTP, HWFET, and US06 Measurements,” *SAE Tech. Pap. Ser.* 1, 2016, doi:10.4271/2016-01-0992.

10. Braisher, M., Stone, R., and Price, P., “Particle number emissions from a range of European vehicles,” *SAE Tech. Pap.*, 2010, doi:10.4271/2010-01-0786.

11. Leick, P., Bork, B., and Geiler, J.N., “Experimental characterization of tip wetting in gasoline DI injectors,” *ICLASS Conf.* (July):1–9, 2018.

12. Wu, C.-W., Chen, R.-H., Pu, J.-Y., and Lin, T.-H., “The influence of air–fuel ratio on engine performance and pollutant emission of an SI engine using ethanol–gasoline-blended fuels,” *Atmos. Environ.* 38(40):7093–7100, 2004, doi:10.1016/j.atmosenv.2004.01.058.

13. Lighty, J.A.S., Veranth, J.M., and Sarofim, A.F., “Combustion aerosols: Factors governing their size and composition and implications to human health,” *J. Air Waste Manag. Assoc.* 50(9):1565–1618, 2000, doi:10.1080/10473289.2000.10464197.

14. Bockhorn, H., “Soot Formation in Combustion: Mechanisms and Models,” Springer Berlin Heidelberg, Berlin, Heidelberg, ISBN 978-3-642-85169-8, 1994, doi:10.1007/978-3-642-85167-4.

15. Heywood, J.B., “Internal Combustion Engine Fundamentals,” McGraw-Hill Inc., ISBN 007028637X, 1988, doi:10.1016/s1350-4789(10)70041-6.

16. Frommherz, M., “Impact of Fuel Properties on Particulate Number Emis- sions from a Gasoline Direct Injection Engine,” Karlsruher Institut für Technologie, 2016.

17. Omidvarborna, H., Kumar, A., and Kim, D.S., “Recent studies on soot modeling for diesel combustion,” *Renew. Sustain. Energy Rev.* 48:635–647, 2015, doi:10.1016/j.rser.2015.04.019.

18. Karjalainen, P., Pirjola, L., Heikkilä, J., Lähde, T., Tzamkiozis, T., Ntziachristos, L., Keskinen, J., and Rönkkö, T., “Exhaust particles of modern gasoline vehicles: A laboratory and an on-road study,” *Atmos. Environ.* 97:262–270, 2014, doi:10.1016/j.atmosenv.2014.08.025.

19. Oberdörster, G., Oberdörster, E., and Oberdörster, J., “Nanotoxicology: An emerging discipline evolving from studies of ultrafine particles,” *Environ. Health Perspect.* 113(7):823–839, 2005, doi:10.1289/ehp.7339.

20. Altin, O. and Eser, S., “Carbon Deposit Formation From Thermal Stressing of Petroleum Fuels,” *Prepr. Pap.-Am. Chem. Soc., Div. Fuel Chem* 49(2):764–766, 2004.

21. Xu, H., Wang, C., Ma, X., Sarangi, A.K., Weall, A., and Krueger-Venus, J., “Fuel injector deposits in direct-injection spark-ignition engines,” *Prog. Energy Combust. Sci.* 50:63–80, 2015, doi:10.1016/j.pecs.2015.02.002.

22. Boger, T. and Cutler, W., “Reducing Particulate Emissions in Gasoline Engines,” ISBN 9780768094176, 2018, doi:10.4271/0768094186.

23. Adamczyk, A.A., Kaiser, E.W., Cavolowsky, J.A., and Lavoie, G.A., “An Experimental Study of Hydrocarbon Emissions from Closed Vessel Explosions,” *18th Int. Symp. Combust. Combust. Inst.*, 1981.

24. Stevens, E. and Steeper, R., “Piston Wetting in an Optical DISI Engine : Fuel Films , Pool Fires , and Soot Generation,” *SAE Tech. Pap.* (2001-01–1203), 2001, doi:10.4271/2001-

01-1203.

25. Chen, L., Braisher, M., Crossley, A., Stone, R., and Richardson, D., “The Influence of Ethanol Blends on Particulate Matter Emissions from Gasoline Direct Injection Engines,” *SAE Int.* (2010-01–0793), 2010.

26. Fatouraie, M., Wooldridge, M., and Wooldridge, S., “In-Cylinder Particulate Matter and Spray Imaging of Ethanol / Gasoline Blends in a Direct Injection Spark Ignition Engine,” *SAE Int. J. Fuels Lubr.* 6(1), 2013, doi:10.4271/2013-01-0259.

27. Singh, R., Burch, T., Lavoie, G., and Wooldridge, M., “Effects of Fuel Injection Events of Ethanol and Gasoline Blends on Boosted Direct-Injection Engine Performance,” *SAE Int. J. Fuels Lubr.*, 2017, doi:10.4271/2017-01-2238.Copyright.

28. Berndorfer, A., Breuer, S., Piock, W., and Bacho, P. Von, “Diffusion Combustion Phenomena in GDi Engines caused by Injection Process,” *SAE International*, 2013, doi:10.4271/2013-01-0261.

29. Steimle, F., Kulzer, A., Richter, H., Schwarzenthal, D., and Romberg, C., “Systematic analysis and particle emission reduction of homogeneous direct injection SI engines,” *SAE Tech. Pap.* 2, 2013, doi:10.4271/2013-01-0248.

30. Gawlica, T., Samenfink, W., Schünemann, E., and Koch, T., “Model-based optimization of multi-hole injector spray targeting for gasoline direct injection,” *Tagung Einspritzung und Kraftstoffe*, ISBN 1861346433: 271–289, 2019, doi:10.1007/978-3-658-23181-1_14.

31. Singh, R., Han, T., Fatouraie, M., Mansfield, A., Wooldridge, M., and Boehman, A., “Influence of fuel injection strategies on efficiency and particulate emissions of gasoline and ethanol blends in a turbocharged multi-cylinder direct injection engine,” *Int. J. Engine Res.* 1–13, 2019, doi:10.1177/1468087419838393.

32. Alzahrani, F., Medina, M., Fatouraie, M., Wooldridge, M., and Sick, V., “Mechanisms of Fuel Injector Tip Wetting and Tip Drying Based on Experimental Measurements of Engine-Out Particulate Emissions from Gasoline Direct Injection Engines,” *Process Int. J. Engine Res.*, 2019.

33. Wu, S., Yang, S., Wooldridge, M., and Xu, M., “Experimental study of the spray collapse process of multi-hole gasoline fuel injection at flash boiling conditions,” *Fuel* 242(January):109–123, 2019, doi:10.1016/j.fuel.2019.01.027.

34. Moulai, M., Grover, R., Parrish, S., and Schmidt, D., “Internal and Near-Nozzle Flow in a Multi-Hole Gasoline Injector Under Flashing and Non-Flashing Conditions,” *SAE Tech. Pap. Ser.* 1, 2015, doi:10.4271/2015-01-0944.

35. Han, J.-S., Lai, M.-C., Henein, N.A., Wang, T.C., Xie, X.B., Miles, P.C., Harrington, D.L., and Pinson, J., “Dynamics of Multiple-Injection Fuel Sprays in a Small-bore HSDI Diesel Engine,” *SAE Tech. Pap. Ser.* 1(724), 2000, doi:10.4271/2000-01-1256.

36. Swantek, A.B., Duke, D.J., Tilocco, F.Z., Sovis, N., and Powell, C.F., “End of Injection, Mass Expulsion Behaviors in Single Hole Diesel Fuel Injectors,” *ILASS Am. 26th Annu. Conf. Liq. At. Spray Syst.* (May), 2014.

37. Moon, S., Huang, W., Li, Z., and Wang, J., “End-of-injection fuel dribble of multi-hole diesel injector: Comprehensive investigation of phenomenon and discussion on control strategy,” *Appl. Energy* 179, 2016, doi:10.1016/j.apenergy.2016.06.116.

38. Eagle, E.W. and Musculus, M.P.B., “Cinema - Stereo Imaging of Fuel Dribble after the End of Injection in an Optical Heavy - Duty Diesel Engine,” *Thiesel*, 1–20, 2014.

39. Peterson, K., Grover, R., and Mitcham, C., “Application of optical diagnostics and simulation to fuel injector tip wetting and soot production,” *11th International Symposium on Combustion Diagnostics*, 2014.

40. Stanglmaier, R.H., Roberts, C.E., and Moses, C.A., “Vaporization of Individual Fuel Drops on a Heated Surface: A Study of Fuel-Wall Interactions within Direct-Injected Gasoline (DIG) Engines,” *SAE Tech. Pap. Ser.* 1(724), 2010, doi:10.4271/2002-01-0838.

41. Karwa, N., Stephan, P., Wiese, W., and Lejsek, D., “Gasoline Direct Injection Engine Injector Tip Drying,” *19th Australasian Fluid Mechanics Conference*, ISBN 9780646596952: 5–8, 2014.

42. Kinoshita, M., Saito, A., Matsushita, S., Shibata, H., and Niwa, Y., “A Method for Suppressing Formation of Deposits on Fuel Injector for Direct Injection Gasoline Engine,” *SAE Technical Paper Series*, 1999, doi:10.4271/1999-01-3656.

43. Aradi, A.A., Imoehl, B., Avery, N.L., Wells, P.P., and Grosser, R.W., “The Effect of Fuel Composition and Engine Operating Parameters on Injector Deposits in a High-Pressure Direct Injection Gasoline (DIG) Research Engine,” *SAE Technical Paper Series*, 1999, doi:10.4271/1999-01-3690.

44. Slavchov, R.I., Mosbach, S., Kraft, M., Pearson, R., and Filip, S. V., “An adsorption-precipitation model for the formation of injector external deposits in internal combustion engines,” *Appl. Energy* 228(187):1423–1438, 2018, doi:10.1016/j.apenergy.2018.06.130.

45. Dageförde, H., Kiefer, A., Samenfink, W., Wiese, W., and Kufferath, A., “Requirements for Spray and Tip Design of a Multi-hole Injector for DISI Engines,” *ICLASS Conf.* 1–8, 2015.

46. Leick, P., Schmitt, M., Kubis, T., Stapf, K.G., and Gawlica, T., “Impact of flash-boiling on gasoline sprays : From fundamental physical insights to engine-measured PN emissions,” *13th AVL Symposium*, 2018.

47. Peterson, K., Grover, R., and Mitcham, C., “Application of optical diagnostics and simulation to fuel injector tip wetting and soot production.”

48. Knorsch, T., Rogler, P., Miller, M., and Wiese, W., “On the Evaluation Methods for

Systematic Further Development of Direct-Injection Nozzles," *SAE Tech. Pap.* 01, 2016.

49. Henkel, S., Hardalupas, Y., Taylor, A., Conifer, C., Cracknell, R., Goh, T.K., Reinicke, P.-B., Sens, M., and Rieß, M., "Injector Fouling and Its Impact on Engine Emissions and Spray Characteristics in Gasoline Direct Injection Engines," *SAE Int. J. Fuels Lubr.* 10(2):287–295, 2017, doi:10.4271/2017-01-0808.

50. Piock, W.F., Befrui, B., Berndorfer, A., and Hoffmann, G., "Fuel Pressure and Charge Motion Effects on GDi Engine Particulate Emissions," *SAE Int. J. Engines* 8(2):464–473, 2015, doi:10.4271/2015-01-0746.

51. Fischer, A. and Thelliez, M., "Methodology and Tools to Predict GDI Injector Tip Wetting as Predecessor of Tip Sooting," *SAE Tech. Pap.* (2018-01–0286):1–10, 2018, doi:10.4271/2018-01-0286.

52. Aradi, A.A., Colucci, W.J., Scull, H.M., and Openshaw, M.J., "A Study of Fuel Additives for Direct Injection Gasoline (DIG) Injector Deposit Control," *SAE Technical Paper Series*, 2000, doi:10.4271/2000-01-2020.

53. Miura, Y., Miyahara, K., Sasaki, S., Kashio, T., and Yoshida, K., "Development of a Gasoline Direct Injector Fouling Test and Its Application to Study of Keep-Clean Performance at Different Additive Treat Rates," *SAE Technical Paper Series*, 2016, doi:10.4271/2016-01-2248.

54. Aradi, A.A., Evans, J., Miller, K., and Hotchkiss, A., "Direct Injection Gasoline (DIG) Injector Deposit Control with Additives," *SAE Technical Paper Series*, 2003, doi:10.4271/2003-01-2024.

55. China, P. and Rivere, J.-P., "Development of a Direct Injection Spark Ignition Engine Test for Injector Fouling," 2003, doi:10.4271/2003-01-2006.

56. DuMont, R.J., Evans, J.A., Feist, D.P., Studzinski, W.M., and Cushing, T.J., "Test and Control of Fuel Injector Deposits in Direct Injected Spark Ignition Vehicles," *SAE Technical Paper Series*, 2009, doi:10.4271/2009-01-2641.

57. Erbil, H.Y., "Evaporation of pure liquid sessile and spherical suspended drops: A review," *Adv. Colloid Interface Sci.* 170(1–2):67–86, 2012, doi:10.1016/j.cis.2011.12.006.

58. Maxwell, J.C., "The scientific papers of James Clerk Maxwell," *Cambridge* 2:625, 1890, doi:10.1017/CBO9780511710377.

59. Fuchs, N.A., "Evaporation and Droplet Growth in Gaseous Media," Elsevier, 1959.

60. Poling, B.E., Prausnitz, J.M., and O'Connell, J.P., "DIFFUSION COEFFICIENTS, Chapter," *Properties of Gases and Liquids*, Fifth Ed, McGraw-Hill Inc., New York, 2001.

61. Fatouraie, M., Frommherz, M., Mosburger, M., Chapman, E., Li, S., McCormick, R., and Fioroni, G., "Investigation of the Impact of Fuel Properties on Particulate Number

Emission of a Modern Gasoline Direct Injection Engine," *SAE Tech. Pap.* 2018-April:1–14, 2018, doi:10.4271/2018-01-0358.

62. Chickos, J.S. and Acree, W.E., "Enthalpies of vaporization of organic and organometallic compounds, 1880-2002," *J. Phys. Chem. Ref. Data* 32(2):519–878, 2003, doi:10.1063/1.1529214.

63. Stiel, L.I. and Thodos, G., "Lennard-Jones Force Constants Predicted from Critical Properties," *J. Chem. Eng. Data* 7(2):234–236, 1962, doi:10.1021/je60013a023.

64. Kulzer, A.C., "BDE-Direktstart: Startoptimierung eines Ottomotors mit Direkteinspritzung mittels eines thermodynamischen Motorsimulationsmodells," 2003.

65. Kulzer, A. and Lejsek, D., BeCAT User Manual, 2010.

66. Horiba Ltd., "Solid Particle Counting System MEXA-2100SPCS Instruction manual," 2002.

67. Fatouraie, M., Peterson, K., Biddappa, B., Livshiz, N., Larimore, J., and Mosburger, M., "Advanced Gasoline Combustion and Engine Controls," *Reducing Particulate Emissions in Gasoline Engines*, SAE International, Warrendale: 103–114, 2018.

68. Singh, R., "Enabling Ethanol Use as a Renewable Transportation Fuel: A Micro- and Macro-scale Perspective," University of Michigan, 2019.

69. Boger, T. and Cutler, W., "Reducing Particulate Emissions in Gasoline Engines," SAE International, Warrendale, ISBN 9780768094176, 2018, doi:10.4271/0768094186.

70. Braisher, M., Stone, R., and Price, P., "Particle number emissions from a range of European vehicles," *SAE Tech. Pap.* (Ci), 2010, doi:10.4271/2010-01-0786.

71. Poling, B.E., Prausnitz, J.M., and O'Connell, J.P., "B. LENNARD-JONES POTENTIALS AS DETERMINED FROM VISCOSITY DATA," *Properties of Gases and Liquids*, 2011.

72. Wang, X., Wu, J., Qiu, S., and Li, X., "Measurements of the Thermal Conductivity of n - Octane, Isooctane, 1-Octene, and 1-Octanol in the Temperature Range from 253 to 393 K at Pressures up to 30 MPa," *J. Chem. Eng. Data* acs.jced.9b00628, 2019, doi:10.1021/acs.jced.9b00628.

73. Pitzer, K.S., "The Thermodynamics of n-Heptane and 2,2,4-Trimethylpentane, Including Heat Capacities, Heats of Fusion and Vaporization and Entropies," *J. Am. Chem. Soc.* 62(5):1224–1227, 1940, doi:10.1021/ja01862a068.